Determination of the Half Lives of Rare Decays of Cd, Te and Zn Isotopes for the COBRA Experiment

Dissertation
zur Erlangung des akademischen Grades
eines Doktors der Naturwissenschaften
des Fachbereichs Physik
der Universität Dortmund

vorgelegt von
DIPL. PHYS. HENNING KIEL

Lehrstuhl für Experimentelle Physik IV
Fachbereich Physik
Universität Dortmund

Dortmund, den 23. Mai 2005

Neutrinos by *John Updike* (1960)

Neutrinos: they are very small
They have no charge; they have no mass;
they do not interact at all.
The Earth is just a silly ball
to them, through which they simply pass
like dustmaids down a drafty hall
or photons through a sheet of glass.
They snub the most exquisite gas,
ignore the most substantial wall,
cold shoulder steel and sounding brass,
insult the stallion in his stall,
and, scorning barriers of class,
infiltrate you and me. Like tall
and painless guillotines they fall
down through our heads into the grass.
At night, they enter at Nepal
and pierce the lover and his lass
from underneath the bed. You call
it wonderful; I call it crass.

Determination of the Half Lives of Rare Decays of Cd, Te and Zn Isotopes for the COBRA Experiment

Dissertation
zur Erlangung des akademischen Grades
eines Doktors der Naturwissenschaften
des Fachbereichs Physik
der Universität Dortmund

vorgelegt von
DIPL. PHYS. HENNING KIEL

Dekan:	Prof. Dr. M. Tolan
Referent:	Priv. Doz. Dr. K. Zuber
Korreferent:	Prof. Dr. C. Gößling
Beisitzer:	Dr. D. Schirmer
Tag der mündlichen Prüfung:	27. Juni 2005

Teilergebnisse dieser Arbeit waren Gegenstand verschiedener Veröffentlichungen und Tagungsbeiträge. Eine Liste befindet sich am Ende der Arbeit ab Seite 149.

Contents

Introduction

As a natural science, the goal of physics is to provide a realistic model of the fundamental processes in the world. Concerning the description of the components of matter, the Standard Model of Particle Physics is a good description of elementary particles and their interactions. However, this model has its limitations as the zero neutrino masses have been introduced ad hoc.

Therefore, neutrino physics plays a crucial role in modern particle physics. In light of recent measurements of the SNO experiment which finally solved the solar neutrino puzzle other questions concerning neutrinos have become more important. The individual lepton flavour number is no longer a conserved property. In flavour changing processes, the parameters to be measured are the squared mass differences $\Delta \mathrm{m}^2$ of the neutrino mass eigenstates and mixing angles of the neutrino flavours and mass eigenstates. However, certain properties of the neutrino remain unknown, such as the absolute mass scale, their mass hierarchy or the nature of neutrinos – whether they are Dirac or Majorana particles.

The investigation of beta spectra, or to be more precise, the analysis of the endpoint of the beta spectrum of e.g. tritium can reveal the absolute mass of the electron neutrino, however, so far the only handle to find out about the neutrino being either Dirac or Majorana type is the analysis of double beta decays.

The most stringent limits of the Majorana neutrino mass come from the Heidelberg-Moscow experiment. A claim for evidence of neutrino-less double beta decay in ^{76}Ge has been published by a sub group of the Heidelberg-Moscow collaboration, however, its correctness is still controversial as the observed signal may well be just a so far unknown background.

In this work the COBRA experiment is presented. It is a new approach to double beta decay investigating cadmium, tellurium and zinc isotopes at the same time. The detector is based on a new generation of CdTe/CdZnTe crystals which can be used as semiconductor detectors with good energy resolution. One of the isotopes in CdZnTe has a higher transition energy than the highest energetic naturally occurring gamma line. Another advantage of looking at a a different energy is to avoid the same background as in germanium experiments and to cross check their result with different nuclei. This is of utmost importance as the nuclear matrix elements play a significant role in the calculation of the neutrino mass if a half life of neutrino-less double beta decay can be measured. These nuclear matrix elements are measured in nuclear physics, however, they can also be measured with neutrino accompanied double beta decay which is an allowed process in the Standard Model. Still, it is uncertain how to transfer the 2ν nuclear matrix elements to the 0ν process. The neutrino accompanied double beta process has been already observed for the first lepton generation, yet the neutrino-less mode remains unobserved.

This thesis is divided into the following sections.
In the first chapter an introduction to double beta decay is given. Here, the neutrino accompanied and neutrino-less modes are presented and their experimental signature is discussed.
The second chapter starts with a description of semiconductor detectors with CdZnTe as a special example. Then the need for a method to reduce background is motivated and the shielding system of the COBRA experiment is presented. Finally, the current detector setup is described in detail.
The development of an appropriate data acquisition system is presented in chapter three. This includes the description of a provisional system based on the CAMAC bus which was built as part of this thesis as well as the construction of the new system based on the VME bus including a custom built ADC. The development of a new data acquisition system is motivated because the CAMAC system is based on almost thirty years old electronics components.
A major part of any new experiment is to simulate the new detector setup with a sophisticated Monte Carlo simulation program. This simulation allows to estimate detection efficiencies for signal processes and to optimise the setup. The simulation can also help in understanding the background contribution of building components in measured spectra. The simulation program for the COBRA experiment which was developed within this thesis is described in chapter four.
Finally, the data taken with the introduced detector setup is presented in chapter five. With this data the analysis of rare decays is carried out leading to limits on the half lives of double beta decays as well as the beta decay of ^{113}Cd and charge non-conserving decays.
At last, the achieved experimental goals are summarised and conclusions are drawn. An outlook on future enhancements of the detector setup as well as additional physics processes to be measured with a larger detector is given.

Chapter 1

Double Beta Decay

In nuclear double beta decay the electric charge of a decaying nucleus changes by two units leaving its atomic number unchanged [Boe87, Zub04]. This process was originally proposed by Maria Goeppert-Mayer in 1935 [GM35]. With half lives around 10^{20} years double beta decay is amongst the rarest processes ever measured. This has to be compared to the current age of the universe $t_0 = (13.7 \pm 0.2) \cdot 10^9$ years [Eid04], which means that almost all nuclei which may disintegrate via double beta decay are still existent since their creation. A more common decay mode is single beta decay. Here, the half life is less than a few years for most of the isotopes [SE98]. Other searches for rare processes like the proton decay resulted in a lower limit of the half life of $2.1 \cdot 10^{29}$ years.
In the following sections, the connection of double beta decay to neutrino physics is presented, then the double beta process is discussed theoretically. The discussion starts with the neutrino accompanied double beta decay mode which is allowed in the Standard Model. After this, the neutrino-less mode is envisaged which is subject of many current experiments. Finally, more speculative modes are sketched.

1.1 Neutrino Physics

Since the postulation of the neutrino by Pauli in 1930 [Pau30] to solve the puzzle of the continuous electron spectrum in nuclear beta decay, the understanding of the neutrino and its properties has changed drastically. The neutrino had been introduced as a massless spin-$\frac{1}{2}$ particle into the Standard Model of particle physics coupling only to left handed weak currents, because it was observed with a fixed helicity

$$H = \frac{\vec{s} \cdot \vec{p}}{|\vec{p}|} \tag{1.1.1}$$

with the spin $\vec{s}$ of the neutrino and its momentum $\vec{p}$ anti-parallel to each other whereas for the anti-neutrino spin and momentum are parallel [Zub04].
The first detection of a free neutrino has been published in 1953 by Cowan and Reines [Rei53a]. The apparatus to detect the neutrino was using a large amount of organic liquid scintillator [Cow53, Rei53b]. The reaction involved in the detection of the neutrino is the inverse of the nuclear beta decay:

$$\bar{\nu} + \mathrm{p} \rightarrow \mathrm{n} + \mathrm{e}^+ \tag{1.1.2}$$

Here, the prompt signal from the positron was measured. As a neutrino source, a nearby nuclear reactor was used. In a second step of the experiment cadmium salt was added to the scintillator to see a delayed signal of the neutron capture on the cadmium [Rei59].
Another experiment by Davis aimed at detecting neutrinos from the sun which should emit neutrinos from the decay of ^{8}B [Dav68]. The detection process is, again, inverse beta decay this time, however, with the reaction $^{37}\mathrm{Cl}(\nu, e^-)^{37}\mathrm{Ar}$. As a target material 520 t of detergent have been used. The detection of the reaction was done by pumping helium into the liquid scintillator purging the dissolved argon. The produced ^{37}Ar is then detected with proportional counters by measuring its beta decay. With this technique an amount of $2-7$ ^{37}Ar atoms produced per day has been measured. This experiment has been located in an underground laboratory to shield the apparatus from cosmic muons which create protons. These protons may produce ^{37}Ar by (p,n) reactions.
The outcome of this experiment was that only approximately $1/3$ of the predicted number of neutrinos was seen. Other experiments followed confirming this measurement [Fuk98, Ham99, Bel03, Gav03]. Also the number of ν_μ from atmospheric muons coming from the decay of charged pions

$$\pi^+ \rightarrow \mu^+ + \nu_\mu \qquad \mu^+ \rightarrow e^+ + \nu_e + \bar{\nu}_\mu \tag{1.1.3}$$
$$\pi^- \rightarrow \mu^- + \bar{\nu}_\mu \qquad \mu^- \rightarrow e^- + \bar{\nu}_e + \nu_\mu \tag{1.1.4}$$

which are generated by cosmic ray interactions with the atmosphere showed a deviation from the predicted value. As the absolute flux depends strongly on the underlying model of hadron generation in the atmosphere and the incoming cosmic ray flux, the ratio of the numbers of electron- and muon-neutrinos [Zub04]

$$R = \frac{\nu_e + \bar{\nu}_e}{\nu_\mu + \bar{\nu}_\mu} \tag{1.1.5}$$

is calculated. This value can be calculated from theory with an uncertainty of only 5 %.
As a solution to the solar neutrino puzzle a process called neutrino oscillation was investigated. Here, the mass of the neutrinos is no longer assumed to be zero. However, the mass eigenstates are not identical to the known flavour eigenstates, but a linear combination of these. For a two neutrino model which only simplifies the calculations but does not change the underlying physics, two neutrino flavours are connected to the mass eigenstates via a unitary mixing matrix:

$$\begin{pmatrix} \nu_\alpha \\ \nu_\beta \end{pmatrix} = U \cdot \begin{pmatrix} \nu_1 \\ \nu_2 \end{pmatrix}, \quad \text{with U} = \begin{pmatrix} \cos\theta & \sin\theta \\ -\sin\theta & \cos\theta \end{pmatrix}. \tag{1.1.6}$$

If a neutrino is produced in a nuclear reaction as one flavour it is a linear combination of the mass eigenstates which propagate differently in space. As a result the composition of the neutrino in the flavour space may change and the measurement of the neutrino flavour at a different space point may result in another flavour than the one at the point of creation.
The probability of a $\nu_\alpha \Rightarrow \nu_\beta$ oscillation

$$P\left(\nu_\alpha \Rightarrow \nu_\beta\right) = \sin^2(2\theta)\sin^2\left(\frac{\pi L}{L_{\mathrm{osc}}}\right) \tag{1.1.7}$$

with the oscillation length

$$L_{\mathrm{osc}} = \frac{2.48(\mathrm{E}\,/\,\mathrm{GeV})}{(\Delta \mathrm{m}^2_{21}/\mathrm{eV}^2)}\ [\mathrm{m}] \tag{1.1.8}$$

depends on the energy E of the incident neutrino and the distance L between source and detector. Therefore, a wide parameter space in L and E had to be covered by experiments to extract the mixing angle θ and the mass difference $\Delta \mathrm{m}^2_{21} = \mathrm{m}^2_2 - \mathrm{m}^2_1$.

The success of the neutrino oscillation model was recently achieved by the Sudbury Neutrino Observatory (SNO) measuring solar neutrinos. In this experiment for the first time the total neutrino flux ϕ, i.e. including all flavours has been measured in addition to the electron neutrino $\phi(\nu_e)$ component of the neutrino flux. The observed reactions are from charged currents (CC), neutral currents (NC) and elastic scattering (ES):

$$\nu_e + \mathrm{d} \rightarrow e^- + \mathrm{p} + \mathrm{p} \qquad (\mathrm{CC}) \tag{1.1.9}$$

$$\nu + e^- \rightarrow \nu + e^- \qquad (\mathrm{ES}) \tag{1.1.10}$$

$$\nu + \mathrm{d} \rightarrow \nu + \mathrm{p} + \mathrm{n} \qquad (\mathrm{NC}). \tag{1.1.11}$$

CC processes have a threshold, because a massive lepton, the electron, muon or tauon has to be generated. Therefore, for solar neutrinos only ν_e can be detected via CC processes. ES is dominated by ν_e scattering as well

$$\frac{\mathrm{CC}}{\mathrm{ES}} = \frac{\phi\left(\nu_e\right)}{\phi\left(\nu_e\right) + 0.14\left(\phi\left(\nu_\mu\right) + \phi\left(\nu_\tau\right)\right)} \tag{1.1.12}$$

and has been measured before, but NC is independent of the neutrino flavour. The measurements resulted in a reduced number of ν_e measured with CC as expected from the previous experiments, but the total number of neutrinos of any flavour matches the number of neutrinos expected from the solar model [Ahm02]. This means that neither the neutrinos vanish nor that the calculations of the solar model is wrong.

From equation 1.1.7 it becomes obvious, that oscillation experiments can only measure the difference of the squared masses of the neutrino mass eigenstates $\Delta \mathrm{m}^2_{\mathrm{ab}}$ and the mixing angle θ. As a consequence, the absolute mass scale of the neutrino masses remains unknown.

Other experiments trying to measure the absolute neutrino mass have been done by e.g. investigating the endpoint of beta spectra, preferably of tritium [Lob85, Pic92, Wei99]. The measured neutrino mass limit is $m_\nu < 2.8\,\mathrm{eV}$ (95 % C.L.) [Wei03].

From the results of the oscillation experiments two possible neutrino mass hierarchies as shown in figure 1.1 can be deduced. Here, the mass of the lightest neutrino mass eigenstate remains unknown. However, from beta and double beta experiments an upper limit on the mass of the lightest neutrinos can be given.

If the neutrino mass as measured by double beta decay $|m_{ee}|$ is below 50 meV, the three mass eigenstates are no longer quasi degenerate, but the underlying hierarchy can be resolved.

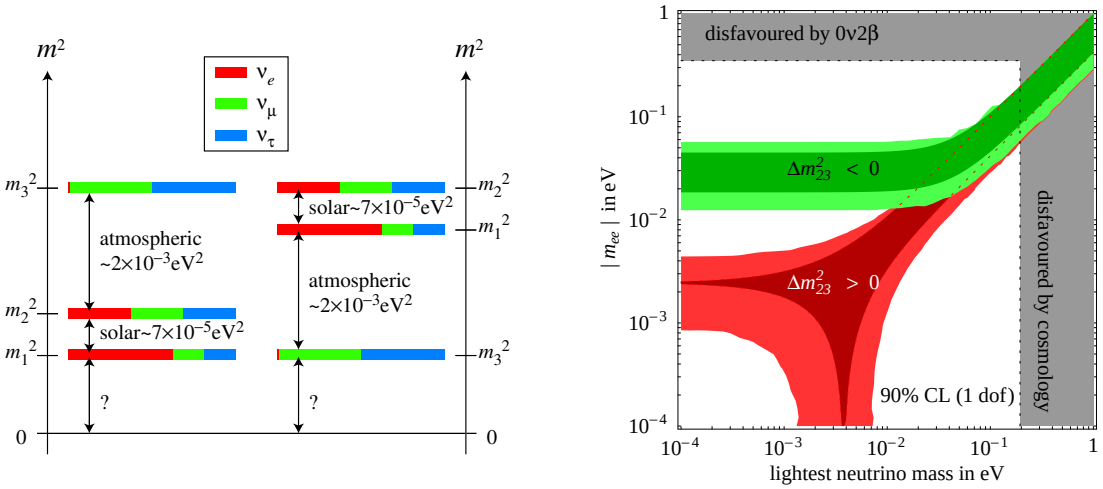

Figure 1.1: The two possible neutrino mass hierarchies resulting from the two measurements of $\Delta m^2_{\text{solar}} \simeq 7 \cdot 10^{-5}\,\text{eV}^2$ and $\Delta m^2_{\text{atmospheric}} \simeq 2 \cdot 10^{-3}\,\text{eV}^2$ from oscillation experiments are shown in the left picture. These experiments cannot distinguish between the two scenarios. The composition of the flavours is indicated by colours. The effective Majorana mass $\langle m_{ee} \rangle$ is plotted as a function of the mass of the lightest neutrino m_1 in the right picture [Fer02].

1.2 Neutrino Accompanied Double Beta Decay ($2\nu\beta\beta$)

Double beta decay can be seen as the decay of a nucleus via two simultaneous beta decays (two nucleon ($2n$) mechanism). Therefore, it is considered as the second order process with respect to the ordinary beta decay. Here, also β^- as well as β^+ and electron capture (EC) processes may occur leading to the following possible decay modes:

$$\begin{aligned}
(Z,A) &\rightarrow (Z+2,A) + 2\beta^- + 2\bar{\nu}_e && [2\nu\beta^-\beta^-]\\
(Z,A) &\rightarrow (Z-2,A) + 2\beta^+ + 2\nu_e && [2\nu\beta^+\beta^+]\\
e^- + (Z,A) &\rightarrow (Z-2,A) + \beta^+ + 2\nu_e && [2\nu\beta^+\text{EC}]\\
2e^- + (Z,A) &\rightarrow (Z-2,A) + 2\nu_e && [2\nu\text{EC EC}]
\end{aligned}$$

This second order process is allowed for any nucleus where the mass of the nucleus in the ground state is larger than the mass of the daughter nucleus $\text{m}(Z,A) > \text{m}(Z \pm 2, A)$. However, if $\text{m}(Z \pm 1, A) < \text{m}(Z,A)$ the process is obscured by single beta decay which is dominating the half life and therefore must be forbidden or at least strongly suppressed to detect double beta decay. A strong suppression of single beta decay may occur if mother and daughter nuclei have a large difference in angular momentum. This is the case for ^{48}Ca where ΔL is 5 or 6. Fortunately, there are 35 known nuclei in nature for which single beta decay is forbidden because of $\text{m}(Z \pm 1, A) > \text{m}(Z,A)$ whilst double beta decay is allowed. Figure 1.2 shows a schematic of the masses of the ground states of nuclei with a fixed number of nucleons (A) and variable number of protons (Z). It can be deduced from the semi-empirical Bethe-Weizsäcker equation for the binding energy per nucleon [Wei35, MK94]

$$E_B = a_v \cdot A - a_s \cdot A^{2/3} - a_c \cdot \frac{Z^2}{A^{1/3}} - a_a \cdot \frac{(Z - A/2)^2}{A} + \delta_p \qquad (1.2.13)$$

with the empiric coefficients $a_v = 15.85\,\mathrm{MeV}$ for the volume dependent part, $a_s = 18.34\,\mathrm{MeV}$ for the surface dependent part, $a_c = 0.71\,\mathrm{MeV}$ for the Coulomb part and $a_a = 92.86\,\mathrm{MeV}$ for the asymmetry part. For a constant number of nucleons A, the total mass of the nucleus (from now on using $\hbar = c = 1$)

$$\begin{aligned} \mathrm{m}_{\mathrm{nucleus}}(Z,A) &= Z \cdot \mathrm{m}_p + (A-Z)\cdot \mathrm{m}_n - E_B(Z,A) && (1.2.14)\\ &\propto \mathrm{const.} + a\cdot Z + b\cdot Z^2 + \delta_p && (1.2.15) \end{aligned}$$

only depends on Z giving a parabola.
For nuclei with an odd number of protons and an even number of neutrons ($N = A - Z$) and vice versa the δ_p term, which is the pairing energy, vanishes. For odd-odd nuclei the value yields $+11.46\,\mathrm{MeV}/A^{1/2}$, and for even-even nuclei it is $-11.46\,\mathrm{MeV}/A^{1/2}$ separating the two parabolae by $22.9\,\mathrm{MeV}/A^{1/2}$ [MK94]. In this scenario an even-even nucleus on the lower parabola might not be allowed to decay into its nearest neighbour which lies on the upper parabola because the neighbour's mass is larger. However, the second nearest neighbour which lies on the lower parabola has a smaller mass. Therefore, it can decay via double beta decay leaping the intermediate nucleus.

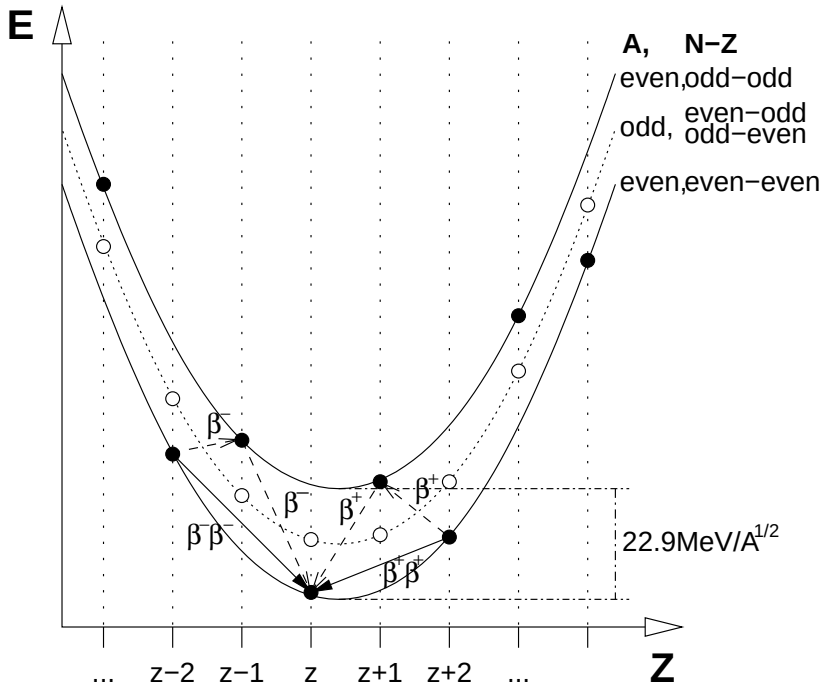

Figure 1.2: The double mass parabolae for nuclei with even number of nucleons A (solid lines) and the single mass parabola for odd number of nucleons (dotted line) are shown. For even number of nucleons the parabola splits up into two because of the pairing energy δ_p, which is $+11.46\,\mathrm{MeV}/A^{1/2}$ for odd number of neutrons N and protons Z, or $-11.46\,\mathrm{MeV}/A^{1/2}$ for even N and Z. Double beta decay is the dominant process for nuclei where $\mathrm{m}(Z,A) > \mathrm{m}(Z\pm 2,A)$ and $\mathrm{m}(Z,A) < \mathrm{m}(Z\pm 1,A)$. For all nuclei which do not fulfil the second condition single beta decay is the dominant decay channel, obscuring the very rare double beta decay.

The transition energy of this process, the Q-value, is the mass difference of the parent and daughter *atoms*. For $2\nu\beta^-\beta^-$ decays the whole released energy is carried away by the two beta electrons and neutrinos. In the β^+ modes the Q-value is reduced by $2\mathrm{m}_e$ per emitted positron, compared to double electron capture where also the full Q-value is released. This can be understood by simple book keeping as shown in the following paragraph.

As the masses of the atoms are measured values of the neutral atoms shell electrons have to be considered for the four cases (neglecting the neutrino masses):

$$\begin{aligned}
\text{(Z,A)} &\rightarrow \text{(Z+2,A)} + 2\,\beta^- + 2\,\bar{\nu_e} && [2\nu\beta^-\beta^-]\\
\mathrm{m}_{\mathrm{atom(Z,A)}} &= (\mathrm{m}_{\mathrm{atom(Z+2,A)}} - 2\cdot m_e) + 2\cdot m_e + E &&\\
\\
\text{(Z,A)} &\rightarrow \text{(Z-2,A)} + 2\,\beta^+ + 2\,\nu_e && [2\nu\beta^+\beta^+]\\
\mathrm{m}_{\mathrm{atom(Z,A)}} &= (\mathrm{m}_{\mathrm{atom(Z-2,A)}} + 2\cdot m_e) + 2\cdot m_e + E &&\\
\\
e^- + \text{(Z,A)} &\rightarrow \text{(Z-2,A)} + \beta^+ + 2\,\nu_e && [2\nu\beta^+\mathrm{EC}]\\
\mathrm{m}_{\mathrm{atom(Z,A)}} &= (\mathrm{m}_{\mathrm{atom(Z-2,A)}} + 1\cdot m_e) + m_e + E &&\\
\\
2e^- + \text{(Z,A)} &\rightarrow \text{(Z-2,A)} + 2\,\nu_e && [2\nu\mathrm{EC\,EC}]\\
\mathrm{m}_{\mathrm{atom(Z,A)}} &= (\mathrm{m}_{\mathrm{atom(Z-2,A)}}) + E &&
\end{aligned}$$

With the definition of the Q-value

$$Q = \mathrm{m}_{\mathrm{atom(Z,A)}} - \mathrm{m}_{\mathrm{atom(Z-2,A)}} \tag{1.2.16}$$

the resulting transition energy for a double beta decay with a number of β^+ particles n_{β^+} is

$$E = Q - 2n_{\beta^+}\cdot m_e \tag{1.2.17}$$

Like for beta decay the spectrum of $2\nu\beta\beta$ decay is continuous as well because the neutrinos carry energy away. The distribution of the sum of electron energies S is given by [Tre95] as

$$S(T) = \left(T^4 + 10\cdot T^3 + 40\cdot T^2 + 60\cdot T + 30\right)\cdot T\cdot (Q/\mathrm{m}_e - T)^5 \tag{1.2.18}$$

Here, the kinetic energy of both electrons T is given in multiples of their rest mass $T = E/\mathrm{m}_e$. Another parameter of this function is the Q-value of the transition, which is e.g. $Q = 2805\,\mathrm{keV}$ for ^{116}Cd.

For some isotopes the Q-value is large enough to allow transitions to excited states of the daughter nucleus. The nucleus then de-excites to its ground state emitting one or several gammas. In figure 1.3 the double beta transition of cadmium and tellurium isotopes to excited levels of the daughter nuclides palladium, tin and xenon are shown.

$2\nu\beta\beta$ decay is of special interest for nuclear physicists as it is possible to test nuclear matrix element calculations with it.

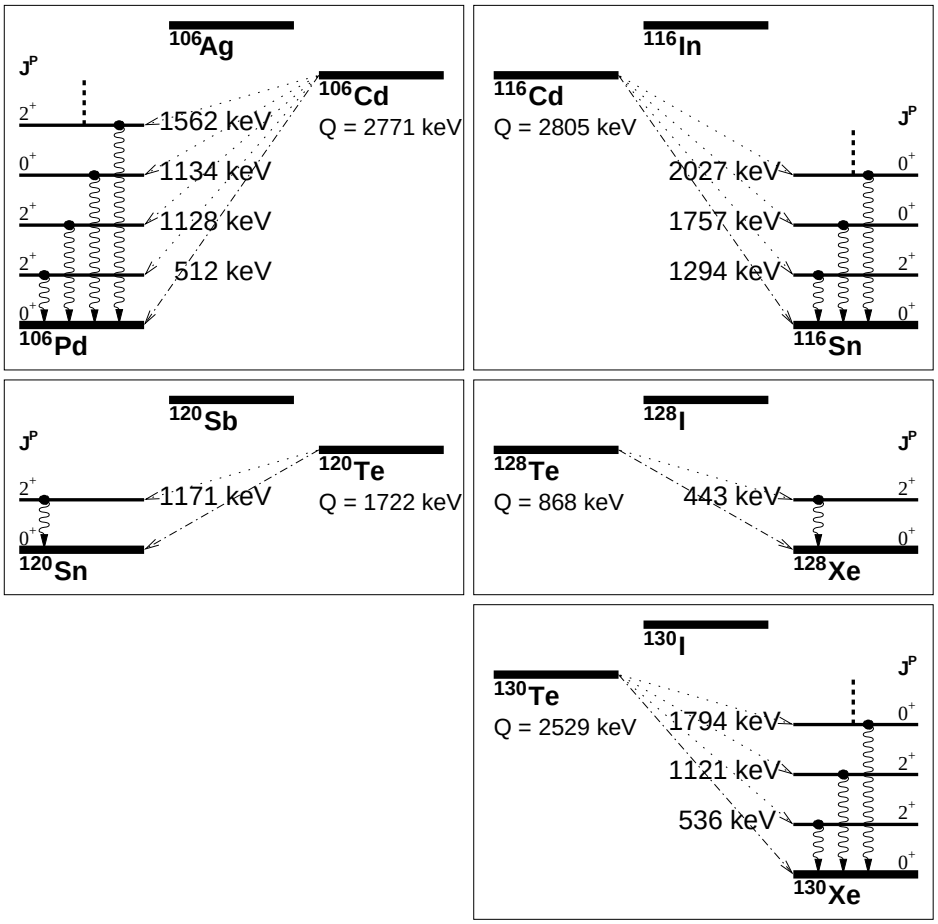

Figure 1.3: Double beta decays of cadmium and tellurium isotopes to excited states of the daughter nucleus. For ^{108}Cd and ^{114}Cd only the transition to the ground state is allowed and are therefore omitted. Energy levels are taken from [Shi78]. The schematics show $\beta^+\beta^+$ decays on the left hand side and $\beta^-\beta^-$ on the right hand side. The number J^P represents the angular momentum and parity of the excited state. The scheme only contains small J, because these are preferred transitions. Dots indicate additional higher energy levels. The curly arrows indicate the de-excitation gammas from the excited states to the ground state with their respective energies.

1.3 Neutrino-less Double Beta Decay ($0\nu\beta\beta$)

The above neutrino accompanied double beta transitions are allowed processes in the Standard Model of Particle Physics and have already been measured [Tre02]. This process conserves quantum numbers like lepton number. However, also the corresponding neutrino-less modes can be imagined:

$$\begin{aligned}
(Z,A) &\rightarrow (Z+2,A) + 2\beta^- && [0\nu\beta^-\beta^-]\\
(Z,A) &\rightarrow (Z-2,A) + 2\beta^+ && [0\nu\beta^+\beta^+]\\
e^- + (Z,A) &\rightarrow (Z-2,A) + \beta^+ && [0\nu\beta^+\mathrm{EC}]\\
2e^- + (Z,A) &\rightarrow (Z-2,A) && [0\nu\mathrm{EC\,EC}]
\end{aligned}$$

As there are no neutrinos in the final state anymore which could carry away energy the experimental signature is a mono-energetic line of the sum of electron energies opposed to the continuous spectrum for the neutrino accompanied double beta decay. Figure 1.4 shows these two spectra for ^{116}Cd with a Q-value of 2.805 MeV indicated by 0ν and 2ν.

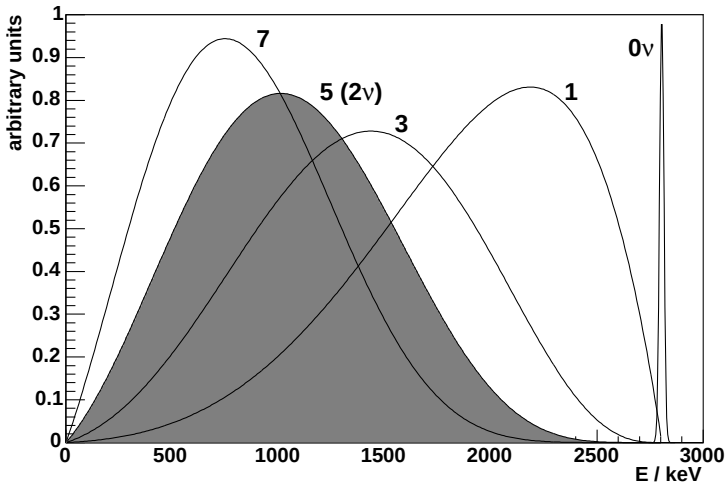

Figure 1.4: The sum energy spectrum of the two electrons emitted in $\beta\beta$ decay is shown for various modes. The endpoint is chosen as 2805 keV, which is the Q-value of ^{116}Cd. The peak at the endpoint is the shape of $0\nu\beta\beta$ decay. The continuous spectra represent the spectra with spectral indices of double beta decays with $n = 7$, $n = 5$, $n = 3$ and $n = 1$ from left to right. Normal $2\nu\beta\beta$ decay has a spectral index of 5 and is marked by a grey area under the spectrum.

The neutrino-less process does not only violate lepton family number conservation like neutrino oscillations do, but also the total lepton number. The favoured model to explain this decay mode is that the neutrino is a massive Majorana particle, i.e. it is its own anti-particle. In figure 1.5 the Feynman diagrams of the neutrino accompanied and neutrino-less double beta decay are shown. In order to make the neutrino-less process take place as well as the neutrino being its own anti-particle, a helicity flip must happen as illustrated by the cross.

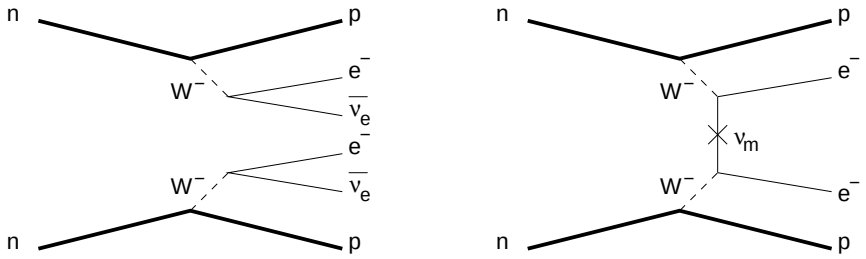

Figure 1.5: Feynman diagrams of the neutrino accompanied double beta decay on the left side and neutrino-less double beta decay on the right side. The cross marks the helicity flip of the massive Majorana neutrino ν_{m}.

Instead of a helicity flip, also right handed currents may solve the problem of exchanging the Majorana neutrino as shown in figure 1.6.

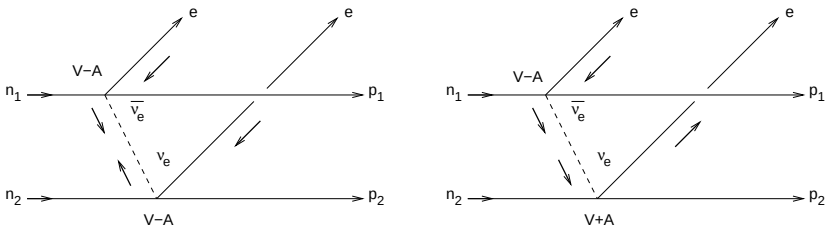

Figure 1.6: The schematic of the $0\nu\beta\beta$ decay is shown with either a helicity flip (left schematic) or a right handed current (V+A) at one vertex (right schematic). The arrows represent the helicity of the particles.

Double beta decay is often called the "gold plated channel" for testing the fundamental character of the neutrino, being either a Dirac or Majorana type particle. If the neutrino is a massive Majorana particle neutrino-less double beta decay must exist and the measured quantity is called effective Majorana neutrino mass $\langle m_{\nu_e} \rangle$. It is related to the observed half life $T_{1/2}$ via [Boe87]

$$(T_{1/2})^{-1} = G^{0\nu} \left| M_{GT}^{0\nu} - \frac{{g_V}^2}{{g_A}^2} M_F^{0\nu} \right|^2 \left(\frac{\langle m_{\nu_e} \rangle}{m_e} \right)^2 \tag{1.3.19}$$

where $G^{0\nu}$ is the phase space factor and $\left| M_{GT}^{0\nu} - \frac{{g_V}^2}{{g_A}^2} M_F^{0\nu} \right|^2$ corresponds to the involved nuclear matrix elements. The effective Majorana neutrino mass is given by

$$\langle m_{\nu_e} \rangle \; = \left| \sum_i U_{ei}^2 \eta_i m_i \right| \tag{1.3.20}$$

with the relative CP-phases $\eta_i = \pm 1$, the PMNS matrix elements U_{ei} and the corresponding mass eigenvalues m_i.
The Pontecorvo-Maki-Nakagawa-Sakata (PMNS) matrix [Mak62] which describes the mixing of the neutrino eigenstates is the analogue of the Cabibbo-Kobayashi-Maskawa (CKM) matrix for the quark mixing which has been known for decades. The three neutrino flavour eigenstates ν_e, ν_μ and ν_τ are connected to the mass eigenstates ν_1, ν_2 and ν_3 according to the following equation which is the general form of equation 1.1.6

$$\begin{pmatrix} \nu_e \\ \nu_\mu \\ \nu_\tau \end{pmatrix} = \begin{pmatrix} U_{e1} & U_{e2} & U_{e3} \\ U_{\mu 1} & U_{\mu 2} & U_{\mu 3} \\ U_{\tau 1} & U_{\tau 2} & U_{\tau 3} \end{pmatrix} \begin{pmatrix} \nu_1 \\ \nu_2 \\ \nu_3 \end{pmatrix}. \tag{1.3.21}$$

For different nuclei, a so-called figure of merit $\left(T_{1/2} \cdot \langle m_{\nu_e} \rangle^2 \right)$ can be drawn, showing the theoretically preferred isotopes as shown in table 1.1. The factor n describes the product of the phase space factor and the nuclear matrix element normalised to 1.0 for ^{76}Ge. Therefore, if one has to probe for a certain neutrino mass, the corresponding half life to detect is $1/n$ lower than for germanium, or with the same limit in half life, the square of the neutrino mass can be excluded by a factor $1/n$ better. Among the most promising isotopes are ^{130}Te and ^{116}Cd.
Apart from the above $2n$ mechanism further models to realise $0\nu\beta\beta$ decay are discussed such as right handed weak currents [Eji01]. In order to unravel the underlying mechanism $\beta^+\beta^+$ decay is a promising candidate. It has been shown to have an enhanced sensitivity to (V+A) interactions [Hir94].

Isotope	Q-value / keV	n
^{76}Ge	2039	1.00
^{82}Se	2995	3.86
^{100}Mo	3034	1.83
^{114}Cd	534	0.05
^{116}Cd	2805	4.78
^{128}Te	868	0.30
^{130}Te	2529	4.76
^{136}Xe	2480	1.05
^{150}Nd	3367	69.1

Table 1.1: Figure of merit showing some of the preferred isotopes. The nuclear matrix elements are taken from [Sta90].

The half life of the neutrino-less double beta decay can be derived from equation 1.3.19 [Eji01] as

$$\begin{aligned}(T_{1/2})^{-1} &= G^{0\nu}\left|M^{0\nu}\right|^2 \cdot \Big(\langle m_\nu\rangle^2 + C_{\lambda\lambda}\langle\lambda\rangle^2 + C_{\eta\eta}\langle\eta\rangle^2 \\ &\quad + C_{m\lambda}\langle m_\nu\rangle\langle\lambda\rangle + C_{\lambda\eta}\langle\lambda\rangle\langle\eta\rangle + C_{m\eta}\langle m_\nu\rangle\langle\eta\rangle\Big). \qquad (1.3.22)\end{aligned}$$

Here, the effective values of the Majorana neutrino mass $\langle m_\nu\rangle$, the square of the mass ratio of the left and right handed weak bosons $\langle\lambda\rangle$ and their mixing $\langle\eta\rangle$ are defined as

$$\langle m_\nu\rangle = \left(\frac{\langle m_{\nu_e}\rangle}{m_e}\right) \qquad (1.3.23)$$

$$\langle\lambda\rangle = \lambda\sum U_{ei}V_{ei}\xi_i \qquad (1.3.24)$$

$$\langle\eta\rangle = \eta\sum U_{li}V_{li}\xi_i \qquad (1.3.25)$$

V_{ei} are the mixing matrix elements for the right handed neutrino states analogous to U_{ei} for the left handed states. ξ_i is the CP phase of the Majorana neutrino ν_i. C_{ij} are the relevant nuclear matrix elements in units of $\left|M^{0\nu}\right|^2$.

Taking a fixed half life limit of a double beta decay one yields an ellipsoid in the parameters $\langle m_\nu\rangle$, $\langle\lambda\rangle$ and $\langle\eta\rangle$ as shown in figure 1.7. The neutrino mass limit which is usually quoted assumes $\langle\lambda\rangle = \langle\eta\rangle = 0$. If $0\nu\beta^+$EC decay would be measured with about the same half life as the claimed evidence from the subgroup of the Heidelberg-Moscow collaboration, then the right two ellipses in figure 1.7 emerge. The solid line represents the $0\nu\beta\beta$ decay and the dashed line the $0\nu\beta^+$EC decay. It can be seen that the free parameter space in this projection can be limited greatly as the two ellipses are almost orthogonal with respect to each other.

Like in single beta decay $0\nu\beta^+\beta^+$ decay is always accompanied by β^+/EC or EC/EC decay. Because of the Coulomb-barrier and the reduction of the Q-value by $4m_e$, the rate for $0\nu\beta^+\beta^+$ is rather small and energetically only possible for seven known nuclides, with ^{106}Cd being one of them. Despite the transition energy being significantly reduced, the transition reveals a good experimental signature. For EC/EC decays lower half lives are predicted, but they are harder to detect experimentally.

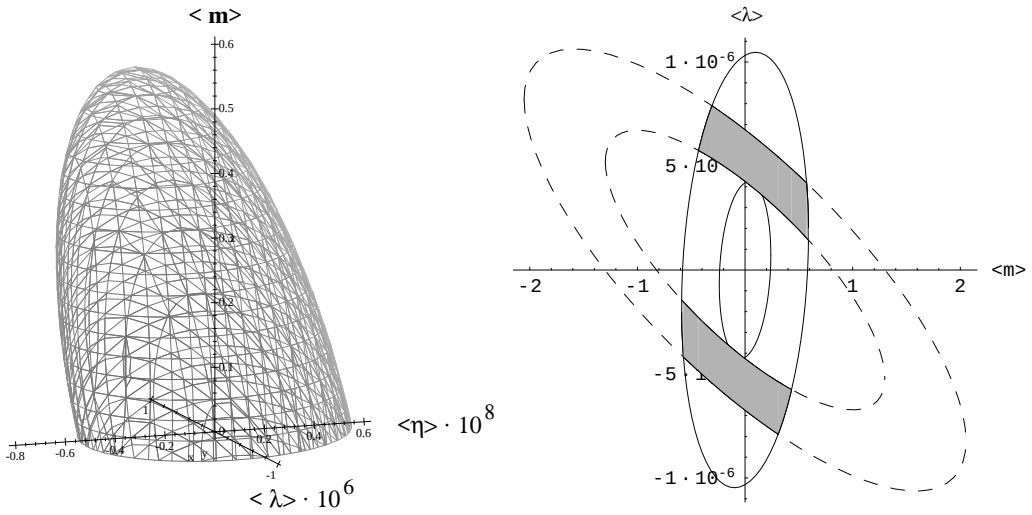

Figure 1.7: In case of right handed weak currents an ellipsoid in the parameters $\langle m_\nu \rangle$, $\langle \lambda \rangle$ and $\langle \eta \rangle$ emerges as shown in the left diagram. In publications usually a simple upper limit is quoted instead. The solid line in the right diagram shows the claimed evidence range of a subgroup of the Heidelberg-Moscow collaboration. The dashed line corresponds to a hypothetical observation of $0\nu\beta^+$EC decay with about the same half life. The two ellipses are almost orthogonal to each other such that not only the neutrino mass, but also the right handed weak current contribution can be measured.

Observation of neutrino-less double electron capture presents a delicate problem as no particles are leaving the nucleus though the energy has to be released somehow. In [Suj03] the possibility of an accompanying photon is discussed. Figure 1.8 shows the corresponding Feynman graph. In normal electron capture such a radiative process has a branching ratio in the order of $10^{-3} - 10^{-4}$ because the introduction of an additional photon in the Feynman graph involves another factor α_{em}, thus increasing the half life. Nevertheless, as this seems to be the only viable method 0νEC EC may be dominated by this radiative effect. On the positive side, the energy of this photon is well defined as the Q-value reduced by the two binding energies of the electrons and thus a clear signal to detect experimentally.

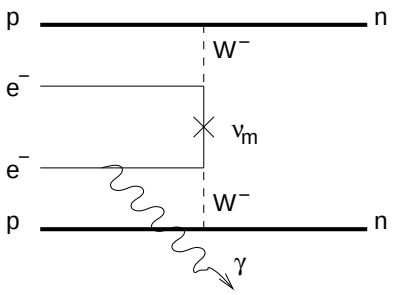

Figure 1.8: Feynman graph of the photon accompanied neutrino-less double electron capture. The additional lepton-photon vertex increases the half life relative to a non-radiative process because of the additional factor α_{em}.

1.4 Exotic Double Beta Decay Modes

Apart from the above mechanisms further models to realise $0\nu\beta\beta$ decay are discussed such as R-parity violating SUSY [Eji01, Goz04] or by additional emission of Majorons [Doi88].
R-parity is a multiplicative quantum number defined as $R = (-1)^{2S+3B+L}$, with B, L the baryon and lepton number and S the spin of the particle. In a minimal supersymmetric standard model (MSSM) this quantity is conserved. Therefore, lepton or baryon number violating processes are strictly forbidden unless the symmetry is broken. However, R-parity is not a fundamental property of SUSY, but has been introduced ad hoc.
As already stated, double beta decay is also thought to be a source of Majorons χ_n [Sch82, Doi88, Boc96]. The Majoron is the Goldstone boson associated with spontaneous breakdown of lepton number conservation. The reaction would be

$$(Z, A) \rightarrow (Z + 2, A) + 2e^- + \chi_n. \tag{1.4.26}$$

As a consequence the spectral shape of the sum electron spectrum would change to

$$S(T) \propto \left(T^4 + 10 \cdot T^3 + 40 \cdot T^2 + 60 \cdot T + 30\right) \cdot T \cdot (Q/m_e - T)^n . \tag{1.4.27}$$

Here, the spectral index n is the factor changing the spectrum, with $n = 1$ for a triplet Majoron, $n = 3$ for a lepton number carrying Majoron and $n = 7$ for various other models [Zub04]. Ordinary $2\nu\beta\beta$ decay is classified with $n = 5$. In figure 1.4 the deformation of the spectra with $n = 1, 3, 5$ and 7 is shown.
The double beta process can also be imagined for the second lepton generation [Kie01, Fla00]. Here, in a ν_μ beam charged current (CC) neutrino-nucleon interactions could take place, where in addition to the μ^- from the CC another muon pair is created according to the Feynman graph in figure 1.9. This pair would have a $\mu^+\mu^+$ signature instead of the usual $\mu^+\mu^-$ pair which comes from Bremsstrahlung or the decay of a meson. The background in such an experiment is determined by the contamination of the beam with $\bar{\nu}_\mu$ which creates a μ^+ together with a $\mu^+\mu^-$ pair.
In the NOMAD experiment [Alt98] such "trimuon" events have been searched for [Kie03]. This search lead to an unphysical limit of

$$\langle m_{\mu\mu} \rangle < 4.8 \cdot 10^3 \,\mathrm{GeV}. \tag{1.4.28}$$

This value is unphysical in the sense that in order to extract the limit propagator effects had to be omitted leading to a naive extrapolation of the curve given in [Fla00]. A more precise measurement of this process can be done in a future neutrino factory experiment [Rod01].

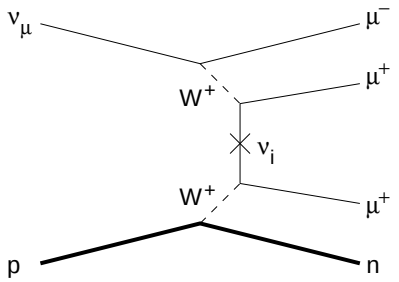

Figure 1.9: Feynman graph of the neutrino-less double beta decay for the second lepton generation. This process can be measured in CC neutrino-nucleon scattering.

Chapter 2

The COBRA Experiment

In 2001 the "COBRA" project, an acronym for **C**admium-Telluride **0**ν Double-**B**eta Decay **R**esearch **A**pparatus, was founded which uses CdTe or CdZnTe semiconductor detectors to measure double beta decays [Zub98, Zub01]. This material has 7 (9 in case of CdZnTe) isotopes which are known to be instable to double beta decay as shown in table 2.1. All these isotopes can be measured simultaneously.

Isotope	Decay mode	Q-value / keV	Natural Abundance / %
^{64}Zn	β^+/EC, EC/EC	1096	48.6
^{70}Zn	$\beta^-\beta^-$	1001	0.6
^{106}Cd	$\beta^+\beta^+$, β^+/EC, EC/EC	2771	1.25
^{108}Cd	EC/EC	231	0.89
^{114}Cd	$\beta^-\beta^-$	534	28.72
^{116}Cd	$\beta^-\beta^-$	2805	7.47
^{120}Te	β^+/EC, EC/EC	1722	0.096
^{128}Te	$\beta^-\beta^-$	868	31.69
^{130}Te	$\beta^-\beta^-$	2529	33.80

Table 2.1: Decay modes, Q-values and natural abundances of isotopes under study [Kie03].

One advantage of CdZnTe as a detector material is that the source of the radiation under study is also the detector ("source=detector" principle), leading to a good detection efficiency. Another advantage is that some of the interesting isotopes like ^{130}Te have a high natural abundance so that it is less important to have an isotopically enriched material, which saves costs. Finally, ^{116}Cd has such a high Q-value of 2.805 MeV that it lies well beyond the highest naturally occurring gamma line of 2.614 MeV. This gamma line stems from the ^{232}Th decay chain and has an emission probability of 35.8 % [Wah96]. Other higher gamma lines do exist, but have emission probabilities below 10^{-4} and are thus suppressed. Therefore, ^{116}Cd has a drastically reduced amount of background in the $0\nu\beta\beta$ signal region. ^{130}Te has a rather high Q-value of 2.529 MeV as well which lies just between the photo peak and the Compton edge of the 2.614 MeV gamma line which means that the background in this region is reduced as well.
In table 2.2 a list of currently proposed or running experiments with their respective proposed sensitivity in half life is shown. A controversial discussion is currently ongoing on the claim of evidence for $0\nu\beta\beta$ decay with the Heidelberg-Moscow detector. For more details see [KK01b,

KK01a, Aal02, Fer02, Zde02]. Following the points of criticism of the claim, it is important to measure $0\nu\beta\beta$ decay with other isotopes than germanium to exclude the possibility that the observed signal is a feature of germanium detectors which is not yet understood.

Experiment	Isotope	Detector Type and Mass	Proposed Half Life / a
COBRA	^{116}Cd, ^{130}Te	10 kg CdZnTe semiconductors	$1 \cdot 10^{24}$
CUORICINO	^{130}Te	40 kg TeO_2 bolometers	$1.5 \cdot 10^{25}$
NEMO3	^{100}Mo	10 kg Mo-foils with TPC	$4 \cdot 10^{24}$
CUORE	^{130}Te	760 kg TeO_2 bolometers	$7 \cdot 10^{26}$
GENIUS	^{76}Ge	1 t enriched ^{76}Ge in liquid N_2	$1 \cdot 10^{28}$
CAMEO	^{116}Cd	1 t $CdWO_4$ crystals in liquid scintillator	$> 1 \cdot 10^{26}$
MOON	^{100}Mo	34 t natural Mo sheets in plastic scintillator	$1 \cdot 10^{27}$
XMASS	^{136}Xe	10 t liquid Xe	$3 \cdot 10^{26}$

Table 2.2: Overview of double beta experiments proposed or currently running with their proposed sensitivities in half life [Zub04].

In the following sections the principle of semiconductor detectors will be explained. An introduction to interactions of charged particles and photons with matter follows. These interactions build the base of the signal generation in the CdZnTe detectors as well as the possibilities on how to screen the detectors from environmental radiation. Taking these principles into account, the construction of a shielding system is then motivated and presented.
Initial investigations with a test setup and the construction of a 26 g prototype module are described. Based on the experience gained with these measurements, the layout of a new 400 g detector of 64 crystals is explained.

2.1 CdZnTe Semiconductor Detectors

CdTe and CdZnTe are intrinsic II-VI semiconductors, i.e. their components are from the 2^{nd} and 6^{th} group in the periodic table of elements. The crystal has a zinc blende structure.
As a particle detector semiconductors work analogously to gas ionisation chambers. When an ionising particle passes the detector it creates electron-hole pairs which are then collected by applying an electric field. The number of electron hole pairs is proportional to the energy deposited in the semiconductor by the ionising particle. The amount of charge carriers produced is also dependent on the band gap between the valence band and the conduction band.
In figure 2.1 the band structures for an insulator, a semiconductor and a metal are shown. The valence and conduction bands contain allowed energy levels for electrons. Energy bands arise from the periodic arrangement of atoms with discrete energy levels, or orbitals, in a lattice. The highest energy band which is completely filled with electrons is called the valence band. If an electron from the valence band gets some amount of energy it may leap the energy gap and reach the conduction band, where it can be seen as a free electron in the material.
For insulators this band gap is so large that no electrons can reach the conduction band by thermal excitation. For semiconductors this small amount of energy is sufficient to excite few electrons from the valence band to the conduction band. For metals both bands overlap so that by adding any small amount of energy the electron is free in the material.

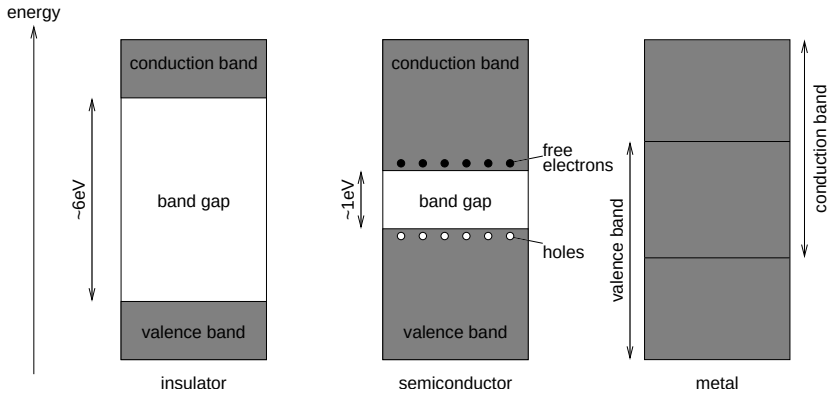

Figure 2.1: Band structure of insulator, semiconductor and metal.

By applying an electric field to a semiconductor, electrons in the conduction band, excited by thermal energy, produce a current in the material. If the thermal energy is decreased by cooling of the material this current decreases as well.

Only few semiconductors can be operated at room temperature, examples are CdTe, CdZnTe and silicon (Si) detectors. Many others like germanium (Ge) detectors have to be cooled for operation otherwise they show a too high current.

As stated in table 2.3, CdTe and CdZnTe have a rather large band gap of 1.6 eV compared to 1.1 eV for silicon or 0.66 eV for germanium. The large band gap results in a lower leakage current, as this defines the number of free charge carriers at a given temperature and Cd(Zn)Te detectors are therefore predestined to be operated at room temperature and need not be doped. The specific resistance of CdZnTe is in the order of $10^{10}\,\Omega/\text{cm}$. Typical bias voltages are dependent on the thickness of the detector and are chosen to be about 1 kV/cm detector thickness.

Semiconductors can be divided into two categories: intrinsic and doped semiconductors. Cd(Zn)Te is an intrinsic semiconductor, which means that the number of electrons in the conduction band and holes in the valence band are the same.

For e.g. Si detectors, the pure material is doped so that additional electrons or holes are created. This creates either so-called donor impurity levels, levels with additional electrons near the conduction band (n-type material), or acceptor impurity levels, levels with additional holes near the valence band (p-type material). Doped semiconductors are usually operated as so-called pn-junction detectors. Here, a material is produced by implanting dopants such that p-type and n-type materials are next to each other. Free charge carriers near the transition of p-type to n-type doping region will recombine. By applying a voltage, this junction works as a diode.

The drift velocity v of the charge carriers in a semiconductor in presence of an externally applied electric field E, depends on a quantity called "mobility" μ. For small electric fields ($E \lesssim 10^3$ V/cm) the relation is linear:

$$v_{e,h} = \mu_{e,h} \cdot E \tag{2.1.1}$$

For stronger electric fields the velocity saturates due to collisions of the charge carriers with the lattice atoms. The values of the mobilities of holes μ_h and electrons μ_e need not be the same, in fact, for CdTe detectors the mobilities differ by more than a factor of 10.

The CdZnTe crystals used for the COBRA experiment are grown with a technique called “high-pressure Bridgman” (HPB) crystal growth [Sze98]. Crystal growth of compound semiconductors is a two step process. First the three elemental constituents Cd, Zn and Te have to be compounded. This happens at a temperature of about 700 °C where a ternary compound is created in an exothermic reaction. Here, already care must be taken to achieve a thorough mixing of the melt to avoid super-heating of the elemental constituents which would rupture the ampoule used to enclose the material. In a second step the compound material is melted and homogenised. For the HPB technique, the crystal, which is also called an ingot, is grown in a crucible, under high pressure of a noble gas – usually argon at 150 bar. This assures a low impurity concentration of less than 10^{16} cm^{-3} because the loss of volatile constituents which would leave from the vapour phase above the melt is highly suppressed. A schematic of the HPB furnace and principle of HPB crystal growth is shown in figure 2.2.

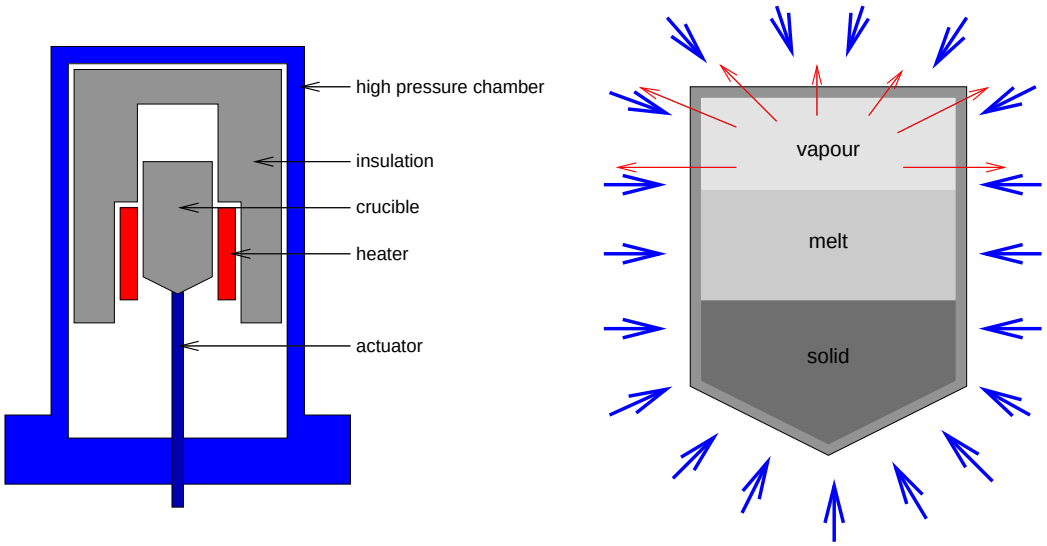

Figure 2.2: The schematic of the HPB furnace is shown on the left side with the crucible being moved by an actuator between the heaters in the high pressure chamber. The right side depicts the process of the HPB crystal growth with the three phases of the material and the external pressure illustrated by blue arrows compensating the vapour pressure of the material indicated by red arrows.

Detectors are produced out of the ingots by cutting slices of material and identifying good mono crystalline zones in these slices. Then the detectors are sawn out of these slices. After polishing and etching of the surfaces, ohmic electrodes of gold or platinum are applied [Cuz87].
CdZnTe detectors are an enhancement of CdTe detectors, created by adding a few percent of Zn, which substitutes part of the Cd and improves the material properties [Chu03]. Thus the correct name would be $Cd_{1-x}Zn_xTe$. However, the Zn content in CdZnTe crystals is not fixed precisely, but changes with position in the ingot from which the crystals are cut. From tip to heel of the ingot the Zn content varies from $7 - 15\%$ [Ton96] with the largest gradients near the ends, so that effectively the variation inside of detectors is smaller.
Table 2.3 shows the material properties of some common semiconductor detectors: CdZnTe, CdTe, Ge, Si and GaAs. The main advantage of Cd(Zn)Te is their large atomic number, which

is important for the cross section of interaction of ionising radiation as explained in section 2.2 in combination with the possibility to operate the detectors at room temperature.

Property	CdZnTe	CdTe	Ge	Si	GaAs
atomic numbers	48, 30, 52	48, 52	32	14	31, 33
average atomic number	49.1	50	32	14	32
average nucleon number	117.6	120.0	72.61	28.09	72.32
structure	zinc blende	zinc blende	diamond	diamond	zinc blende
band gap E_g / eV	1.572	1.5	0.67	1.12	1.43
mean e^--hole pair energy E_{eh} / eV	4.64	4.43	2.95	3.62	4.2
density ϱ / (g/cm^3)	5.78	5.85	5.33	2.33	5.32
e^- mobility μ_e / (cm^2/Vs)	1000	1100	3900	1400	8000
hole mobility μ_h / (cm^2/Vs)	50-80	100	1900	480	400
R_s / (Ω/cm)	$3 \cdot 10^{10}$	10^9	50	$2.3 \cdot 10^5$	10^7

Table 2.3: Physical properties of selected semiconductor detector materials from [Kla99, Eid04, eV-04].

In order to reduce the signal degradation of the detectors leading to low energy tails of peaks mostly due to trapping of holes, different readout techniques have been investigated. One possibility is to use pulse shape discrimination to reject events which show a significant influence from trapped charge carriers [Jon75]. Obviously, this method is associated with a large detection efficiency loss. Another attempt is a charge-loss compensation through sophisticated electronics [Jon75], however, this is adherent with a massive amount of electronics per channel which not only consumes a huge amount of power and space but also significantly increases the price per channel.
Another method called Coplanar Grid (CPG) technology which does not require complicated electronics nor reduces the detection efficiency has been developed [Luk95, Amm99]. With this technique the pure electron signal can be read out. The idea is borrowed from drift chambers where a so-called Frisch Grid is used to discriminate the fast electron signal from the slow ion signal.
In figure 2.3 a schematic of the structured anode of a CPG detector and a picture of a real detector are shown. The cathode is usually planar and connected to the negative bias voltage. The anode consists of two combs with one of the combs being connected to ground and the other one to a small positive voltage of about $10 - 50$ V. If ionising radiation has created a cloud of electrons and holes in the detector volume, the holes are drawn to the cathode and the electrons to the anode. This movement already induces an electric signal at the electrodes due to Ramo's theorem [Ram39]. The induced charge dQ is proportional to the drifting charge q, the Ramo field $\vec{E_R}$ and the drift velocity $\vec{v}_{\mathrm{dr}}$:

$$dQ = q\vec{E}_R(\vec{r})\vec{v}_{\mathrm{dr}}(\vec{r})dt \tag{2.1.2}$$

The signals induced by the drifting of the holes and electrons in the detector is always the same for both anode combs except when the electrons approach the combs. There the electrons are pulled towards the more positive (collecting) anode and almost only induce a signal there. If the signal of the non-collecting anode is subtracted from the signal of the collecting anode, the contribution of the hole signal which is always the same for both anodes, is cancelled out.

The contribution of the electron signal also cancels out in the bulk, leaving only the signal generated near the anode which is proportional to the drifting electrons. So far, there are three generations of the CPG layout. The schematic in figure 2.3 shows the newest generation layout [He98, He03] which is also in used for the COBRA detectors.

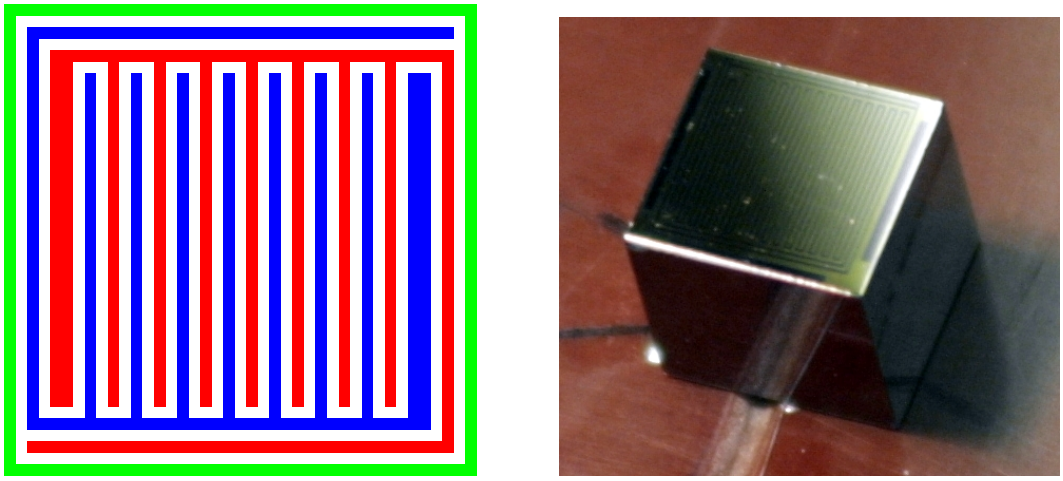

Figure 2.3: The left picture shows a schematic of the Coplanar Grid (CPG) electrode layout [He98, He03]. The two anode combs are drawn in red and blue. A guard ring drawn in green which is used to form the electric field inside the detector is also shown. The right picture shows a $1\,\mathrm{cm}^3$ CPG detector with the gridded electrode visible on the top side.

A guard ring around the anode may also be implemented. It is used to form the electric field inside the detector volume. However, the connection of the guard ring, either to the collecting anode, to ground (i.e. the non-collecting anode) or unconnected ("floating"), has an influence on the active volume of the detector and the signal quality. The optimum solution for the COBRA experiment is still under investigation at the time of writing.

As the detector material is known to degrade over time due to oxidisation processes with oxygen from the air, a passivation paint is applied to the detectors' surface [eV-04]. Only the bare detector material needs to be passivated, such that the planar cathode is left blank. However, the anode grid is completely covered except for the contact pads for the two anode combs and the guard ring. Other means of passivating the surface are currently under investigation.

The size of the detector crystals used in the COBRA experiment as specified by the manufacturer is slightly larger than the nominal $10 \times 10 \times 10\,\mathrm{mm}^3$. Due to tolerances in the processing, the surface in the x-y plane is larger to assure that the electrode will fit fully. The values are specified as $((10.6 \pm 0.1)\,\mathrm{mm})^2 \times (10.05 \pm 0.05)\,\mathrm{mm}$. Using these values and the density of CdZnTe of $\varrho = 5.78\,\mathrm{g/cm}^3$ one yields a mass of $1.13\,\mathrm{cm}^3 \cdot 5.78\,\mathrm{g/cm}^3 = 6.53\,\mathrm{g}$. Table 2.4 gives a list of the masses of 12 detectors recently acquired as central part of the new 64 detector array described in section 2.7. The amount of applied passivation paint has been measured as well by weighing the detectors before and after applying the paint.

Number	Weight / g	Paint / mg
1	6.478	27
2	6.524	24
3	6.593	26
4	6.517	26
5	6.516	24
6	6.477	25
7	6.540	30
8	6.561	30
9	6.516	30
10	6.535	30
11	6.509	28
12	6.511	25
average	6.523	27.1
median	6.516	26.5

Table 2.4: Net masses of twelve CdZnTe detectors and their respective passivation paint masses delivered and weighed by the manufacturer eV-PRODUCTS.

In order to assure a defined quality of the single detectors of the 64 detector array, certain tests have to be done before the detectors can be mounted to their final position in the array. Two measurements will be the energy resolution and active volume of each particular detector. Another method to characterise the detectors is to use the Transient Current Technique (TCT). It makes use of Ramo's theorem mentioned above to measure detector properties such as the mobilities of holes and electrons or the electric field distribution inside a semiconductor. An application of TCT for silicon detectors at the University of Dortmund can be found in [Kra04]. The TCT method has been adapted for testing the quality of the COBRA detectors as described in [Oeh04].
The energy resolution of a detector is usually determined by measuring a mono-energetic signal and calculating the width of the detector response. This is usually done with a fit to a Gaussian distribution

$$\text{Gauss}(x) = \frac{1}{\sigma\sqrt{2\pi}} \exp\left(-\frac{x^2}{2\sigma^2}\right). \tag{2.1.3}$$

Here, the parameter σ denotes the width of the distribution.
The full width at half maximum (FWHM) is also a commonly used measure for the energy resolution $\triangle E$. This value does not depend on the signal being Gaussian shaped. Here, the maximum of a peak is measured, then the two channels to the left and right of the distribution are read off where the bin content is reduced to half of the maximum value. The full width at the tenth of the maximum (FWTM) is sometimes used as well. For a Gaussian distribution the following relation holds:

$$\text{FWHM} = \sqrt{2\ln 2} \cdot \sigma \simeq 2.35 \cdot \sigma. \tag{2.1.4}$$

These and further measurements will provide the necessary input for the classification of new detectors in the upgrade to the 64 detector array.

2.2 Ionising Radiation

The passage of a charged particle through matter is characterised by two features: loss of energy and deflection from the incident direction. This energy loss is the mechanism which is responsible for the signal generation in the CdZnTe detectors. Examples of charged particles are electrons, e.g. from double beta decays and background in form of alpha and beta particles from surrounding radioactive materials or muons from cosmic rays. However, not only their signal generation, but also the possibility to screen the detector setup from background radioactivity can be described by these interactions.

The main interactions causing the above effects are inelastic collisions with the electrons of the atoms and elastic scattering from the nuclei. There are more processes like the emission of Čerenkov radiation, nuclear reactions or Bremsstrahlung, which are however, extremely rare compared with the first two processes and may be omitted for simplicity in the following discussion. A discrimination of two classes of charged particles has to be taken, which are the light charged particles, electrons and positrons, on the one hand and heavy charged particles like muons, pions, protons or alpha particles on the other hand.

The energy loss of heavy charged particles due to ionisation can be described by the Bethe-Bloch equation

$$\left\langle -\frac{dE}{dx} \right\rangle = 4\pi N_A {r_e}^2 m_e z^2 \frac{Z}{A}\frac{1}{\beta^2}\left[\ln\left(\frac{2m_e\beta^2}{(1-\beta^2)\,I}\right) - \beta^2 - \frac{\delta}{2}\right] \tag{2.2.5}$$

with the charge z of the incident particle, the classical electron radius r_e, the atomic number and mass of the absorber (A, Z), the ionisation constant I which is a property of the absorber, a parameter to describe the density effect δ and Avogadro's number N_A. Figure 2.4 shows a graphical illustration of the energy loss in different materials.

The resulting penetration depth of a charged particle as a function of its initial energy can be derived from equation 2.2.5 as

$$\langle R \rangle = \int_E^0 \frac{1}{\left\langle -\frac{dE}{dx} \right\rangle} dE \tag{2.2.6}$$

and is graphically displayed in the right diagram of figure 2.4. As the energy loss depends linearly on the charge of the nuclei, the corresponding curve for Cd(Zn)Te can be estimated by Sn.

The energy loss of electrons in matter differs from that of heavy charged particles because they loose more energy by Bremsstrahlung. The resulting range is graphically displayed in figure 2.5. Again, the range of beta particles in Cd(Zn)Te is estimated to be between the ranges in copper and lead.

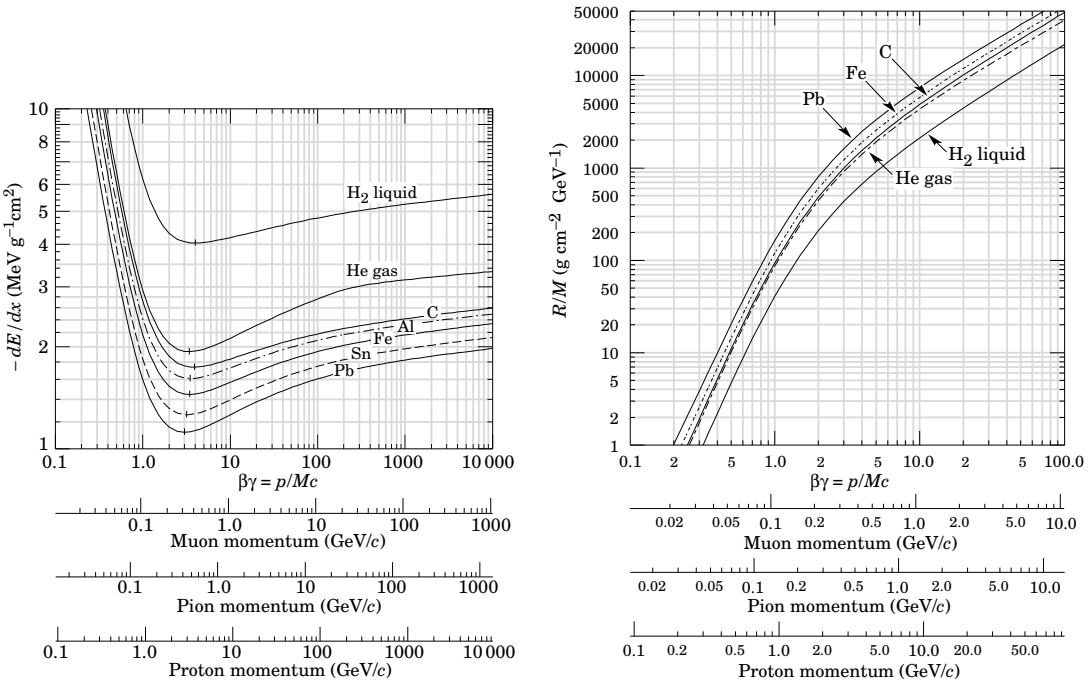

Figure 2.4: The mean energy loss of heavy charged particles in different materials according to equation 2.2.6 is shown in the left diagram. The right graph shows the resulting range of heavy charged particles in these materials [Eid04]. For both values the density of the material has to be considered, and for the range also the mass of the particle. CdZnTe can be approximated by tin, between lead and iron.

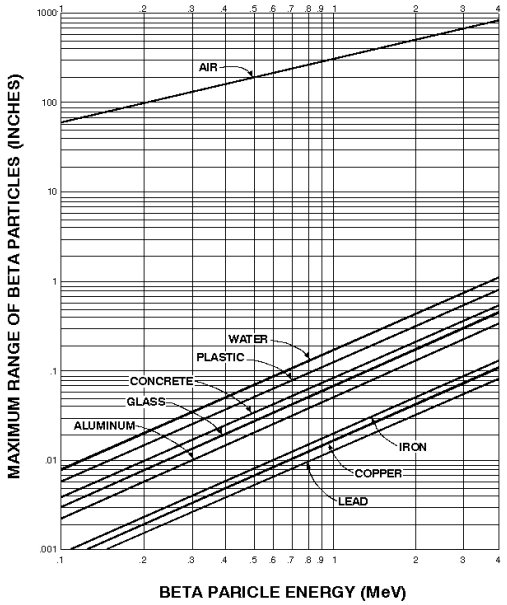

Figure 2.5: Range of beta particles in different materials [Shu02]. The range in Cd(Zn)Te lies between copper and lead.

Considering double beta decay of ^{116}Cd, the maximal kinetic energy of one electron is 2.8 MeV if the other one gets almost no energy. The resulting range of this electron in CdZnTe is then approximately 1.5 mm. Another interesting decay is the single beta decay of ^{113}Cd with a Q-value of 320 keV. For a 300 keV electron the range would be about 0.08 mm.
Photons behave completely different opposed to charged particles. Their interactions with matter, the photoelectric effect, Compton scattering and pair production, are discrete processes. Except for Compton scattering, these effects do not reduce the energy of the incident photons, but their number. Thus, the intensity of a photon beam I is attenuated exponentially with the thickness x of an absorber with an absorption coefficient μ.

$$I(x) = I_0 \exp(-\mu x) \tag{2.2.7}$$

In the photoelectric effect the entire energy of a photon is absorbed by a bound electron. If the energy of the photon E_γ exceeds the binding energy E_b of the electron in the atom, the electron will leave the atom. The excess energy is carried away by the electron as kinetic energy

$$E_e = E_\gamma - E_b. \tag{2.2.8}$$

It has to be mentioned that this process is only possible for bound electrons where the nucleus absorbs the recoil, as for free electrons energy and momentum cannot be conserved at the same time in this process.
For free or quasi free electrons which are less bound elastic scattering is the preferred interaction. Thomson scattering is the interaction of a photon on a free electron in the classical limit, Rayleigh scattering is the interaction of a photon with an atom as a whole and Compton scattering is the interaction of a photon with a less bound electron. In all these cases the photon is not absorbed, but only deflected by an angle θ. Thus, after the interaction the electron carries away only a part of the photon energy. The remaining energy of the photon after the elastic Compton scattering is calculated as

$$E' = \frac{E}{1 + \gamma(1 - \cos\theta)} \qquad \text{with} \quad \gamma = \frac{E}{m_e}. \tag{2.2.9}$$

Here, the energy of the struck electron $E_e = E - E'$ has a maximum value of

$$E_e = \frac{2E\gamma}{1 + 2\gamma} = \frac{2E^2}{m_e + 2E} \tag{2.2.10}$$

which is called the Compton edge. For the 2.614 MeV gamma from the ^{232}Th decay chain, this leads to a Compton edge of 2.381 MeV. As stated before, the endpoint of the double beta decay of ^{130}Te lies at 2.529 MeV, just between the Compton edge and the photo peak and therefore profits from an intrinsically reduced background.
Pair production is the conversion of a photon into an electron-positron pair. Of course, this process has a threshold of two times the electron mass $2m_e = 1022$ keV. Additionally, a nucleus has to be present to make momentum conservation possible.
For small detectors the conversion of a photon into an electron-positron pair leads to effects called single and double escape peaks (SE, DE). Here, the electron and positron deposit their total kinetic energy in the detector, due to their limited range. The positron then annihilates at rest with another bound electron and two 511 keV gammas are produced. Now, one or both

gammas may escape, because the mean free path for gammas is larger than for electrons, so that two peaks arise in a measured spectrum at $E_\gamma - 511\,\text{keV}$ (SE) and $E_\gamma - 1022\,\text{keV}$ (DE). In figure 2.6 the total photon cross section is shown for lead and the resulting attenuation length for different materials.

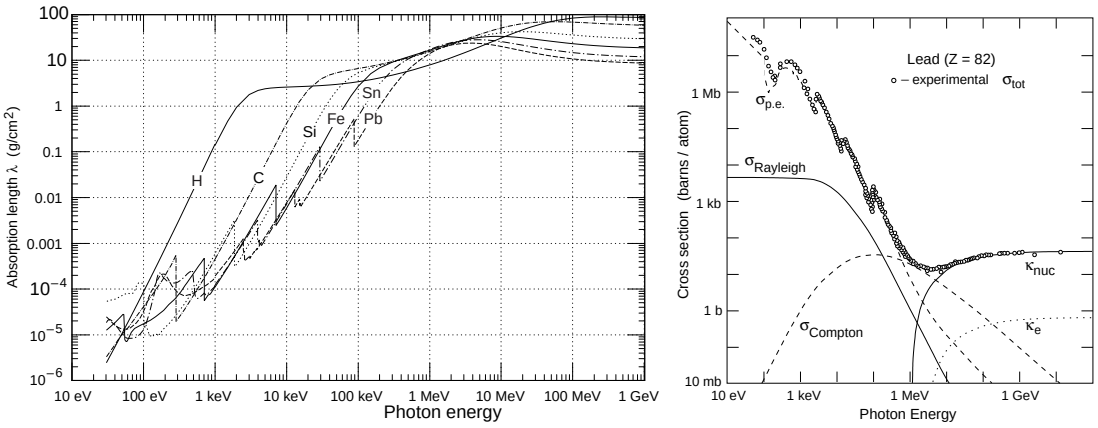

Figure 2.6: The photon mass attenuation length or mean free path for different materials is shown in the left graph. The right graph shows the total photon cross section in lead, indicating also the contributions of the photo effect σ_{Photo}, Compton scattering σ_{Compton} and pair production in the field of a nucleus κ_{nuc} and in the field of an electron κ_{e} [Eid04]. The kinks denote the K, L and higher shells of the absorber.

The dominant process of the photon interaction as a function of energy is shown in figure 2.7. For CdZnTe, a material with a mean Z of 50, Compton scattering is the dominant process over a wide range of the photon energy from 250-7000 keV. For lead, a good shielding material, the photo effect is the dominant process up to 550 keV. Compton scattering is then the dominant process up to 5.5 MeV.

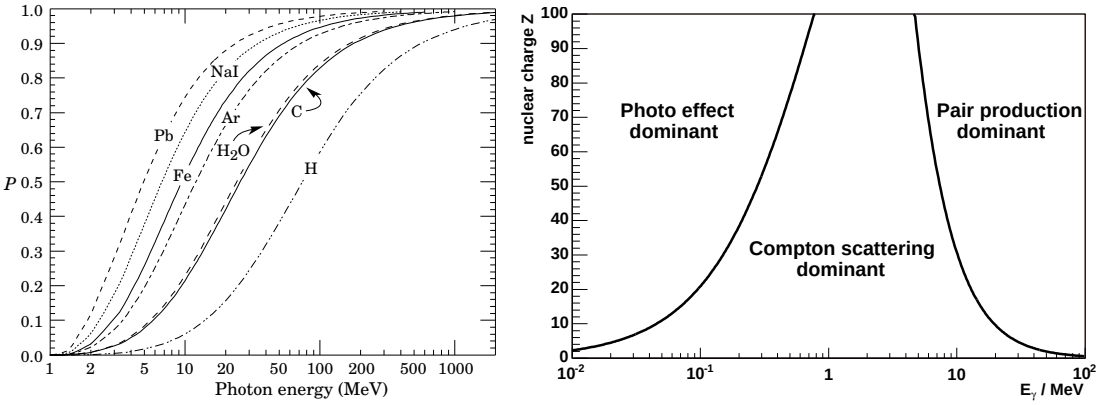

Figure 2.7: The left graph shows the photo pair production probability κ_{nuc} [Eid04]. The corresponding graph for CdZnTe would lie between NaI and lead. The right diagram shows the dominant photon interaction process as a function of the photon energy E_γ and the nuclear charge Z of the absorbing material.

Photons are mainly produced as background, however, signal events may contain photons as well. Examples are double beta decays to excited states where the excited daughter nucleus emits a gamma ray, or the annihilation of β^+ positrons into two 511 keV gammas.

2.3 Detector Arrangement

From the above interactions the optimal geometry for a detector setup can be deduced, i.e. for larger detectors the detection efficiency is increased. However, current crystal growth methods limit the size of a single CdZnTe detector to about 1 cm^3 which corresponds to roughly 6 g. Larger crystals of up to 16 cm^3 of the same quality exist, but are disproportionally more expensive. Therefore, in order to reach a competitive mass in the order of some tens of kg many small detectors have to be deployed. This granularity may seem like a burden. However, the track length of electrons from double beta decays in the detector is in the order of a millimetre, so that such a detector can be favourably used for background rejection by analysing coincidences between crystals.
For a small ensemble of detectors a 2-dimensional configuration is ideal as all crystals are easily accessible. However, a larger amount of crystals must be arranged in a 3-dimensional array to get the maximum efficiency to see coincidences of multiple detectors.
This 3-dimensional setup may consist of several 2-dimensional modules which can be stacked vertically together as illustrated in figure 2.8. This technique maintains the advantage of easy accessibility of the single detectors while achieving the full detection efficiency of a 3-dimensional array. Another advantage of a 3-dimensional array is that the surrounding shielding can be optimised for a minimal surface compared to a large 2-dimensional array. This reduces the surface and volume of the surrounding shielding material.

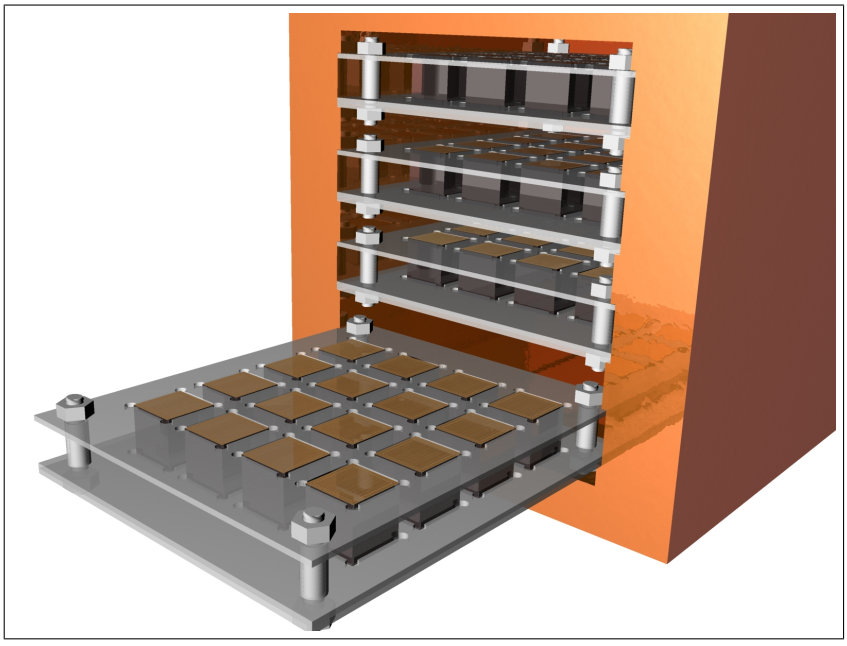

Figure 2.8: Virtual model of the $4 \times 4 \times 4$ Prototype array, an arrangement of 64 detectors in 4×4 arrays on 4 shelves. By courtesy of Daniel Dobos.

2.4 Background Components and their Shielding

As double beta decays are amongst the rarest processes in nature, the vast amount of background events from the environment would obscure the physically interesting events unless shielded. Therefore, much effort has to be put into designing an efficient shielding system which may consist of both active and passive parts. Again, the interactions described in section 2.2 have to be considered to build an efficient shielding system.
There is a large number of possible background sources, like the natural decay chains, neutrons, muons or cosmogenics. Muons are the most penetrating background generated by cosmic and solar particles hitting the upper atmosphere of the earth. These reactions produce mesons which then decay into muons. They, therefore, need the largest shielding. Instead of stopping the muons to prevent them from reaching the detector plastic scintillators can be utilised as an active veto to shield the setup.
Cosmogenics are radioactive nuclei produced by mesons and muons in any material on the earth's surface. Therefore, it is necessary to not only to tag events in the detector coincident with a passing muon, but shield the materials completely from cosmic rays. Usually, the produced isotopes are short lived so that by storing the materials for a few years in a cosmic ray reduced environment, the contamination diminishes by itself. α, β and γ rays produced in the natural decay chains of ^{238}U and ^{232}Th are far less energetic than cosmic muons. The simplest passive shielding can be done by placing the detectors inside a thick pure lead shield.
Neutrons can be shielded by placing material around the setup which has a large cross section for neutron capture. A competing process to neutron capture is elastic scattering. Here, the neutrons are only moderated, i.e. their energy is reduced, but not the flux. This process can be used as part of the overall shielding as many materials have higher capture cross sections for low energy neutrons, thus by moderating the neutrons in the material their capture cross section increases. In the following sections the above background sources are discussed more in detail.

2.4.1 Underground Laboratory

The main background stems from cosmic background, like atmospheric muons and hadronic showers. Instead of vetoing events coincident with a muon traversing the plastic scintillators mentioned above, the muon flux can also be suppressed by a massive shielding, i.e. by going underground as such a massive shielding cannot be built.
In figure 2.4 the dependence of the penetration depth of a particle and its incident momentum is shown according to the Bethe-Bloch formula in equation 2.2.5. The flux of atmospheric muons has a maximum at about 100 GeV [Ach04], however, the spectrum extends to several TeV. Taking a muon with an energy of 10 GeV which is the maximum possible energy to read from figure 2.4 and rock with a density of $\varrho = 2.5\,\mathrm{g\,cm^{-3}}$ as a shielding material, the resulting penetration depth already yields 160 m. This implies that a deep underground laboratory has to be used to suppress the muon flux significantly.
About a dozen laboratories exist in the world that are located deep underground in mines or tunnels with a thick enough shielding from covering rock to absorb the muon flux significantly. The muon flux as a function of depth is shown in figure 2.9 [Bug98]. Though the muon flux from atmospheric muons is decreasing with depth, at a certain depth the absolute muon flux will not decrease anymore. This is because at that depth neutrino induced muons dominate

the flux. The muon flux from neutrinos as measured in the Gran Sasso laboratory is $I_\mu^\nu = (2.98 \pm 1.15) \cdot 10^{-13}\mathrm{cm}^{-2}\mathrm{s}^{-1}\mathrm{sr}^{-1}$ [Agl95] which agrees well with the world average from [Bug98] of $2.17 \cdot 10^{-13}\mathrm{cm}^{-2}\mathrm{s}^{-1}\mathrm{sr}^{-1}$ or about 1 muon per m^2 per year.

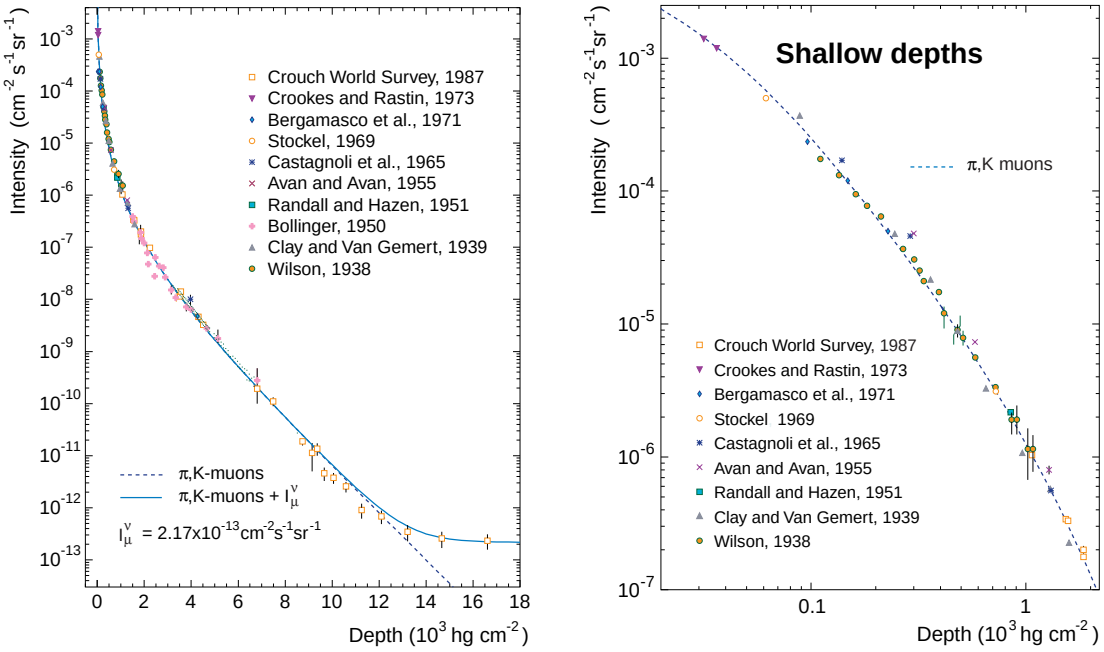

Figure 2.9: Muon intensity versus standard rock thickness in mWE [Bug98]. The markers are measurements, the dashed line represents the depth-intensity relation of the muon flux from pions and kaons, the solid line includes neutrino induced muons with a fitted muon flux of $I_\mu^\nu = 2.17 \cdot 10^{-13}\mathrm{cm}^{-2}\mathrm{s}^{-1}\mathrm{sr}^{-1}$ which corresponds to approximately 1 muon per m^2 and year.

In order to be able to compare the shielding of different sites covered with different types of rock of varying densities, the amount of material above such a laboratory is normalised to a water column with the same shielding power. The unit is called meters water equivalent (mWE). Table 2.5 shows an overview of some of the more important underground laboratories.

Laboratory	Country	Depth / m	Depth / mWE	Type
UDO	Germany	925	2100	mine
Soudan	USA	710	2100	mine
Canfranc	Spain	900	2450	tunnel
Kamioka	Japan	1000	2700	mine
Boulby	UK	1100	3000	mine
Gotthard	Switzerland	1600	3700	tunnel
Gran Sasso	Italy	1400	3800	tunnel
Homestake	USA	2300	4200	mine
Fréjus	France	1700	4800	tunnel
Sudbury	Canada	2039	6000	mine

Table 2.5: Incomplete list of underground Laboratories sorted by their effective shielding in mWE.

The COBRA experiment is located in the Laboratori Nazionali del Gran Sasso (LNGS) which is situated in the Abruzzo region in Italy about 120 km east of Rome. It consists of an outer laboratory with offices, workshops and administration, a subterranean laboratory in a motorway tunnel through the Gran Sasso massive where most of the experiments are located and an additional laboratory on top of the mountain at the Campo Imperatore. The subterranean laboratory is located at about 6 km from the west side entrance of the 10.4 km long tunnel connecting L'Aquila and Teramo. The underground laboratory consists of three large halls (A, B and C) and connecting tunnels with a total area of about 1800 m^2 as shown in figure 2.10. The COBRA experiment itself is located in a container in one of the side tunnels behind Hall A.

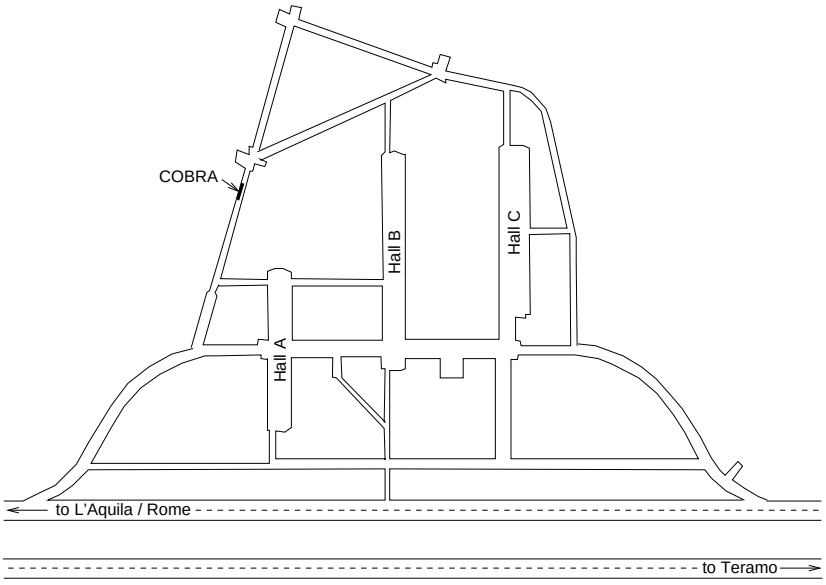

Figure 2.10: Map of the LNGS subterranean laboratory with the location of the COBRA experiment.

In the underground laboratory the muon flux is reduced to about $10^{-8}\mathrm{cm}^{-2}\mathrm{s}^{-1}\mathrm{sr}^{-1}$ which corresponds to $\sim$4 muons per hour and m^2 [Agl03]. This is a factor 10^6 less than at the surface. The neutron flux is also about 1000 times lower than at the surface because of the low activity from dolomite rock. The laboratory is run by the Italian Istituto Nazionale di Fisica Nucleare (INFN).
Short lived isotopes may be activated by cosmic ray activation. Therefore, unnecessary airborne transportation of the detectors should be avoided. Also storing the detectors and shielding material underground prevents them from being activated and already produced short lived isotopes may decay prior to starting the measurement period. The activation of CdTe by cosmic rays has been investigated at the SATURNE accelerator in Saclay, France using a 1.7 GeV proton beam [Por96]. In table 2.6 a list of long lived isotopes with a half life larger than 50 days is shown. These radio-impurities do not pose an impact on the measurement of the $0\nu\beta\beta$ decay of ^{116}Cd with a Q-value of 2.8 MeV. Actually, none of the isotopes listed in [Por96] has a significant gamma line beyond the Q-value of ^{116}Cd. However, they are important for the measurement of lower energetic transitions. Isotopes with a shorter half life are of little importance because their activity will fade away in a short period of time.

Isotope	Half Life / d	Decay Mode	E_γ / keV	Emiss. Prob. / %	Cross Section / mb
^{124}Sb	60.2	β^-	603	98	6.2±0.4
			1691	50	
^{121m}Te	154	EC, β^+, IT	212	81	5.4±0.6
^{110m}Ag	250	β^-	658	95	3.4±1.4
^{95m}Tc	60.2	EC, β^+	204	64.2	1.7±0.4
^{88}Zr	83.4	EC	393	94.5	14.5±0.6
^{88}Y	107	EC, β^+	898	94	3.3±0.5
			1836	99	
			2734	0.71	

Table 2.6: List of the long lived ($T_{1/2} > 50$ d) proton-induced radionuclides in CdTe measured with a 1.7 GeV proton beam on a CdTe target [Por96]. The half lives and characteristic gamma lines are shown as well as the production cross section.

2.4.2 Inner Shield

In order to protect the detector from environmental radioactivity from the natural decay chains as shown in appendix A, radon, ^{40}K as shown in figure 2.11 and other long lived isotopes in the surroundings of the detectors, copper and lead are ideal shielding materials. Because of their large density and rather high nuclear charge, their efficiency in absorbing high energy gammas from these decays is large. Additionally, especially copper can be produced very clean, i.e. it contains less that 10^{-10} g / g radioactive isotopes.

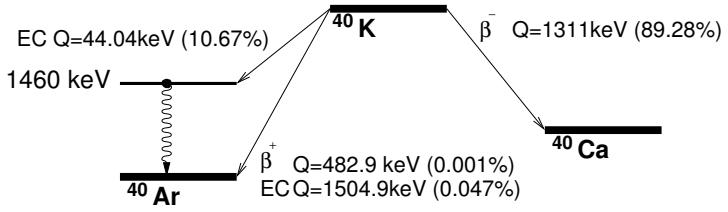

Figure 2.11: Decay scheme of ^{40}K [Chu99], which mainly decays into ^{40}Ca (89%). In 10% of the cases it decays into an excited state of ^{40}Ar which then de-excites by emitting a 1460 keV gamma. Both daughter nuclides are stable.

The innermost parts of the detector usually cannot be shielded so that clean materials have to be used here. The four 1 cm^3 detectors used in the LNGS since August 2003 are mounted on a Pertinax holder in a copper brick as shown in figure 2.12. The copper brick already acts as a passive shielding and is surrounded by another 10 cm of electro-polished copper and a further shielding of 20 cm of lead.
All electronics components, which basically means the preamplifiers, have been removed from the vicinity of the detectors. They are located about 25 cm from the detectors outside the lead shielding.
The innermost layer of the shielding is made of copper, as it can be produced cleaner than lead. However, lead is cheaper and has a larger cross section because of its higher atomic number Z so that it is used as the next layer, which is even more massive, because the volume and therefore the mass scales with r^3.

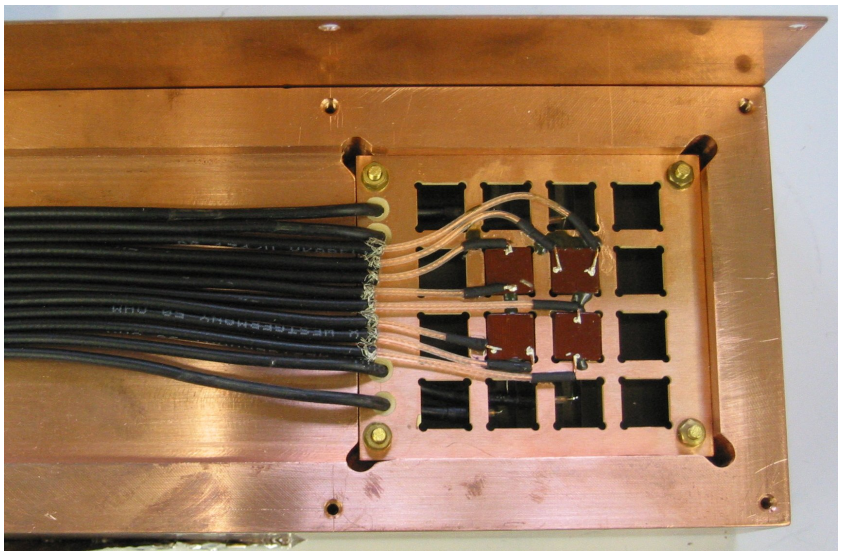

Figure 2.12: Picture of the 2×2 array in its Pertinax holder. The anodes on the top side are connected with silver loaded epoxy to the LEMO cables, whereas the cathode on the lower side is contacted with wire bonds which are glued with silver-epoxy to the electrode. This bond was by accident soldered to the LEMO cables. The Pertinax holder was designed to host up to 16 detectors.

In figure 2.13 the first build up of a lead and copper shielding is shown. For maintenance reasons the copper brick containing the detectors can be removed from the shielding without major modifications of the lead and copper shield. The setup must also be accessible for calibrations at regular intervals. Therefore, the copper brick above the detectors' brick was machined to host a holder for radioactive sources, which is accessible without modifying major parts of the shield as well.

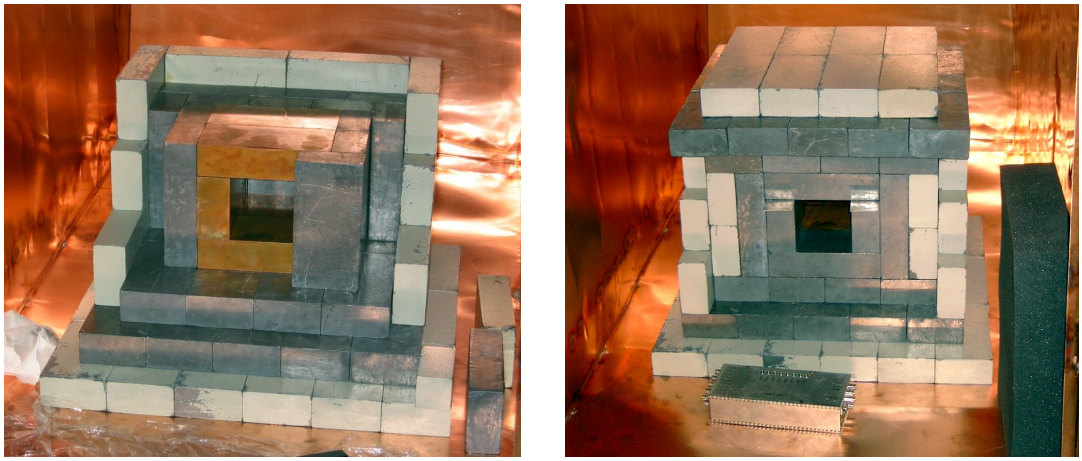

Figure 2.13: Picture of the lead and copper shielding during a first build up. In a later step the bricks coated with paint have been replaced by other non-varnished bricks. The whole lead and copper shield is located in an air tight Faraday cage made of copper sheets.

Another disadvantage of lead is that it usually contains ^{210}Pb which comes from the natural decay chain of ^{238}U. Its decay produces a low energy gamma of 46.5 keV, betas up to 1.161 MeV and an alpha of 5.305 MeV [Wah96]. The most problematic item is the 1.161 MeV beta which produces Bremsstrahlung up to this energy. However, the detector may be shielded from this radiation by a copper shield as stated above. As the half life is "only" $T_{1/2} = 22.3$ a the quality of the lead increases with time if it is stored underground. Therefore, some experiments use archaeological lead from sunken roman galleys. The covering water prevented the lead from being activated by cosmic rays.

2.4.3 Faraday Cage & Airlock

In order to protect the critical signal lines from the detectors to their preamplifiers against high frequency (HF) disturbances, a Faraday cage has been installed which can be seen in figure 2.13 as well. The cage is also air tight and can be flushed with nitrogen to avoid surface contamination from radon. However, the flushing with evaporating liquid nitrogen has not yet been installed.

In order to optimise the flushing, the nitrogen has to be guided by Teflon tubes to the innermost part of the detector shielding, as otherwise the volume to flush would be too large. The flushing with nitrogen can also be used to cool the detectors down to about 0 °C to improve their energy resolution.

Flushing the setup with nitrogen from bottles is not beneficial, as the gas contains a lot of radioactive radon.

2.4.4 Neutron Shield

A major component of the environmental radioactivity in the underground laboratory of the LNGS are thermal neutrons from the rock. They are produced as fission products of uranium and thorium and (α, n) reactions in the concrete and rock.

For the COBRA experiment this background is of great importance because the cross section for thermal neutron capture in ^{113}Cd is one of the highest of all isotopes. The cross section as a function of the neutron energy is shown in figure 2.14. The reaction is ^{113}Cd (n,γ) ^{114}Cd which produces gammas up to 9 MeV [Chu99]. The cross section for thermal neutron capture is about $2 \cdot 10^5$ barn [McC93].

In order to reduce the neutron flux, a two component shielding is usually used. Firstly, the high energy neutrons are moderated by a material with light nuclei. In a second step, the thermal neutrons are captured in a material which contains an isotope with a large capture cross section for thermal neutrons. In shieldings for nuclear reactors this is done using cadmium foils with ^{113}Cd. However, as this isotope is an integral part of the detector material, cadmium foils cannot be used for the COBRA experiment, as otherwise the gammas from the shielding and those of reactions in the detectors are indistinguishable. Fortunately, there are other isotopes like ^{10}B and ^{6}Li which also have a large capture cross section for thermal neutrons. Another advantage of ^{10}B is that neutron capture does not involve the emission of high energy gammas for this isotope.

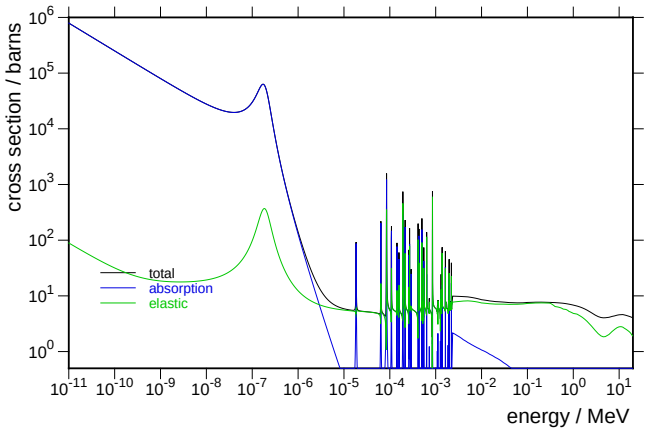

Figure 2.14: The absorption reaction ^{113}Cd (n,γ) ^{114}Cd has a large cross section of about 20000 barn for thermal neutrons [McC93] with an energy dependence as shown.

The neutron shield is installed outside the Faraday cage mentioned in the previous section. It consists of 7 cm thick boron loaded polyethylene (PE) plates and an additional 20 cm of paraffin wax at the bottom and sides. The paraffin, containing a huge amount of hydrogen, is used as a moderator thermalising the fast neutrons. The boron loaded polyethylene is then used to capture the thermalised neutrons. A schematic of the neutron shield is shown in figure 2.15.

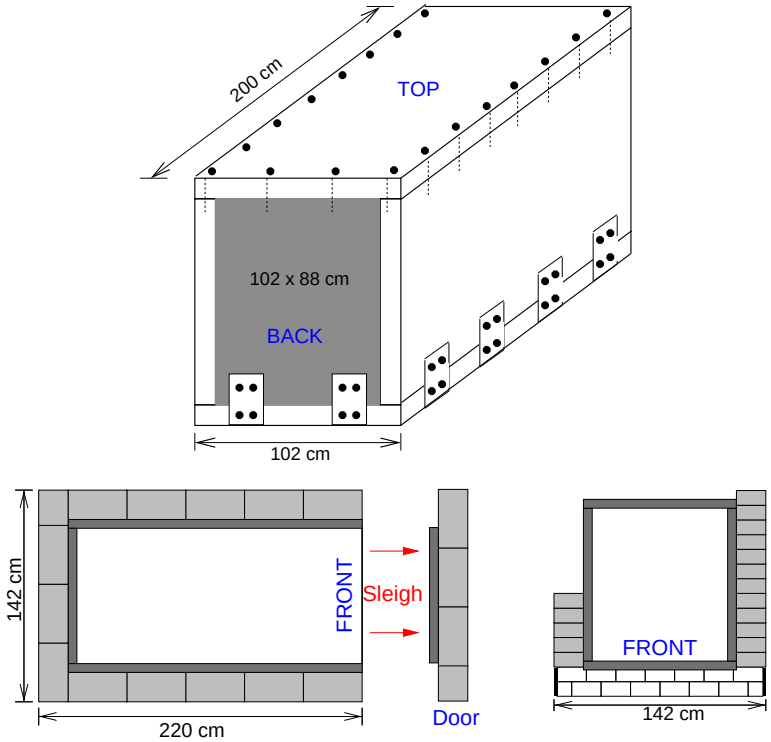

Figure 2.15: The top sketch shows the boron loaded polyethylene shield with the position of the screws and mounting links. The sketch at the bottom illustrates the stacking of the paraffin bricks outside the PE shield from above (left sketch) and from the front (right sketch) [Oeh04].

The shielding material, both the borated PE plates and the paraffin bricks were kindly provided by the Forschungszentrum Karlsruhe. The PE shield and the bottom layer of paraffin has been installed in March 2004 and the 20 cm thick side walls of paraffin were installed in December 2004. The current state of the neutron shield is shown in figure 2.16.

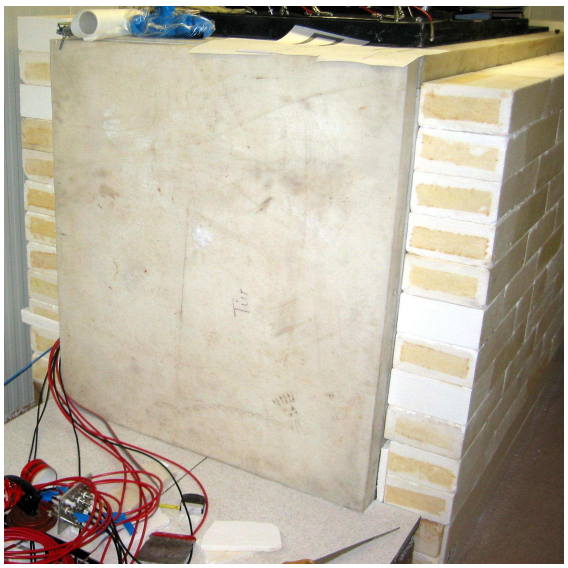

Figure 2.16: Picture of the neutron shielding with the paraffin bricks around the borated polyethylene plates. The top layer and door are missing. Instead the borated polyethylene front plate can be seen. To the bottom left of the front plate the cabling of the detectors, i.e. their high voltage and signal lines, is passed through the neutron shield. The shield can be opened by sliding the front plate away.

The weakest parts of the neutron shield are now the front door and the top plate where the shielding consists only of the 7 cm PE. The door has not yet been built because of space limitations. Extensive simulations and the design of the neutron shield are elaborated in [Oeh04]. A short review of the simulation is presented in section 4.1.

2.4.5 Active Veto

When charged particles pass through a scintillating material photons in the visible range are produced which can be read out via photomultiplier tubes [Kno79]. By building a layer of scintillators around the setup charged particles which pass the inner volume of the setup can be detected.
The veto signal of the test setup in Dortmund sketched in figure 2.17 is generated by charged particles traversing the two layers of plastic scintillators on the top or one of the layers at the sides. The signals of the double layer on the top are linked together in a coincidence. The signals of the single layers at the sides and the coincidence signal of the double layer are then 'OR'ed together. The resulting signal triggers a timing unit which generates a 20 μs long veto signal. The whole electronics for the veto system, such as threshold, logic and timing unit, are NIM[1] modules [Leo92].

[1] **N**uclear **I**nstrument **M**odule [Cos73]

Before the installation of the neutron shield, the active veto was installed in the LNGS setup, but was not activated. In favour of the space requirements of the neutron shield the active veto had to be removed. This was possible, because the background reduction of an active veto is only marginal in an underground laboratory due to the reduced muon flux.

2.5 Initial Tests

Before a prototype can be installed in an international laboratory certain basic tests have to be performed to justify the space and financial requirements. These tests have been carried out at the University of Dortmund in 2001.

Different types of test detectors have been purchased. Two of them were CdTe detectors with planar electrodes from EURORAD[2], with $9.83 \times 9.83 \times 10\,\mathrm{mm}^3$ (E1) and $9.83 \times 9.83 \times 3\,\mathrm{mm}^3$ (E2), and one nominal $10{\times}10{\times}5\,\mathrm{mm}^3$ CdZnTe detector with Coplanar Grid technology (CPG2) kindly provided by eV-PRODUCTS[3].

The CPG2 detector was a complete, encapsulated detector with its preamplifier integrated inside the housing. E1 and E2 were bare detectors, i.e. just the plain crystals with short wires connected to the electrodes.

The bare detectors have been mounted in a small copper box also acting as a Faraday cage. The cylindrical casing of the CPG2 detector has a radius of $1\frac{1}{4}'' = 31.75\,\mathrm{mm}$ and a length of 130 mm. The detector is mounted at one end of the casing and is shielded by a 13 mm thick tungsten cylinder from the electronics which are located at the other end of the casing.

These detectors have been placed inside a 20 cm shield of copper bricks which are surrounded by a further 30 cm of lead bricks. These bricks were etched with HCl and HNO_3 acids and cleaned in an ultrasonic sound bath with ethyl alcohol and acetone. The whole passive shielding is surrounded by an almost 4π active veto of plastic scintillators, with a double layer on top and single layer on the four sides. The scintillators are mounted on an air tight box which was constantly flushed with nitrogen to protect the apparatus from ^{222}Rn. A schematic of the setup is shown in figure 2.17. The whole setup is located inside a building with barite concrete walls and ceilings.

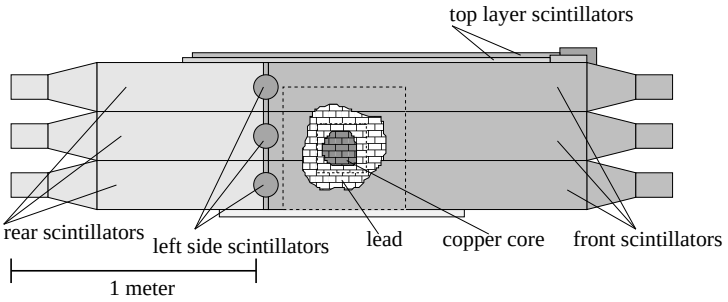

Figure 2.17: Schematic of the COBRA test setup in Dortmund [Mue01, Kie03]. The detectors were located inside a copper and lead shielding with a surrounding air tight box on which scintillator paddles were mounted on five sides, i.e. the top and four sides.

[2] http://www.eurorad.com/

[3] http://www.evproducts.com/

In figure 2.18 the efficiency of the active veto of plastic scintillators installed in Dortmund is shown. It can be seen that the background is reduced to about a factor of 10^{-2} over the whole spectrum revealing the previously obscured rare 4-fold forbidden beta decay of ^{113}Cd with an endpoint of $Q \simeq 320\,\text{keV}$ and a half life $T_{1/2} \simeq 10^{16}$ years. First measurements of double beta decays have been published in [Kie03] already resulting in world best limits on the neutrino-less double beta decay of some isotopes.

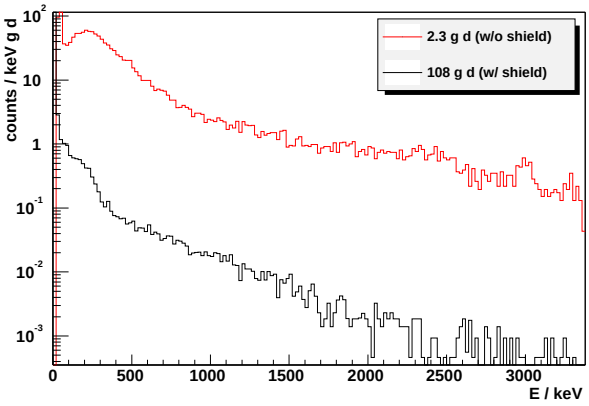

Figure 2.18: The efficiency of the active veto system is illustrated for the setup in Dortmund with the CPG2 Detector. The red histogram indicates the background level obtained with a 2.3 g·d of measurement without the shield. The black line shows a measurement with the active veto. The statistics of this measurement is 108 g · d. A significant reduction of the background component of about two orders of magnitude over the whole spectrum can be seen.

2.6 The 2×2 Prototype

The 2×2 array of 1 cm^3 CdZnTe detectors in a Pertinax (FR2, hard paper) holder was designed with scalability in mind. Therefore, the Pertinax holder is large enough to hold 4×4 detectors. In figure 2.19 different views of the Pertinax holder with the detectors and their cabling are shown. The detectors are contacted with silver epoxy to bonding wires. These bonding wires are then connected to LEMO cables, unfortunately using solder which usually contains radioactive isotopes. The LEMO cables are fixed to the top Pertinax grid with super glue (cyanoacrylate) as a strain relief. The numbering of the detectors D1−D4 has been superimposed on the left picture.

The Pertinax holder was removed in a later step and substituted with almost the same structure, but with Delrin (Polyoxymethylene (POM)) as a material. The technical drawings of the new Delrin holder are shown in appendix B. This measure was taken, because the radioactive content of Pertinax was measured on a low level germanium counter showing vast amounts of ^{137}Cs [Lau04] as shown in appendix C. Also during remounting the soldering points in the vicinity of the detectors were removed. In figure 2.20 the new Delrin holder with the mounted detectors, as well as the new Kapton cables are shown. A more detailed discussion can be found in [Mue05].

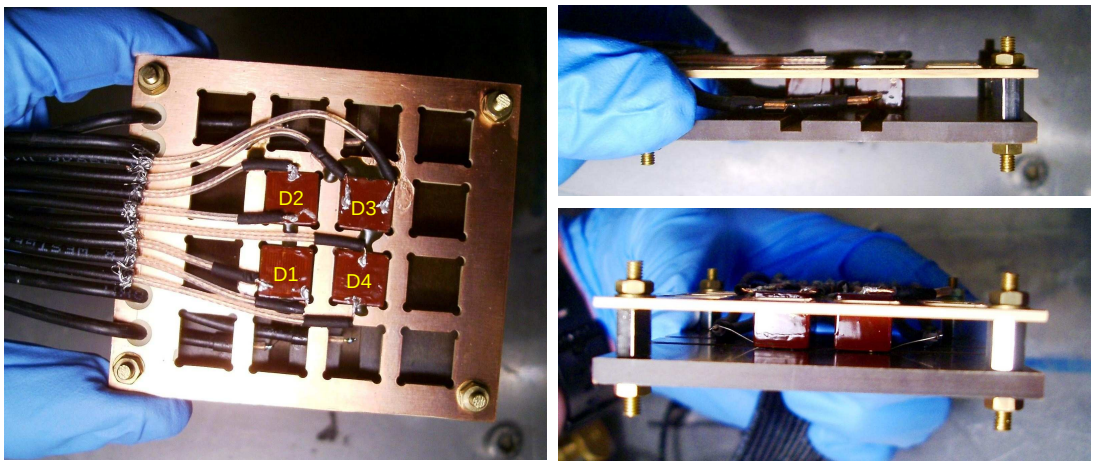

Figure 2.19: The 2×2 Prototype array in the Pertinax holder is shown from the top and the two sides. Clearly visible are the positions of the cables and their fixation. The glued ends of the LEMO cables are insulated with heat shrinkable tubes from the copper coated Pertinax sheets. The base and guiding plates are separated with brass screws. The numbering of the detectors is shown in yellow.

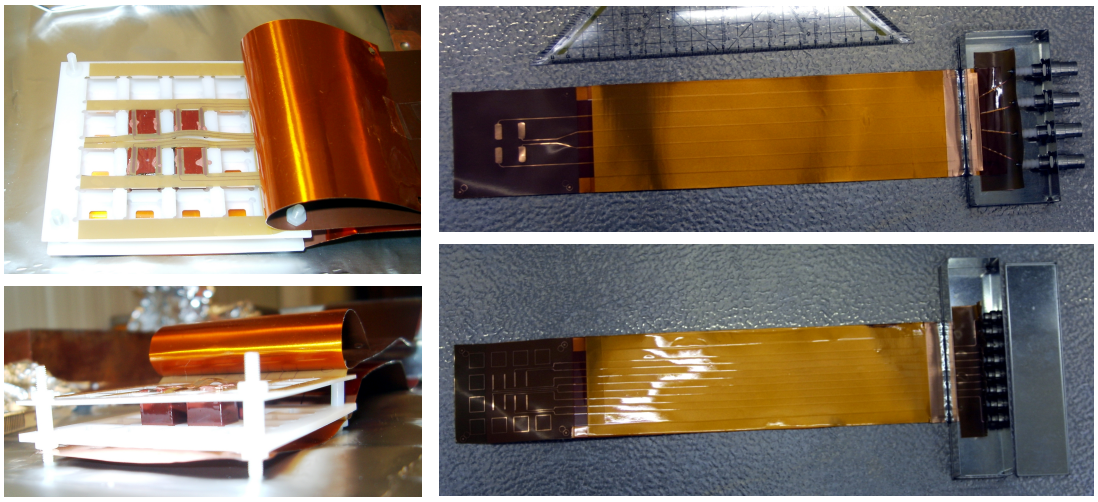

Figure 2.20: The remounted 2×2 Prototype array in the Delrin holder is shown from the top and side in the left two pictures. The glued Kapton cable at the anode side can be seen in the top picture. The two layers of the supporting Delrin structure and its Teflon screws can be seen in the bottom picture. The two Kapton cables connected to the electrodes of the detectors are shown in the right pictures. The cathode is shown at the top and the anode at the bottom. The amount of contaminated material in the vicinity of the detectors has been reduced significantly.

Apart from the measured contaminations in the construction materials a cosmogenic activation in the raw zinc material has been measured, namely ^{65}Zn with an activity of (16 ± 3) mBq/kg in November 2004. The half life of this isotope is $T_{1/2} = 244.26$ d. The characteristic gamma line has an energy of 1115.5 keV and an emission probability of 50.6 %.
The contacts of the detector electrodes have also been removed. Instead of silver epoxy, a

home-made conductive glue of "UHU-hart" (a nitrocellulose solution adhesive), copper powder and acetone was used for the new contacts. A Kapton (polyimide) foil has been used as the basis for the cabling.
During the dismounting of the detectors two crystals were damaged. On one detector the electrode was torn off, another detector lost part of its passivation paint including small amounts of CdZnTe. After remounting, the detector with the best energy resolution was still operational. A second detector works as well, but has an increased leakage current.

2.7 The 64-Array - the next Step

At the time of writing the new design of the 64 detector array is under development. However, only few things have been decided on yet.
As stated above, the $4 \times 4 \times 4$ array will be based on the same layout used for the 2×2 array with 16 detectors per layer. The layers will be stacked in a copper casing, into which they can be easily slid in. As the Delrin holders have shown good results concerning their modularity as well as their cleanliness they have been chosen as a supporting structure for the layers. The calibration measurements will be done by feeding point like sources on a string through guiding Teflon tubes. An optimal layout of the Teflon tubes through the setup is being discussed.
Other active work is done on the preamplifiers. The discrete design of the subtraction circuit is still space consuming, but optimisations are currently investigated. The readout system with the VME ADCs as described in section 3.3 has been shown to be working and is in the production phase of the 16 modules with 4 channels each.
The shielding of the setup needs not to be changed, as the new $4 \times 4 \times 4$ array will fit into the existing copper and lead shield. Only the two centre bricks have to be replaced by the $10 \times 10 \times 20\,\mathrm{cm}^3$ supporting structure.
The limiting factor of the measurements will be the passivation paint as it is closest to the detectors and has the highest activity. However, no alternative is known yet to avoid the passivation paint and still prevent the degradation of the detectors. The detectors for this array are already ordered, and those for the central part of the array have already arrived.

Chapter 3

The COBRA Data Acquisition System

A data acquisition system (DAQ) is responsible for recording all the important information from an experiment. It is the interface between the analogue electronic components of this experiment, like amplifiers, and the digital data storage system. It usually contains elements like analogue-to-digital converters (ADCs) which convert a voltage or current to a digital number or time-to-digital converters (TDCs) which convert the time between start and stop signals to a number. The converted numbers are then usually read out from these devices via some kind of data bus on an event-by-event basis and saved on a storage device of a computer like a hard disk.
The DAQ for the COBRA experiment is designed to be as responsive and flexible as possible to reduce the dead time needed for the conversion of the measured quantities. The flexibility includes scalability in the number of detectors to be read out and the possibility to calculate the "quality" of data.
In principle, the detector signals must be sampled in a way that most of the secondary information, like timing of events, is reconstructible in order to to not only perform simple spectroscopy, but also to be able to consider coincidences or cascades of events.
In addition to the main detectors a veto system must be read out which marks events in the detector coinciding with e.g. cosmic radiation like atmospheric muons or hadronic showers going through the experiment. This signal must be coupled to the detector signals by either tagging these events or ignoring them completely. This need, of course, is weakened if the detector is located in a special underground facility like the LNGS where only a few muons can reach the detectors. There, the flux of muons is reduced by the covering rock of 3800 mWE to about 0.2 muons per m^2 and hour.

Implementations

Currently there are three major generations of the COBRA DAQ:

1. PC-based Multi Channel Analyser (MCA)

2. CAMAC-based, event-by-event readout ADC system

3. VME-based, event-by-event readout ADC system

The first generation DAQ was used in Dortmund and in the LNGS for first tests with a single commercial detector (CPG2). This DAQ is no longer used for data taking, due to its shortcomings, namely the limitation in the number of detectors – one per card – and the lack of the timing information provided for each event.
The second generation DAQ has been used for the 2×2 Prototype measurements in the LNGS. However, it is suboptimal in speed and the used modules have shown severe ageing problems which led to immense outages.
Therefore, the third generation DAQ has been developed, based on a VME Bus System. This development also included the design of a custom built ADC. This DAQ is currently operating in the LNGS.

3.1 PC-MCA based DAQ

For the initial tests with the CPG2 detector and the tuning of detector parameters of the 2×2 Prototype a PC-based data acquisition system consisting of a 13 bit MCA card (EG&G ORTEC) in a standard ix86 PC running Windows was used.
The CPG2 detector was operated with its integrated preamplifier, whose signal was fed into a shaping (main-) amplifier to adjust the signal shape and height to the MCA's requirements.
The muon veto which is described in detail in section 2.4.5 was connected to the coincidence input of the MCA, running in anti-coincidence mode so that events arriving at the ADC during a veto signal were discarded.
The MCA card is controlled by the commercial *Maestro* Software. As data can only be taken as histograms for a given period, data taking was subdivided into "runs". These runs have been recorded using a script for Maestro which starts the ADC for a fixed time (30 min runs in Dortmund, 2 h runs in the LNGS) accumulating events which are not rejected by the veto. After that period the ADC is stopped, so that the content of the histogram can be transferred to the buffer and written to disk. Before the ADC is activated again the histogram has to be cleared. Files are stored in the so-called "CHN" format which does not store the histogram alone, but also additional information, like the starting time, the real time and the life time, which is the real time minus the dead time, i.e. the integrated time where the ADC was busy or disabled by the veto gate. The file's name is generated by the script using a prefix and the value of a counter of the Maestro software in the range of '000' to '999'. This counter puts a limit on the total length of a measurement period of about 20 days for 30 minute runs.
The data taken in Dortmund with this setup has been used for a first analysis which has been published in [Kie03] and [Mue03].

3.2 CAMAC based DAQ

For the 2×2 Prototype with four readout channels a more flexible data acquisition system than the PC-MCA solution has been designed as part of this thesis using the CAMAC[1] bus system. This is a modular multi purpose crate system with a controller and up to 23 slave modules per crate. In this case the controller is a LeCroy 8901A module, a CAMAC to GPIB[2] interface

[1] **C**omputer **A**utomated **M**easurement **A**nd **C**ontrol, IEEE 583-1975
[2] **G**eneral **P**urpose **I**nterface **B**us, IEEE 488-1982

which is driven by a Linux PC via a National Instruments PCI[3]-GPIB card (see figure 3.1). This PC acts as a server which is controlled by a client Linux PC through a custom UDP[4] protocol to exchange commands and data.

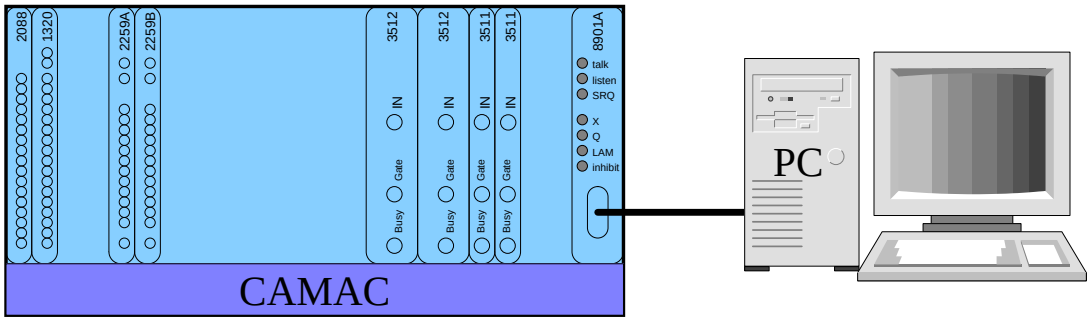

Figure 3.1: Schematic of the CAMAC DAQ-system with the CAMAC crate including its modules and the Linux PC connected via a GPIB cable.

All CAMAC operations take place over the CAMAC dataway, a parallel bus which is used to transfer all data, function codes and status information. A typical CAMAC command consists of the station number (N) which corresponds to the slot number of the module in the crate, the sub address (A) which addresses a sub section of a module (e.g. one ADC channel of a multi-channel module) and the function code (F) which is defined in the instrument's manuals. The whole sequence is abbreviated as "FAN". As a response to a FAN the module will generate a "valid command accepted" (X) response and execute the called function F. The width of the data bus is 24 bits for each read (R) and write (W) (as seen from the CAMAC controller). If the command needs to transfer data these data lines are used either by the controller setting data on the write lines before issuing the FAN or reading from the read lines, when a module issues a Q signal after a FAN, which means "data ready".
Whenever the CAMAC bus is not busy, any module may generate a Look-At-Me (LAM) signal indicating that it needs to be handled. Three common signals are issued to all stations which are used to initialise all units (Z), clear all data registers (C) and to inhibit e.g. data taking (I).
The GPIB bus protocol operates by exchanging control strings with its devices. These strings are then interpreted by the attached devices. GPIB devices can be set to "Listen" or "Talk" mode. When in Listen mode, the CAMAC-GPIB interface accepts a string which is either a setup byte or a sequence of bytes representing the FAN and 24 bit (=3 bytes) of data. This data is written to internal registers. When the controller is switched to Talk mode, a CAMAC cycle is issued. Data can then be read back again from the CAMAC bus by doing a GPIB-read on the controller.
The DAQ's core is built of four 13 bit ADC CAMAC modules (types LeCroy 3511 and 3512). They accept signals up to 8V and can be operated in peak-sensing mode. The 3511 types are 1 slot wide modules whereas the 3512 types are 2 slots wide and additionally contain a 1024 word FIFO buffer which is filled by the ADC. Both types have a gate input for (anti-)coincidences, a switch to select negative ($Z = 600\,\mathrm{k}\Omega$) or positive ($Z = 1\,\mathrm{k}\Omega$) signals and potentiometers to adjust the zero level and the lower and upper thresholds. The rise time protection can be set

[3] **P**eripheral **C**omponent **I**nterconnect, IEEE 1386.1
[4] **U**ser **D**atagram **P**rotocol

from 300 ns to 20 μs by jumpers on the module. In order to enable the ADCs, an output register of type CES 1320 is used which can put a fast negative NIM level on the coincidence inputs of the ADCs.

Based on the circuit of the preamplifier of the commercial CPG2 detector, a 4-channel preamplifier was designed for the Prototype. The outputs of this preamplifier are fed into shaping main amplifiers before the signals are ready to be fed into the ADCs. The internal electric potentiometers of the are preamplifier used to optimise the circuit and can be adjusted via the output register mentioned above. The impact of the potentiometer settings on the detector resolution is illustrated in figure 3.2. Here, the 238.6 keV gamma line of the ^{228}Th decay chain has been used to determine the relative energy resolution σ/E. An optimum value for this specific detector on this preamplifier channel is about 115 in the parabolic minimum.

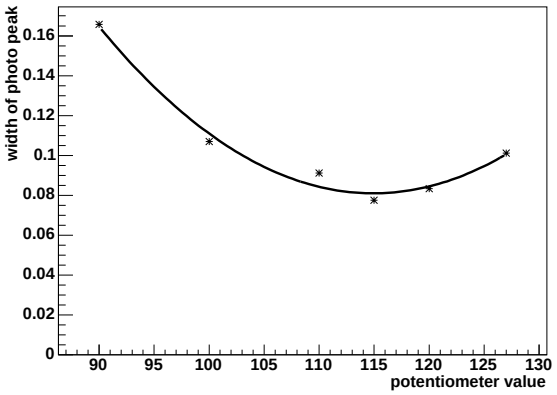

Figure 3.2: Dependence of the energy resolution from the settings of the preamplifier's potentiometers. The energy resolution has been determined with a ^{228}Th calibration source measuring the width of the 238.6 keV gamma line as the relative width σ/E of a fitted Gaussian distribution. The distribution can be described by a parabolic behaviour.

Two 12-channel 8 bit ADCs (LeCroy 2259A/B) are used for the veto-system and slow control. They accept voltages between 0 and 2 V and must be triggered externally. This is done using an output register of type SEN 2088 which can generate fast negative NIM pulses.

The coincidence between the 20 μs veto signal and the busy out of the ADCs triggers a timing unit which prolongs the veto flag, so that it can be read out with the veto-ADC mentioned above.

The number of coincidences of the veto signal and a detector signal is counted with a 4-fold 16 bit scaler of type Borer 1003. The first and last two channels can be combined via a switch to form one 32 bit counter each.

One part of the slow control for monitoring the temperature are PT100[5] elements which change their resistance with temperature. In a custom built NIM module their resistance is converted to a voltage which can be read out by the slow-control ADC. As an example, figure 3.3 shows the measured temperature in the COBRA container in the LNGS for 19 days.

[5] Platinum (Pt) based resistance temperature detectors with 100 Ω at 0°C, IEC 751, DIN 43 762

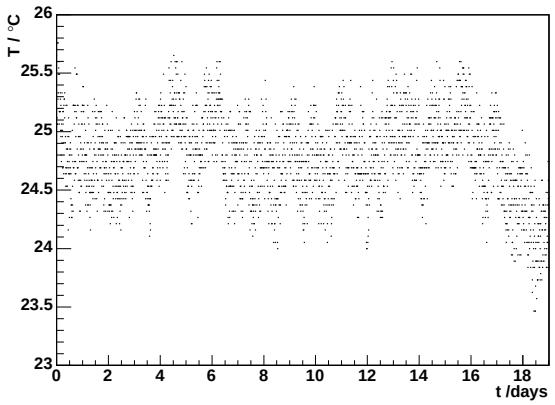

Figure 3.3: The temperature in the COBRA container in the LNGS measured with the CAMAC slow control is shown as a function of time. The fluctuation of the temperature is about 1 °C during a day. A slight day/night oscillation is also visible from the periodic spikes. The temperature at the end of the period is dropping because a NIM crate has been switched off.

The bias voltage of the detectors can be adjusted via stepping motors which are connected to the potentiometers of the high voltage supplies of type Oltronix A3.4K−40R. The motors are controlled by two controller cards connected to the parallel ports of the PC. As this system has no feedback, the settings can be monitored by a web cam pointing at the display of the high voltage supplies. A serial port relay card is used for switching devices on and off.
The DAQ software busy polls the CAMAC ADCs in a loop checking the LAM of each module. The module will be read out once if the LAM is set. So a cycle to read out all four detectors in a row takes about 5 ms where the main bottleneck is the slow GPIB bus. Slow control data is read out every 10 minutes and written to a separate slow control file together with the logging of (de-)activating detectors and starting or stopping runs.
Runs are stored in files comprising 1 hour of measurement stopping on the hour, so that the first and last file of a measuring period may be shorter than 1 h. The data is stored in a fully human readable ASCII file as shown in appendix D using a file name of daq_<year>_<month>_<day>_<hour>_<minute>_<second>.dat reflecting the starting time of the file. Each file starts with a header "START<filename>/<starttime>" where starttime is the time in seconds since January 1, 1970, 00:00:00 UTC also known as Unix time. Finally, the file is closed with "END<runtime>" where runtime is the length of the run in seconds.
Events are stored as "<detector>:<time>:<energy>:<flags>", where detector is the detector ID (1-4), time is in Unix time, energy is the ADC value and flag one of -1 (veto not enabled), 0 (event not coincident with a veto) or 1 (event coincident with a veto).
An oscilloscope of type Tektronix TDS 520 is attached to the GPIB bus as well monitoring the preamplifier signals of two detector channels. This construct is used as a first test for pulse shape measurements.
With its 8 bit resolution and a sampling frequency of 50 MHz (20 ns) the oscilloscope triggers on one channel using a rather high threshold as the oscilloscope reacts slowly to commands sent via the GPIB bus. Therefore, the threshold has been set to about 1 MeV in order to see only all events interesting for the ^{116}Cd $0\nu\beta\beta$ decay region.
If the CAMAC ADC of the detector which is monitored via the oscilloscope shows a value above 800 keV the trigger of the oscilloscope will be checked. If the trigger is set the stored

waveform can be read out. The signal of the second attached detector can then be checked for a coincident signal.
In figure 3.4 four sample events are shown. The oscilloscope was configured to trigger on the first detector whose signal is shown as a black line and also sample a second signal indicated by a red line. The first event shows an ordinary event with no energy deposition in the second detector. The second event shows a multi site or pile up event which can be identified by the additional step in the signal. Here, also the second channel is silent. The third event shows a small dip in the second detector during the signal of the first detector. However, the first detector shows an unusual shape. The fourth event also shows an abnormal shape. In this case the signal is falling too slow.

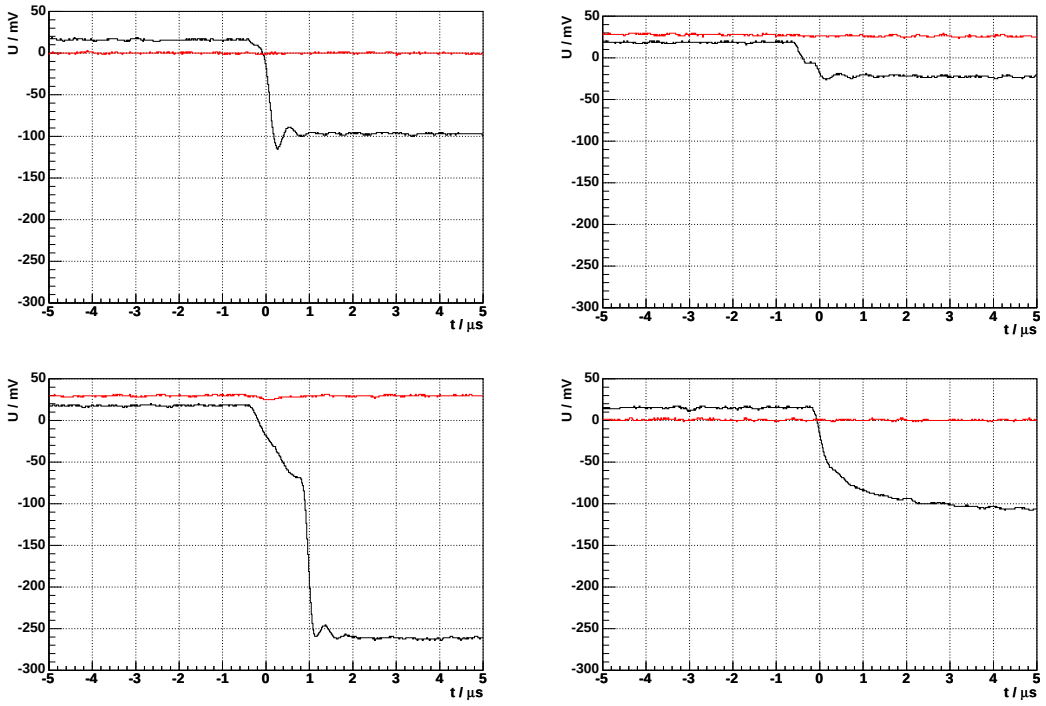

Figure 3.4: Events captured with the oscilloscope, triggered on first detector (black), also sampling a second detector (red). Top left: good event; top right: two site or pile up event; bottom left: event with kink in first detector and a small dip in second detector at $t = 0$; bottom right: event with too slow slope.

The DAQ server is controlled by a remote client via a custom UDP protocol to send command strings. The command is decoded and executed. Upon completion of the command a return message is sent back to the client transmitting the requested information or indicating the status of the DAQ. For a complete list of commands see table D.1 in appendix D.1.1.
As the driver of the GPIB card does not support interrupts at the time of writing the software, the CAMAC crate was busy polled. The full sequence of actions, as sketched in the flow chart of figure D.1, is as follows:
First the hardware components have to be initialised, i.e. the GPIB bus, the CAMAC bus and its modules and the oscilloscope. Then internal data structures, e.g. histograms, are initialised

and the server socket is opened for listening.

Then the program enters an endless loop where it first checks if a network command has been received, which is then decoded and handled. In the next step, the current system time is retrieved to check if the time interval between two slow control readouts is reached. This time is also used to check if a new hourly file must be opened if the system is currently writing events to disk.

To release the processor from unnecessary load it checks to see whether any detector is set to active. Otherwise the program is sent to sleep for 100 μs and the loop starts again. If there are any detectors activated then one ADC module in the CAMAC crate is checked for a LAM. If no LAM is active, the loop again starts from the beginning. To ensure that all detectors are read out evenly, the software checks all detectors in a loop. When data is ready to be read, if it is connected the veto ADC is also is read out. This data of the event is then written to disk in the format as shown in appendix D.3.1.

If the oscilloscope is connected to the system, the program checks if the event just read from the CAMAC ADC was in the detector which is connected to the triggering channel on the oscilloscope and checks if the oscilloscope also has triggered. If data is available from the oscilloscope the stored waveform is read out of the oscilloscope and written to disk. As the oscilloscope responds slowly (a readout of the waveforms of two channels with 500 samples takes about a second), the pulse height of the CAMAC ADC is compared to a preset value. Only if the pulse height exceeds this value, a check for a waveform on the oscilloscope is issued. To ensure that each trigger on the oscilloscope is read out immediately, the minimal value of the ADC and the oscilloscope's threshold are adjusted accordingly.

Finally, the value of the CAMAC ADC is put into a histogram and the LAM of the module is cleared. Then the program starts again with the loop.

For easier controlling of the setup a graphical user interface (GUI) called "daq-gui" has been written as the standard client using the portable "GTK+" toolkit[6]. The GUI as shown in figure 3.5 is split into four "tabs". The first gives a general overview of the status of the setup (it shows the last status via "Get Slow" command, or issues a complete readout of the slow control with the "Update Slow" command).

On the second tab ADCs can be switched on and off, data-taking can be started and stopped ("Start/Stop DAQ" command). The buttons "Start/Stop Calib" issue data taking into a single file cal_<year>_<month>_<day>_<hour>_<minute>_<second>.dat, however, for ordinary calibrations it is sufficient to use the histogramming feature of the DAQ server which can be accessed on tab three. Here, the current histograms of the DAQ server can be read out, viewed and cleared. If a "Get" command is issued, the DAQ server transmits its internal histogram contents to the daq-gui which creates a file "./detector_<ID>.dat" with the raw spectrum in ASCII format, i.e. 8192 lines with the number of events per bin in each line. The "Clear" button sends a command to clear the corresponding histogram on the server. "Clear all" resets all histograms on the server. The histogram viewer can switch from logarithmic to linear y-axis and either shows the jolted complete spectrum (8192 channels in an 800 pixel wide window), or zooms in to map one channel to one pixel.

[6] http://www.gtk.org/

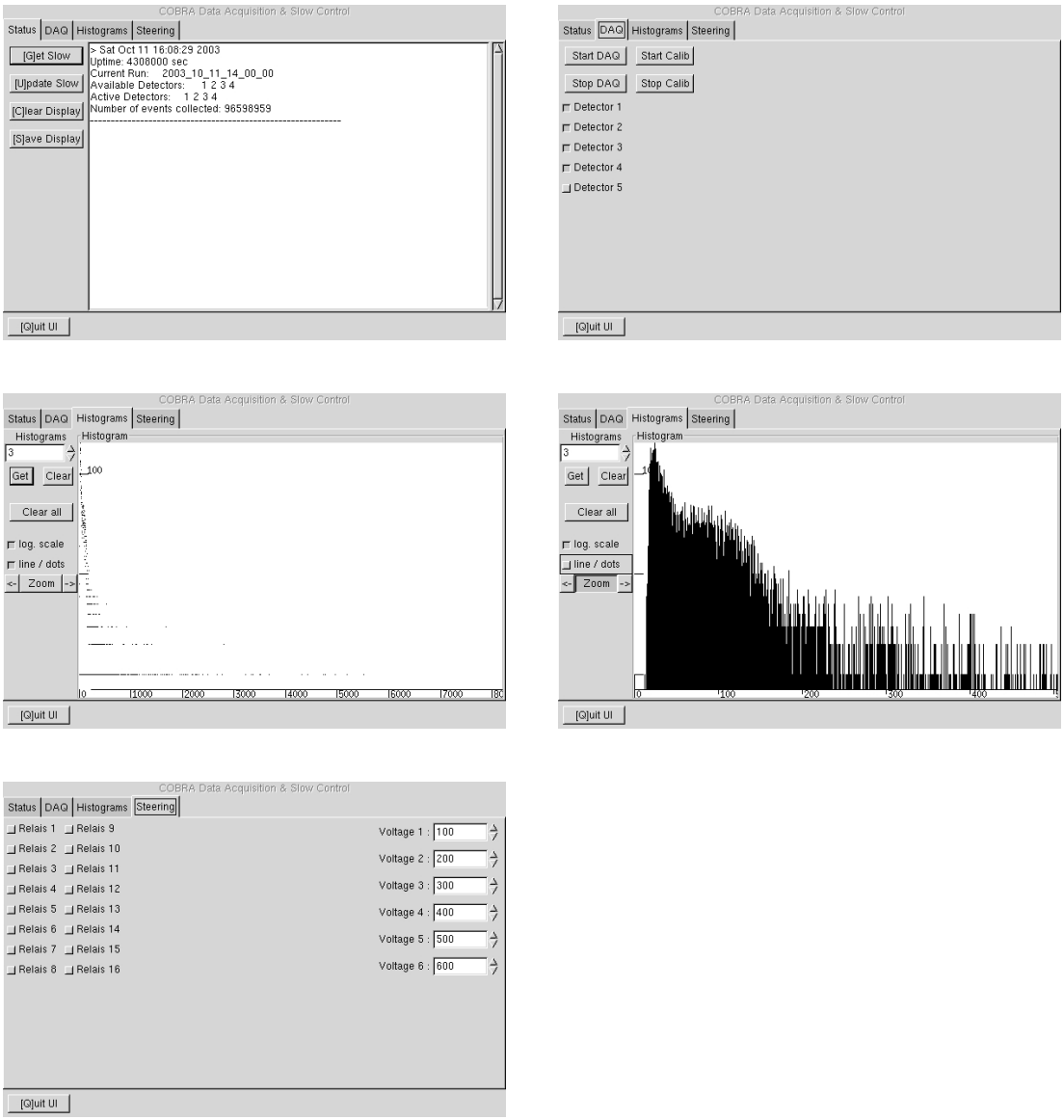

Figure 3.5: The tabs of the DAQ-GUI are shown. The general overview in the top left picture shows the currently open data file and active detectors. The detector status in the top right picture is used to switch on and off detectors and start or stop data taking. The middle row shows the histogramming tab with the current spectra of the data taking. The left picture shows the full spectrum up to channel 8192 as dots and the right picture shows the zoomed spectrum up to channel 500 displayed as lines. The slow control tab with the relays and the high voltage control is shown in the bottom line.

The fourth tab is used for slow control. 16 sockets can be switched on and off via the above mentioned relay card and step motors can be driven to set the high voltage supply to the new position. As a surveillance system, a web cam is connected to one step motor and can be turned around to look at the displays of the high voltage supplies. A lamp is connected to one of the

relay-sockets and can be switched on and off to supply light for the camera.
The muon veto mentioned section 3.1 has been operated in Dortmund but was never activated in the LNGS due to the lower muon flux. However, the system is prepared to accept its signals and couple them to the data taking.
Despite the feature rich implementation of this rather complex DAQ system, the deployed CAMAC hardware is based on more than 20 year-old modules which were available at the University of Dortmund but they caused lots of trouble and outages during data taking. Due to the aged electronics components the following bugs have been discovered:

- bit error,
- sub threshold events,
- drift,
- creating fake events in other ADCs,
- and complete breakdown blocking the bus.

Also the shaping amplifiers did not transform the signal from the preamplifiers perfectly to Gaussian pulses so that due to the rather long input signals, a tail remains in the shaped signal. For high energetic events this tail is still above the threshold of the ADCs leading to subsequent unwanted conversions.
This effect is only grave for the ADCs of model LeCroy 3512, because of their internal buffer. For the other modules the readout is too slow to effectively sample the tail. These excess events are filtered out by software in the analysis, however, this may lead to ambiguities when considering cascaded events.
Another problem with this CAMAC system is that it is not possible to expand the number of readout channels to the required 64 channels for the $4\times4\times4$ array. As a conclusion a completely new DAQ system has been designed re-using already existing supplementary devices (e.g. the relay box, etc.).
Publications of improved limits on double beta decays relative to the ones obtained with the PC-MCA system and a measurement of the beta decay of ^{113}Cd are in preparation [Göß05, Kie05].

3.3 VME based DAQ

In order to simplify the hardware structure a new bus system has been chosen for the next generation data acquisition system. The VME[7] bus appeared to be a good choice due to its robust modular design and high bandwidth. Many vendors produce VME modules for nearly any purpose which guarantees support for a long time. Another advantage is that there exist state of the art computer boards, so-called Single Board Computers (SBC), which are directly plugged into the crate and control all modules in the crate. This way the modules can be accessed directly without the need of additional buses like for the CAMAC system. Furthermore, a VME module is accessed via its settable base address and not via the slot number in the crate.
VME is a 32-bit computer architecture which was introduced in 1981 [Pet93] with processor independence and open architecture without proprietary rights in mind. Information about the

[7] **V**ersa **M**odule **E**urocard, IEEE 1014-1987

VME bus is available from the VITA[8] which is a non-profit organisation of vendors and users of VME products.
As a computer architecture, the VME bus has a memory mapped scheme, which means that every device on the bus can be accessed by an address or a block of addresses. The backplane of the VME bus operates with TTL[9] signals. Although it is asynchronous, the bus has a maximal transfer speed of approximately 20 Mbyte per second. Later improvements of the VME bus also feature higher transfer rates. A VME crate usually contains 21 slots for modules, although smaller crates are sometimes used in development environments.
The VME bus can be subdivided into five sub-buses:

- *Data Transfer Bus*
  This is the part most used. It consists of 31 address lines A01-A31, where the least significant (LSB) bit of an address (A00) must always be 0 and is therefore not wired, an address strobe (AS) line to indicate valid data on the address lines, six address modifier lines AM0-AM5 which specify the width of the broadcast as "short I/O" (16-bit), "standard" (24-bit) and "extended" (32-bit) and 32 data lines D00-D31. There are additional lines to indicate valid data on the bus (DS0, DS1), acknowledge data transfers (DTACK) used by slaves, mark the direction of the data lines (WRITE) or signal that an error occurred during the bus cycle (BERR).

  Some of these lines are also used by interrupt handlers to get status and ID from interrupters during interrupt acknowledge cycles.

  There also exists an extension of the VME bus to 64 bits. For this extension a new backplane is used in the crate, which is, however, backwards compatible to standard VME.

- *Data Transfer Arbitration Bus*
  This part is used by the masters to obtain ownership of the above data transfer bus. A module which is currently controlling the bus will drive the bus busy line (BBSY) low to indicate that it is in use. If this line is not low the most left module in the crate, the arbiter module, will sample the bus request lines (BR0-BR3) looking for a pending action, where requests on BR3 have the highest priority. Requests of equal priority are handled by a daisy chain using the bus grant in lines (BG0IN-BG3IN) and the bus grant out lines (BG0OUT-BG3OUT). The arbiter module will generate the first grant signal which is passed to modules of increasing slot number.

- *Priority Interrupt Bus*
  This part performs the system interrupts, where seven interrupt levels are possible using the seven interrupt lines (IRQ1-IRQ7) with IRQ7 as the highest priority. In response to an interrupt, an address cycle is generated where the address indicates the request being acknowledged. The interrupt acknowledge (IACK) is then changed in the arbiter to a signal which is daisy chained down the bus using the interrupt acknowledge in (IACKIN) and out (IACKOUT) pins. In a following data cycle the module requesting the interrupt asserts its status and ID.

[8] **V**MEbus **I**nternational **T**rade **A**ssociation
[9] **T**ransistor-**T**ransistor **L**ogic

- *Utility Bus*
  On these lines miscellaneous signals are passed for initialisation via a system reset (SYSRESET), periodic timing with an independent 16 MHz clock (SYSCLK), and system or power failures (SYSFAIL, ACFAIL). Power is supplied to modules via pins at $+5$ V, -12 V and $+12$ V. An optional battery backup of the $+5$ V supply (+5STDBY) may also be present.

- *Serial Bus*
  Urgent messages between modules or systems can be passed using the VMSbus using pins for clock (SERCLK) and data (SERDAT).

Depending on the operating system and the support packages delivered with the computer boards, the VME bus is accessed slightly differently. In most cases an access to the VME bus can be initiated by reading or writing to an address in the normal address space which is mapped to an address on the VME bus.
This is the case for the Motorola MC68040 based MVME167 SBC. It has been operated using the NetBSD operating system. There was no special support package, however, in the BIOS of the SBC the VME bridge chip can be programmed to map a certain region of the processor's address range to the VME bus using fixed address modifiers. As processes in Unix use the MMU[10] to map virtual addresses to true addresses in the processor's address range, this method needs a special kernel option. The whole processor's address space can then be accessed via the special device "/dev/mem". To make a VME bus access look like an access to ordinary RAM, the `mmap()` function can be used. Reading data from or writing data to the VME bus is then just a matter of reading or writing to the address of the slave module.
The drawback of this non-commercial system is the use of interrupts. In order to catch interrupts from the VME bus a kernel module would have been needed to write. As COBRA aims for a low rate experiment, first tests have been successfully done with this system not using interrupts.
At the end of 2004 a new, more powerful PowerPC based SBC, the TEWS TVME8240, has been installed running Linux. This board was purchased with a complete set of drivers for the VME bus including IRQ support. The board also supports mezzanine IP[11] modules which are mainly used for slow control.
There is one IP module with a 16 channel, 12 bit ADC and a 4 channel, 12 bit DAC[12]. Some channels of this ADC are used for temperature measurements with the PT100 elements mentioned in section 3.2. A 48 channel TTL I/O module is used to set up the preamplifier settings. The inputs and outputs of the IP modules are realised as 50 pin post plugs. These post plugs are connected via ribbon cables to a custom built NIM transition box shown in figure D.4. The TTL lines are put to DB9 connectors with a COBRA standard assignment, providing 5 TTL lines on the upper five pins and ± 12 V and ground on the lower pins.
A CAN bus[13] controller (CAN-HIGH-SPEED) is used to control and monitor the status of the VME crate.
The success of the COBRA experiment depends strongly on background suppression. Therefore, the analysis of cascaded background events in the 100 μs lifetime regime is of impor-

[10] **M**emory **M**anagement **U**nit
[11] **I**ndustry **P**ack, ANSI/VITA-4 1995
[12] **D**igital to **A**nalog **C**onverter
[13] **C**ontroller **A**rea **N**etwork, ISO 11898

tance. In order to optimise the performance of the setup, a custom analogue to digital converter (ADC) module has been designed and built in cooperation with the Elektronik-Entwicklung of the Fachbereich Physik of the University of Dortmund.

This step has been taken because no suitable commercial module exists which fulfils the needed requirements. These key features have been set from the experience with the CAMAC system:

- $\geq$13 bit resolution
- multi channel ($\geq$8)
- simultaneous conversion of all channels
- peak detect
- self triggering
- event buffer
- time stamps for events ($\leq 10\mu$s resolution)
- boolean logic input (e.g. for veto).

For the 2×2 Prototype detector a prototype VME board has been developed containing four peak sensing 14 bit ADC channels each with VME-settable threshold and gain. Figure D.5 shows a picture of the ADC. If the input signal in one channel exceeds the threshold, a complete readout is issued for all other active channels. This way the digitised values of all detectors are recorded including their pedestals. This trigger signal can also be connected through a front side bus to other modules to be able to extend the readout to more than four detectors. This is especially important for the $4 \times 4 \times 4$ array. The time between crossing the threshold and the start of the first conversion, called rise time protection (RTP), can be set in steps of $1\ \mu$s from 0 to 1023 μs.

The analogue part of the module shown in figure D.6 has been placed on a separate board, a so-called mezzanine, which is plugged onto the main board. The digital part and the ADC chip of type AD7865 remains on the main board. In a first version of the ADC the analogue part was directly put on the main board. Therefore, it was impossible to exchange the analogue circuitry in order to improve its speed performance or reduce the noise.

The current version of the analogue mezzanine uses the commercial “PKD01” chip as a peak holder. For a more sophisticated module, this chip may be replaced by an optimised discrete circuitry.

The ADC board has been designed to enhance its resolution by a technique called oversampling, which means that the signal is converted multiple times. The mean value of these samples is then calculated usually resulting in a better resolution. The calculation of the mean value is done by the readout software.

The oversampling technique has been introduced, motivated by experiences made with the first version, before performing some optimisations on the analogue mezzanine. It was implemented as a 7-fold oversampling, which led to a better energy resolution. However, after introducing a low-pass filter to the input amplifier, this technique no longer shows a significant improvement. The left diagram of figure 3.6 shows the distribution of the n-th sample. The right diagram shows the mean of the Gaussian distribution. The error bar indicates its width σ. The amplitude decreases from sample to sample because of a small leakage current on the peak holder's capacitor. The first sample is much higher than the others because of an overshoot in the peak holder.

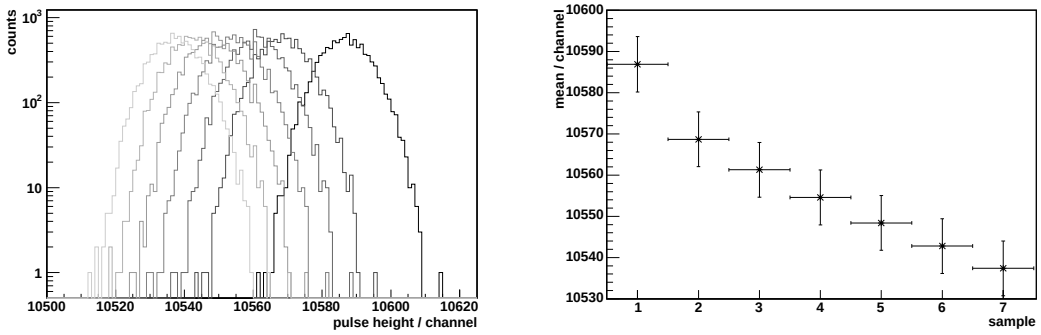

Figure 3.6: The left diagram shows the distribution of samples for the oversampling technique. Sample 1 is on the right side with the darkest colour. Due to a small leakage current of the peak holder, the amplitude shrinks over time as can be seen from the right figure, which shows the extracted mean values of the single sample distributions. The error on the ordinate reflects the width in sigma of the measured peak. The full statistics is 1000 events of constant height induced with a test-pulser. No significant degradation of the signal with time indicated by the width of the distributions can be seen.

The correlation of two measured values of the oversampling is shown in figure 3.7. It can be seen that the fluctuations are not statistical for each sample, but constant for each event. The distribution looks qualitatively the same for all combinations.

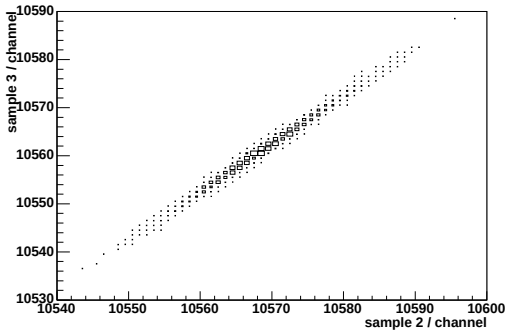

Figure 3.7: The measured values of sample 2 against sample 3 are shown. A strong correlation of the two measurements can be seen as the events are mainly clustered on the diagonal. An uncorrelated distribution would show up as an elliptical distribution.

In order to reduce noise more effectively, a low pass filter has been placed behind the peak holder. As a side effect this removes the mentioned overshoot. Figure 3.8 shows the sampled value as a function of the RTP. This way, for a periodic signal, the pulse shape can be sampled with 1 μs accuracy. Also with this technique it can be shown that the second sample of one channel comes 10 μs later than the first sample when doing oversampling.
In the final version, the oversampling technique has been removed again, because each conversion takes about 2.5 μs, which sums up to 70 μs for 7 over-samples with four ADC channels active possibly spoiling the recording of cascades.

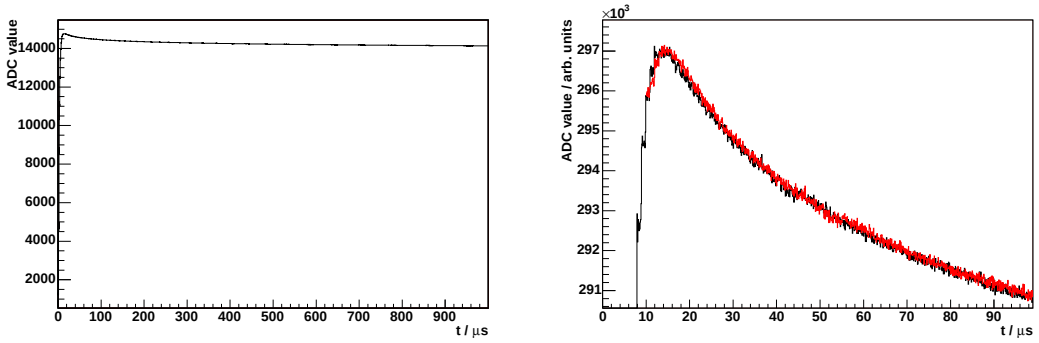

Figure 3.8: The left diagram shows the sampled value for a series of pulses of constant height as a function of the RTP, "oscillographing" the pulse form at the peak holder. The right diagram shows the same data set with sample 2 overlaid in red, shifted by 10 μs to match the first sample. This demonstrates the time difference between two over-samples of $\Delta t = 10\,\mu$s.

The values of the four ADCs are stored in a FIFO buffer together with the value of the timer at the time of conversion and 14 TTL levels.

The timer has a precision of 8 μs and can be reset via a VME command which is also broadcast to the other modules connected via the front side bus. The timer is used to generate a time stamp of an event. It is a 32-bit counter which corresponds to approximately 9.6 hours before the timer overflows to zero. The timer is driven by the 16 MHz clock on the VME backplane, so that the timers of all modules will always be synchronous.

Some of the TTL levels will be used for the 20 μs long veto signals from the scintillator paddles, others may indicate the status of other components.

The FIFO is organised in 2 chips with 4096×8 bits each, to be able to hold the 16 bit wide values. This is enough room for 512 events with $7 \times 4 \times 2$ byte ADC values + 4 byte time stamp + 2 byte TTL = 14 bytes. Two more bytes are added to round the number of bytes up to 2^4 using a duplicate of the TTL levels. This is done in order to prevent the module from adding an event only partially to the FIFO in case it is nearly full.

Another data integrity check is done using the two most significant bits of each data word. In all ADC data words these bits are set to 1. The two bits of the TTL value and its duplicate are set to 0. The value of the timer is not affected, thus the value of the two bits is undefined. If the timer is reset every hour, then the two most significant bits of the high word will also stay 0. This way the readout software can check that the data sequence read in from the ADC is synchronised. The whole sequence is shown in table 3.1.

The module can be set up to generate interrupts when the buffer is no longer empty, i.e. an event has been sampled, or when the buffer is half-full or full. This information is also available in a status register. If an interrupt occurs the data can be read out in a block reducing VME overhead. The FIFO state (empty, half-full and full) is also indicated by LEDs[14]. Other LEDs indicate a conversion of the ADC module, occurrence of an interrupt and the active channels.

[14] **L**ight **E**mitting **D**iodes

Data Word	Content	Data Width / Bit	MSB Value
1	TTL	14	00
2	TTL (duplicate)	14	00
3	Timer low	16	undefined (data)
4	Timer high	16	undefined (data)
5	ADC channel 0	14	11
6	ADC channel 1	14	11
7	ADC channel 2	14	11
8	ADC channel 3	14	11

Table 3.1: The data sequence of the VME ADC is shown with the content, data width and integrity bits for each item. The TTL value is duplicated to obtain a sequence length of 8 words to avoid corrupted events in the buffer. The integrity bits are set to 0 for the TTL item and 1 for the ADC data. These two bits are, however, used for the data of the timer and thus undefined as integrity bits.

In figure 3.9 a schematic of the components of the 2^{nd} generation ADC board is shown. The signal inputs are on the left side and the VME bus is on the right side. A negative signal with few 100 ns rise time and some 100 μs fall time is fed from the shaper via a LEMO connector to a peak holder. The output of the peak holder is used as input for the ADC chip and the threshold. Both threshold and a small amplification factor from 1 to 10 in steps of approximately 0.1 can be set via a VME command.

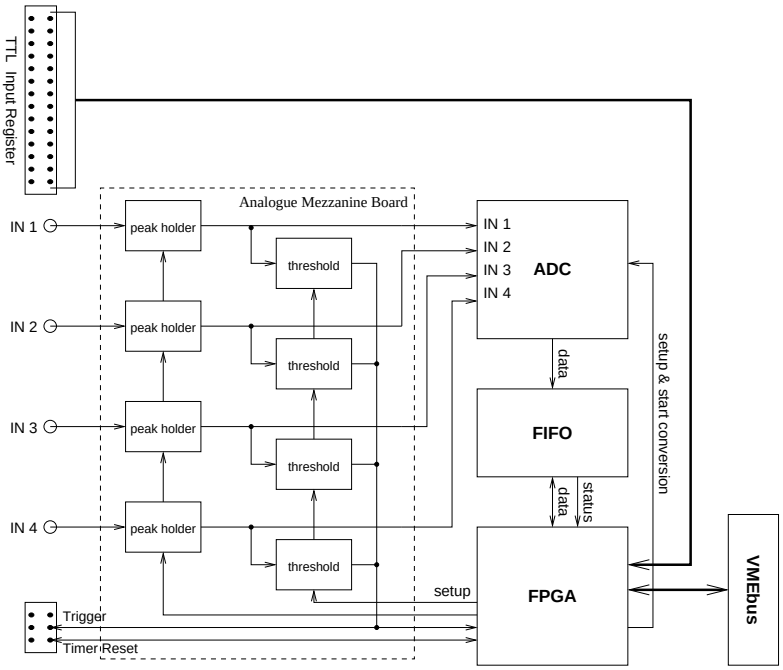

Figure 3.9: Block diagram of the functional components of the VME ADC board. The four input signals pass through peak holders to the threshold and the ADC chip. An FPGA[16] coordinates the readout of the signals and the communication with the FIFO and VME bus.

[14] **F**ield **P**programmable **G**ate **A**rray

The stability of the device has been investigated. A temperature dependence is clearly visible by feeding the ADC with several pulses of a constant height and measuring the temperature of the board with the PT100 elements mentioned above connected to the analogue I/O IP board. The distribution of pulse heights as seen from the ADC against the current temperature of the board is shown in figure 3.10. For each temperature the mean of the ADC value can be plotted against the temperature. The resulting graph can be approximated by a linear correlation. The slope of this fit gives a temperature change of $(9.42 \pm 0.35) \cdot 10^{-4}/°\text{C}$. Compared to a value of $1 \cdot 10^{-4}/°\text{C}$ for the CAMAC ADC [LeC80], both modules are of almost equal stability.

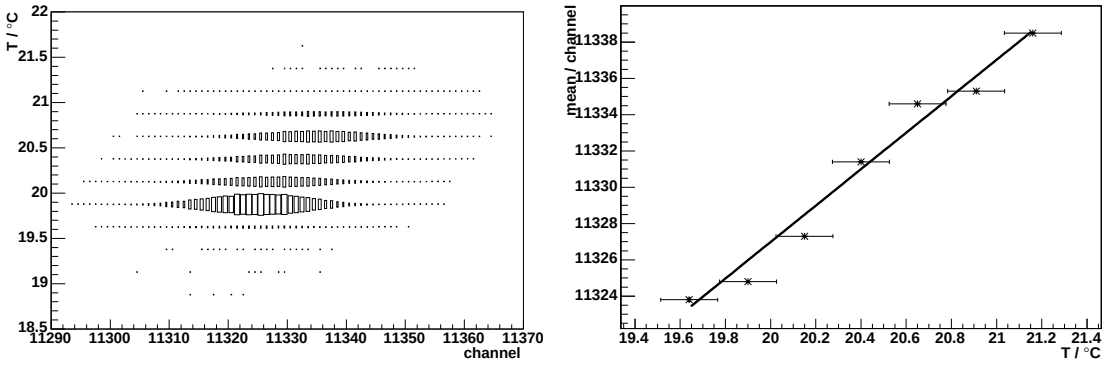

Figure 3.10: Temperature dependence of the VME ADC. Pulses with a fixed height have been fed into the ADC while slowly changing the temperature of the whole system.

The width of the distribution at a constant temperature is a measure for the goodness of a converted value. In figure 3.11 the distribution for $T = 19.9°\text{C}$ is shown. The resolution is $\sigma = 7 \cdot 10^{-4}$ which is well below the energy resolution of the CdZnTe detectors of above 1%.

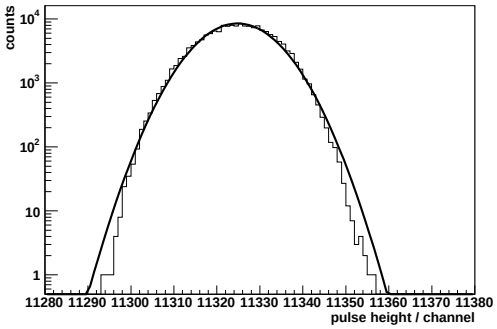

Figure 3.11: Resolution of the VME ADC at 19.9°C. The distribution of measured pulse heights is well fitted by a Gaussian of 7.9 channels width or $\sigma = 7 \cdot 10^{-4}$.

To reduce the costs per readout channel the signals from the preamplifiers are not fed into main amplifiers, but are transformed with a comparatively cheap shaper circuit instead. The shaping is necessary to reduce pile-up of events because of the slow decrease of the signals from the preamplifier and to suppress noise.
The TTL lines 1-3 from the COBRA-DB9 connector are used to set the electronic potentiometers in the preamplifiers and the shaper via a simple daisy chained protocol. If the chip select

(CS, pin 1) line is low, data provided on pin 2 is written to the daisy chain during a clock signal on pin 3. This way 7 bit of data per electronic potentiometer are written. If the CS signal switches to high again, the value in the register of the potentiometers is applied.

The client-server model to control the DAQ has proven its usefulness with the CAMAC setup, also because it reduces the CPU power needed for the server. This makes it possible to use the existing MC68040 based MVME-167 modules as VME controller for further testing of modules in Dortmund, whereas the faster PowerPC based TVME8240 is used for the real operation in the LNGS.

A minor change of the underlying transport protocol has been performed, changing from UDP to the more reliable TCP[17]. The new command set remains almost compatible to the CAMAC commands but is still updated and adjusted to the new hardware. The complete list of commands is given in appendix D.1.1.

Since the transport protocol and part of the command set changed, the CAMAC daq-gui has also been reworked completely. A new graphical front end for calibrations has been built using the ROOT toolkit[18]. A snapshot of the new program is shown in figure 3.12.

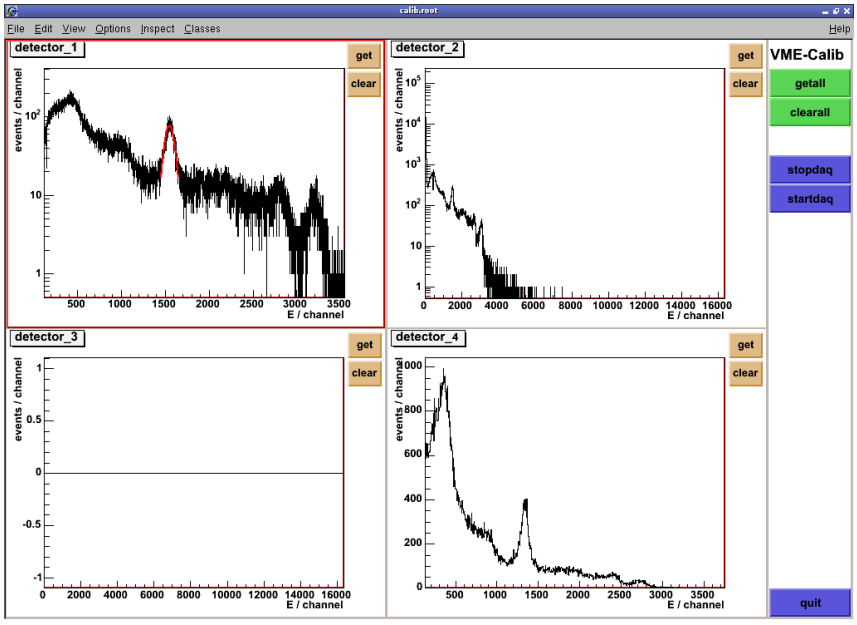

Figure 3.12: The calibration front end for the VME DAQ using the ROOT toolkit is shown. The four histograms correspond to the four detectors in the 2×2 array showing the possibilities of the new user interface. The spectra show a combined calibration with a ^{137}Cs and a ^{60}Co source. Detector D3 has been switched off, because of its damaged electrode. The top two spectra show the spectrum logarithmically. Detector D1 shows a zoomed view with a fitted Gaussian to the 661.66 keV photo peak of ^{137}Cs indicated by the red line. Detector D2 shows the full spectrum, and detector D4 shows the zoomed spectrum linearly. The current spectra can be fetched from the DAQ server by pushing the get button. They can also be cleared on the DAQ server. Data taking can be started and stopped from this user interface as well.

[17] **T**ransmission **C**ontrol **P**rotocol

[18] http://root.cern.ch/

As this new DAQ system samples the current value of all detectors simultaneously if one channel exceeds the threshold, a new output format has been used compared to the CAMAC system with single ADC readout.
The data format resembles the format for the CAMAC DAQ with the same header and footer line. A sample is shown in appendix D.3.2 to be compared to appendix D.3.1. Data is read out on an ADC module basis so that the data points include the module number, the ADC channel with highest content, the on-board timer (in 8 μs steps), the system time of the readout, the values of channel 0-3, the TTL register and finally, temperatures read out by the IP modules. The temperature value is again the ADC value of the resistance to voltage conversion. All these items are separated by a white space character. The starting time given in the header can be taken as a unique run number. The data will be stored in a ROOT file in the near future.
This new system overcomes the deficiencies of the old CAMAC system, such as the rather slow response time spoiling the analysis of cascaded events in the μs regime or the reliability of the hardware components due to their age. Also the tailoring of the ADC to the experiment's needs concerning pulse form and height reduces the need for shaping amplifiers and thus reducing the complexity of the whole system.

3.4 Outlook

Apart from further active background reduction by using less active materials and building a better shield, for future upgrades of the detector array the following points should be considered:

- **Upgrade of the array to several hundreds of detectors**
  Simulations show that for one event in a large array only a few detectors show an energy deposition. Multiplexing could then be a possible solution to reduce the number of ADC channels.

- **Pulse shape analysis using Flash ADCs**
  In order to discriminate signal from background events and to improve the detector resolution a pulse shape analysis using Flash ADCs sampling the pulse form of the signal could be used.

- **Using pixelated detectors**
  Background reduction can be further improved by segmenting the detectors and measuring tracks of electrons in the crystal.

- **Miniaturisation by using ASICs**[19]
  The above pixelation of course increases the number of readout channels by several orders of magnitude, so that the density of readout channels has to be increased. ASICs are a good choice for this purpose.

[19] **A**pplication-**S**pecific **I**ntegrated **C**ircuit

Chapter 4

Monte Carlo Simulations

Monte Carlo simulations are a widely used tool to help in designing a new apparatus or to understand an existing one. For the COBRA experiment simulations have been done as well with respect to the optimisation of the geometry for the new 64 detector array as well as the design of the neutron shield and the comprehension of background sources in the old 2×2 array. Different simulation packages have been surveyed to find an appropriate tool to be used as the standard simulation program for the COBRA experiment. These different packages are also used to cross check the results of each other. The standard simulation program has been developed within this thesis.

4.1 MCNP

As a first step MCNP[1] version 4C [Bri00] has been used. The program code has been obtained from the NEA[2] which is the official distributor for MCNP, cross section tables and other programs and data tables to be used in nuclear safety.
MCNP is a powerful Monte Carlo simulation tool mainly used by e.g. radiologists and in nuclear safety. Thus, its advantage lies in easy handling, allowing easy source and detector definitions through a sophisticated dynamic geometry description. The scope of the simulations lies within calculating neutron, photon and electron interactions as well as nuclear fission. Despite its simplicity the program has its drawbacks such that an event-by-event handling is rather difficult and multi-particle sources which are essential to simulate double beta decays as well as cascades of radioactive background are not feasible without major modification of the code. Another deficiency is its low calculation speed.
Nevertheless, for first simulation tests the code has been modified to simulate double beta events. This was done by tricking the event generation which is only capable of handling one source particle into immediately decaying a "virtual double beta" particle. This virtual particle has an energy corresponding to the sum of energies of the two primary electrons to be generated. During its decay the directions and energies of the decay products are calculated according to [Tre95].

[1] **MCNP** - A General **M**onte **C**arlo **N**-**P**article Transport Code

[2] **N**uclear **E**nergy **A**gency, a specialised agency within the Organisation for Economic Co-operation and Development (OECD), an intergovernmental organisation of industrialised countries, based in Paris, France.

Another approach was done by using the high energy simulator GEANT 4 which is described in the following section. It was designed to handle the simulation on an event-by-event basis with user defined readout functions. Nevertheless, MCNP is used as a cross check for GEANT 4 and has been intensively used to optimise the neutron shield of the COBRA setup [Oeh04]. Figure 4.1 shows an MCNP display of the setup for the neutron shield simulation.

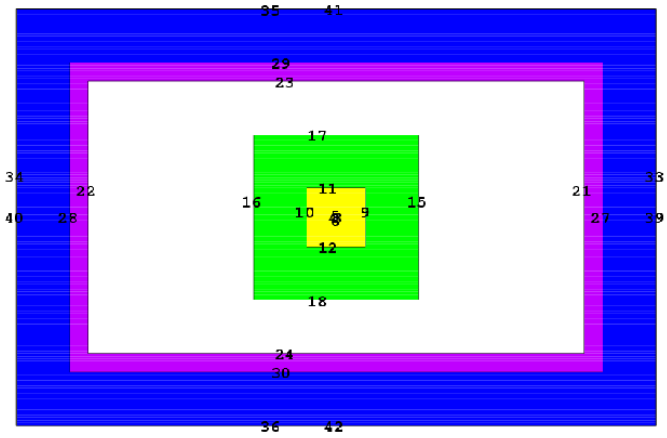

Figure 4.1: Setup of the neutron shield as displayed with MCNP [Oeh04]. The neutron shield is motivated by a significant neutron flux in the LNGS which generate background events by ^{113}Cd(n,γ) reactions in the detector material with a cross section of 20 kbarn as described in section 2.4.4. The moderator material paraffin is indicated by blue, the neutron capturing boron loaded polyethylene by purple colour. The gamma shield of lead and copper is marked by green and yellow colour respectively. The numbers indicate the index of the surfaces delimiting the volumes.

The neutron shield consists of a layer of 20 cm thick paraffin wax bricks which moderate the neutrons from the surrounding rock followed by another layer of borated polyethylene plates. In this layer mostly thermal neutrons are captured by the isotope ^{10}B with a cross section of 3850 barn [SE98]

$$^{10}\mathrm{B} + \mathrm{n} \rightarrow {}^{7}\mathrm{Li} + \alpha. \tag{4.1.1}$$

Also neutron capture on the hydrogen in the paraffin and polyethylene takes place, however with a smaller cross section of 0.332 barn [Shi02]. The cross section for elastic scattering is 20.47 barn.

Further candidates for thermal neutron capture are ^{6}Li with a cross section of 940 barn and ^{113}Cd with a cross section of $20.6 \cdot 10^3$ barn [SE98]. However, ^{113}Cd is not a good candidate as the (n, γ) reaction produces gammas up to 9 MeV which may create further background in the detectors.

The simulated absorption efficiency of neutrons by the current COBRA neutron shield is shown in figure 4.2 using the flux in the Gran Sasso [Bel89]. The simulation shows that the neutron flux is reduced to at least a factor of 10^{-6} for all energies [Oeh04].

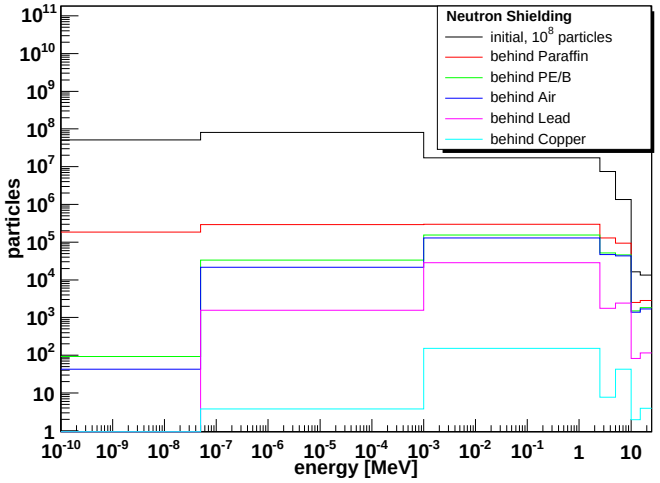

Figure 4.2: Simulation of the COBRA neutron shield [Oeh04] using MCNP. The diagram shows the reduction of the neutron flux by the different layers of the neutron shield. The input spectrum of the neutrons is taken from [Bel89].

4.2 GEANT4

Like MCNP, GEANT4 [Ago03] also simulates the passage of particles through matter. It is designed as an object orientated toolkit based on C++[3]. Its application areas include high energy physics and nuclear experiments as well as medical, accelerator and space physics studies. The functionality provided by this package embraces geometry, tracking, detector response, run, event and track management, visualisation and user interface.

From the physics side GEANT4 includes a diversity of interactions of particles with matter across a wide energy range. All known mesons, baryons and leptons are included as well, as its main focus lies on high energy physics simulations. However, special low energy routines are also provided through the LowE package [Ama04].

GEANT4 is the successor of GEANT3 [Bru87] which is based on the FORTRAN[4] programming language. The main focus during the move from FORTRAN to C++ was on advanced software engineering techniques and object orientated technology to have a transparent physics implementation which allow the validation of the physics results more easily. All classes have been designed in a clear hierarchical structure. The development of this package is done in close contact with the users in order to meet their requirements.

GEANT4 started as an R&D project at CERN[5] (RD44) and is now an international collaboration. The source code is freely available and being further developed with regular releases. An extensive documentation is available through the Internet.

GEANT4 does not use geometry files for the detector setup, but instead the setup must be programmed. Therefore, for an easier handling, a standard simulation package has been developed for the COBRA experiment which is called “POISON”.

[3] ISO/IEC 14882

[4] **FOR**mula **TRAN**slator, ISO/IEC 1539

[5] **C**entre **E**uropéen de **R**echerches **N**ucléaires, European Organisation for Nuclear Research, Geneva, Switzerland. http://www.cern.ch/

4.3 POISON

POISON is the standard Monte Carlo program for the COBRA project. It uses the GEANT4 toolkit to simulate events in a user defined detector setup. The scope of POISON is to have a versatile simulation program to compare different possible detector setups and radiation sources in order to understand the intrinsic background of the materials in the vicinity of the detector and to simulate signal events. The outcome of the simulations can be used to optimise the current prototype setup or a future setup.
In order to accomplish this, no fixed activities of radio impurities are integrated into the simulation. Instead, the user can choose from a great variety of radiation sources which may be distributed in certain parts of the setup.
Basically, first a detector geometry is defined and then events are simulated specifying only their type (e.g. double beta decays as a signal or gamma radiation as a background) and location (e.g. homogeneously distributed in the detector material or in the surrounding copper shielding).
The simulation does not contain a time-line so that activities can only be considered by simulating a number of events which are supposed to happen in a certain time. This also prevents from simulating pile up events.
The energy deposited in each detector by the simulated source particles and their secondaries is given as output on an event-by-event basis. However, no detector effects like charge collection or energy resolution are simulated yet so that this simulation is a mere calculation of the geometrical acceptance of the setup. Measurements with the transient current technique (TCT) [Kra04] mentioned in section 2.1 may give valuable input to a simulation of the charge transport in the crystals.
For comparison with measured data, the energy resolution of the detectors can be folded externally after the simulation using empiric rules. As a side effect, this also allows the analysis of the impact of different energy resolutions with one set of simulated data.
For now only a simplified 3-dimensional array is integrated in the main version of POISON. The full description of the program and its commands can be found in [Kie04]. A detailed modelling of the 2×2 Prototype has been developed [McK05] and will be integrated into the main version. A short description of the geometry's details will be described in section 4.3.2.

4.3.1 The 3-Dimensional Array Geometry

Before a simulation can be started two input files have to be prepared: a file describing the geometry of the setup and another containing a sequence of commands which describe the events to be generated. The commands can also be passed interactively to POISON instead of using the latter file. The two input files are documented in the following paragraphs.
For the 3-dimensional array implemented in the main version of POISON the following parameters can be changed. A graphical illustration of the parameters is shown in figure 4.3.

- The **material** of the detectors.
  This can be either 'CdZnTe' (= 'CZT') or 'CdTe'.
- The size of the detector crystals: **cdte_dimx**, **cdte_dimy** and **cdte_dimz**.
- The number of detectors in each direction **DNX**, **DNY** and **DNZ**.
  The number of placeholders in x and y direction: **DGX** and **DGY**.

If DGX<DNX or DGY<DNY was specified the number of placeholders is automatically set to the number of detectors.

- The distance of the detectors in x and y direction **gap_len**.
  This is half the distance between two detectors and the full distance to a possible surrounding shielding.

- The detectors are “mounted” on trays of copper whose thickness can be set via **tray_width**.

- The gap between the detectors and the copper tray on which they are mounted is defined by **gap_bot**. For a non vanishing value the detectors are hovering above the tray.

- The gap above the detectors to the next tray or the shielding is specified by **gap_top**.

- The thickness of passivation paint **paint_th**.
  This is simulated on 5 sides of each detector (all sides except the bottom, where the unpainted planar electrode resides) as a generic polymer material.

- Around the detectors a shielding can be defined from inside outwards with first copper (**copper_wallx**, **copper_wally**, **copper_wallz**) and then lead (**lead_wallx**, **lead_wally**, **lead_wallz**). Setting these values to 0 removes the shielding completely.

After reading in the geometry file the program performs certain consistency checks on the specified parameters. The revised geometry data is written to stdout when POISON is started.

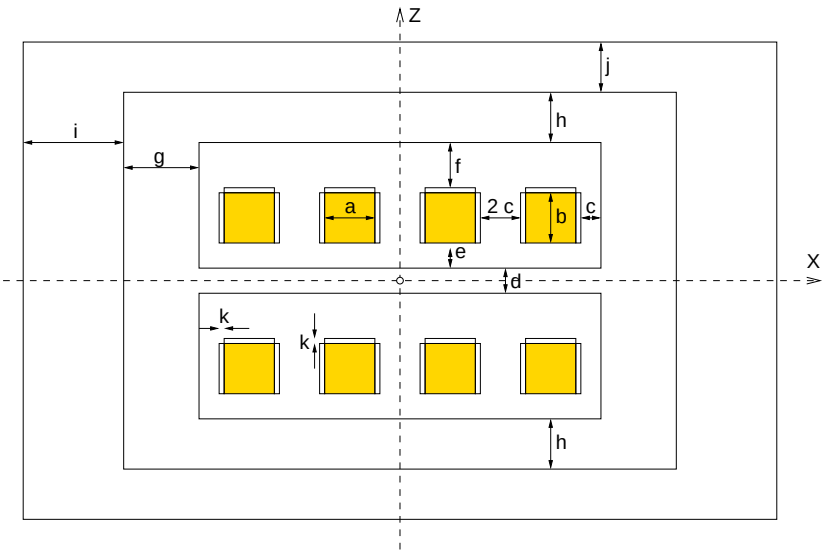

Figure 4.3: A 2-dimensional projection of a sample detector array with 4 detectors in x-direction (DNX=4) and two in z-direction (DNZ=2) indicating the geometry parameters as described in the text above.
a = cdte_dimx, **b** = cdte_dimz, **c** = gap_len, **d** = tray_width, **e** = gap_bot, **f** = gap_top, **g** = copper_wallx, **h** = copper_wallz, **i** = lead_wallx, **j** = lead_wallz, **k** = paint_th.

Upon execution of POISON the sequence of events must be specified. This can be done either interactively by entering the commands one by one on the POISON prompt or by using a script file. This script file may be either passed as a command line argument or written to stdin.
First an event generator has to be selected and configured. As different generators the user can choose between

- “KielGen”,
- “particleGun”,
- “Decay0”.

For the generators KielGen and Decay0 a location of the radiation source can be chosen from a fixed list. If not specified otherwise, the source is homogeneously distributed over the specified region:

- in central detector
- in any detector
- in paint on top and sides of central detector
- in paint on top and sides of any detector
- in copper
- in lead
- in lead surface above detectors (copper_dimx $\times$ copper_dimy $\times$ 0.1mm)
- at a fixed calibration point

Note that some locations may be identical for a single detector setup. For an even sized number of detectors in X, Y and/or Z direction the “central detector” is defined as the one which has X, Y or Z coordinates immediately below than the centre of gravity as shown in figure 4.4. The numbering of the detectors starts with number one as the detector with the lowest X, Y and Z coordinates, i.e. the front most and leftmost detector of the bottom layer, counting in X direction.

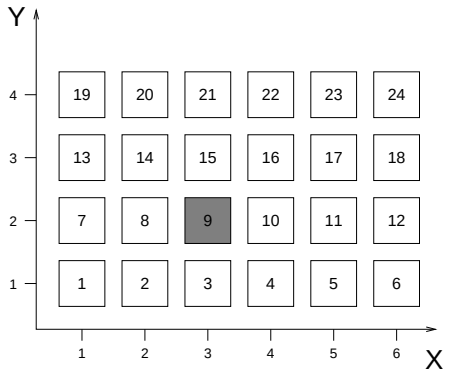

Figure 4.4: Definition of the central detector marked in grey in an even numbered array. The detector numbering starts with the bottom layer counting line by line from the left.

Additionally, for the calibration source its position, direction and opening angle must be set with extra commands.
In order to start multiple simulations of the same configuration, the seed of the random number generator must also be specified by the user in order to achieve different results. Two identical setups with the same commands will result in the same output of POISON, unless changing the used version of POISON.
The event data output can be redirected by a special command to a file given by the user. If not specified, the output will be directed to the console, together with information from POISON, like the used geometry or processes.
"KielGen" has been developed as a powerful generator which can generate many types of events that can be selected from a list. These types of events, called "mode" can be selected with the **/kielgen/mode <mode>** command with mode being a number:

0: single mono-energetic electrons

1: $0\nu\beta^-\beta^-$ $(0^+ \Rightarrow 0^+)$ [Tre95, eq.4]

2: $2\nu\beta^-\beta^-$ $(0^+ \Rightarrow 0^+)$ [Tre95, eq.16]

3: single mono-energetic gammas

4: gammas from the ^{238}U decay chain

5: gammas from the ^{232}Th decay chain

6: single mono-energetic positrons

8: $0\nu\beta^+\beta^+$ $(0^+ \Rightarrow 0^+)$ [Tre95, eq.4]

9: simple allowed β^- spectrum (taken from GEANT4 neutron decay [Ago03])

10: gammas from the decay of ^{60}Co (1173 keV, 1332 keV)

11: gammas from the decay of ^{152}Eu

12: ^{113}Cd beta spectrum according to [Dan96a]

13: gammas from ^{113}Cd(n,γ)^{114}Cd ("thermal neutrons on CdTe")

14: gammas from the decay of ^{88}Y

15: $0\nu\beta^-\beta^-$ $(0^+ \Rightarrow 0^+)$ spectrum, with right handed currents [Tre95, eq.8]

16: single mono-energetic alphas

17: single mono-energetic neutrons

18: ^{208}Tl decay: 2614 keV and 538 keV gammas and beta distribution

19: gammas from ^{117}Cd beta decay (from neutron activation)

20: gammas from the decay of ^{133}Ba.

Some of these modes, like the mono-energetic particles or (double) beta decays require that an energy is set via the **/kielgen/energy <energy> <unit>** command. The value is ignored for the other modes where internal tables and calculations are used.

The Q-value for the $2\nu\beta\beta$ events (mode 2) must be exactly specified because some internal parameters are taken from a table. Possible values are:
Q = 534 keV(^{114}Cd), 868 keV(^{128}Te), 1001 keV(^{70}Zn), 2529 keV(^{130}Te), 2805 keV(^{116}Cd).

The gamma energies of the decay chains and other isotopes are taken from [Wah96, Shi78].

An alternative event generator is DECAY0 which is the initial version of DECAY4 [Pon00], a Monte Carlo generator for the simulation of double beta processes and decays of radioactive nuclei provided by V. Tretyak. It is also used in other double beta experiments. DECAY0 is an external program shipped with POISON, which is able to generate an event file containing the initial particles and their momenta of an arbitrary number of events.

To generate such an event file the DECAY0 program is started offering an interactive menu. Once generated, the output file can be fed into POISON using the "Decay0" generator. The GEANT4 class to read in the event file has been kindly provided by L. Pandola.

GEANT4 also provides a default generator called "particleGun" which imitates a particle beam as used in accelerator experiments. This generator is not quite suitable for double beta experiments, however, it has been used for testing in the early stage of POISON and has been left in the code for simplicity. Configuration of this generator includes setting the particle type, the beam direction, the energy of the beam particles, a starting position of the beam, a polarisation of the beam particles and the number of particles to be generated per bunch. The generator also provides the possibility to shoot ions of arbitrary properties like their atomic number, atomic mass, charge and excitation energy.

After setting up the generator and location events can be produced with the command **/run/beamOn <n>** where n is the number of events to be generated. Then the generator settings, or even the generator itself, may be changed and another number of events with the new settings can be generated by the command above.

If POISON has been configured to use a graphical interface, it can be used to check the geometry of the setup and to show the particle tracks of events. As a graphical back end different graphics systems are possible. The graphics output may be either displayed immediately in a window, or written to a file in order to be viewed by external programs. The graphical back end "DAWNFILE", for example, creates a file which can be converted to PostScript using DAWN[6] [Kaw97]. A sample display using DAWN is shown in figure 4.5. The geometry is a $3\times3\times3$ array of detectors in a lead and copper shielding. 2000 ^{113}Cd beta events have been started in the central detector. The tracks of the electrons are indicated by red colour, photons by green colour. The sequence of commands is given in appendix E.1.

Another output format is VRML[7]. These files can be viewed with e.g. FreeWRL[8]. All graphics systems allow the user to choose the viewpoint from which to look at the scene, a magnification factor for the view and other options. In order to see the tracks of the particles, GEANT4 has to be configured to store the trajectories and draw them after an event.

[6] **D**rawer for **A**cademic **W**riti**N**gs, http://geant4.kek.jp/ tanaka/
[7] **V**irtual **R**eality **M**odeling **L**anguage
[8] http://freewrl.sourceforge.net/

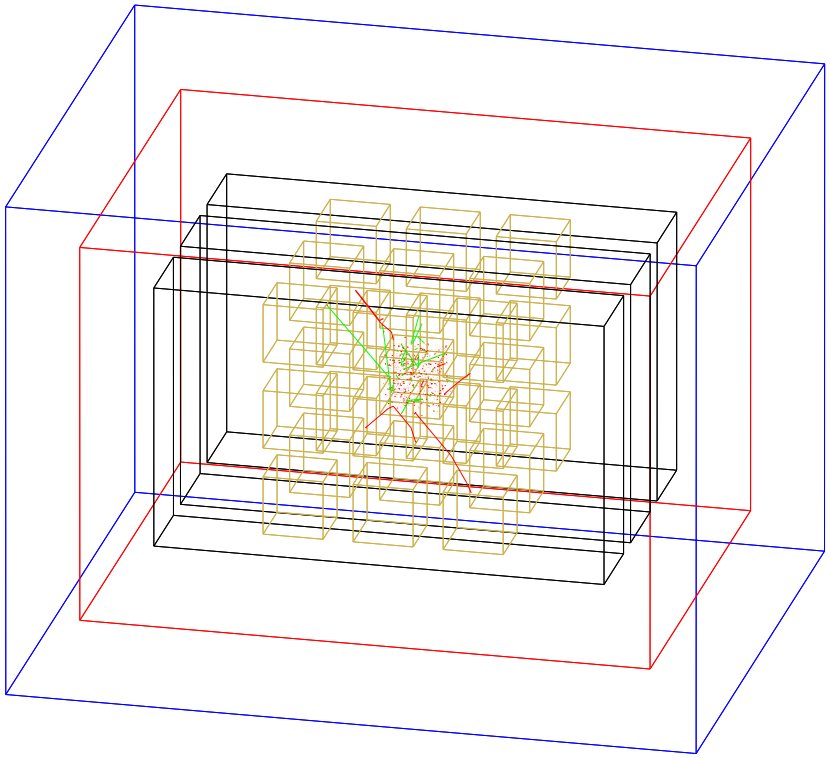

Figure 4.5: 3-dimensional event display showing the detector setup and particle tracks. The display is an accumulation of 2000 ^{113}Cd beta events started in the central detector of a 3×3×3 array of 1 cm^3 CdZnTe detectors as defined in the input file given in appendix E.1. The blue and red cubes indicate the outer boundary of the lead and copper shielding respectively. The three black cuboids mark the outer boundaries of the cavities in the copper hosting the detectors which are shown in brown. The red lines indicate the tracks of the electrons, the green lines represent photons coming from Bremsstrahlung.

In order to analyse the simulated events, the data output of POISON has to be interpreted. In the output file events are saved as follows:

$$\text{Eventnumber}\ \ \mathrm{E_1}\ \ \mathrm{E_2} \ldots \mathrm{E_n}\ \ \mathrm{E_{Sum1..n}}\ \ (\text{keV})\ \ \mathrm{E_{Input}}$$

with the numbering of the detectors as defined before:

$$\text{Detectornumber} = x + \text{DNX} \times (y-1) + \text{DNX} \times \text{DNY} \times (z-1)$$

with $x = 1..\text{DNX}$, $y = 1..\text{DNY}$ and $z = 1..\text{DNZ}$ which is the position of the detector in x, y and z direction. In appendix E.2 the corresponding data output of the event display shown in figure 4.5 is shown partially together with the complete informational output. Future versions of POISON will produce a ROOT file containing the data.

4.3.2 The Prototype Geometry

As already mentioned, the geometry of the Prototype has been implemented in a separate branch of POISON [McK05]. This branch was initiated in order to avoid broken code in the "production" version of POISON. The Prototype branch of POISON does not require any geometry file like the 3-dimensional array as all parameters are fixed. However, the same commands and data output are used to ensure compatibility of the semantics.
In figure 4.6 the geometry of the Prototype as implemented in the POISON branch is shown. The left figure shows the whole setup including the lead and copper shielding. The right figures show the projection of the Prototype detector seen from top and front respectively with the Pertinax holder indicated by magenta. The green dots are simulated electron tracks in the top layer of the Pertinax holder to check the congruence of the geometries of the detector setup and the event generator.

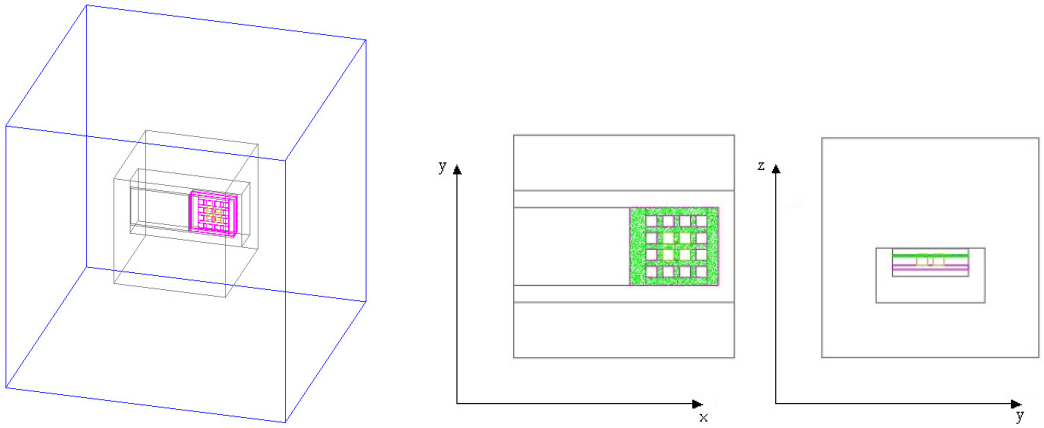

Figure 4.6: A display of the Prototype geometry is shown [McK05] as a 3-dimensional display in the left picture and two projections on the right side. The Pertinax holder is indicated by magenta colour. The green dots indicate the tracks of electrons started homogeneously in the upper layer to show consistency of the physical description of the Prototype geometry and the event generator.

With this setup the contribution of the radioactive contamination of the Prototype's construction materials was simulated. The result of the simulation is shown in section 5.3.4.

4.4 Adjustment of Monte Carlo to Data (Absolute Calibration)

For a cross check of the Monte Carlo program with real detector measurements, a simple defined setup has been realised. This measurement is intended to estimate detector effects which are not included in the simulation, such as the active volume or detector resolution. The finite resolution of detectors is always folded in after the simulation. The spectral response is estimated as a Gaussian shape for simplicity. A more detailed description will be included in a later version of POISON, when the charge transport and signal generation of the detectors can be simulated.
In figure 4.7 the geometry of the absolute calibration setup is shown. The four detectors of the Prototype array are placed inside their copper brick and covered by a 1 mm thick copper sheet. A calibration source is placed at 20 cm above the centre of the array. The whole setup is surrounded by 5 cm lead bricks. A point like calibration source has been simulated as can be seen from the tracks of the gammas indicated by the green lines. The source is isotropically emitting the gammas which are stopped by the surrounding lead shield.

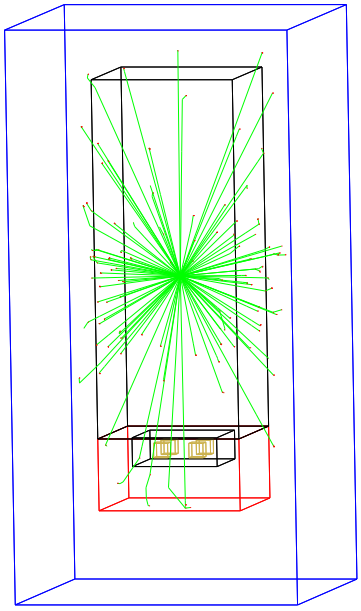

Figure 4.7: Schematic of the setup for the absolute calibration in POISON. The four detectors shown in yellow are located in a copper brick with a covering copper sheet of 1 mm thickness. Around the copper brick a lead shield of 5 cm is built which leaves an empty volume above the copper brick of about 20 cm. A point like source isotropically emitting gammas can be seen from the green lines representing the photon tracks which are stopped in the surrounding lead.

The above geometry resembles the setup with true detectors. Figure 4.8 shows the measured spectrum of detector D1 as a red line. For the calibration a ^{137}Cs source with an activity of 9 μCi = 333 kBq in the year 1981 has been used. Considering the half life of $T_{1/2}(^{137}\mathrm{Cs}) = 30.07$ a the activity of the source at the time of measurement has been calculated as 196 kBq. The data spectrum is compared to a simulation with the same geometry indicated by a black line. The measured energy resolution of the detector is folded onto the simulated spectrum. A clear discrepancy of the number of events in the photo peak is visible. The event rate in

the region of the Compton edge is comparable. However, the backscattering peaks and X-rays of copper and lead which lie around 90 keV are not simulated properly which is a hint to an insufficient description of the setup in the simulation. Investigations done by collaborators at the University of Birmingham using POISON have shown a good agreement between their measurements and simulations of about 10 % accuracy [Ful05]. Therefore, the discrepancy shown above is attributed mainly to the incomplete modelling of the setup.

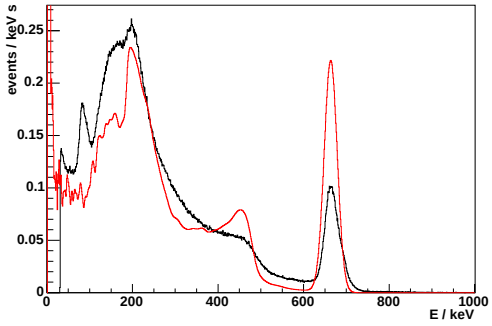

Figure 4.8: Comparison of the simulated spectrum of a ^{137}Cs calibration source (red) and the data of detector D1 (black). The measured energy resolution of this detector has been folded into the simulated spectrum.

In table 4.1 the measured photo peak efficiencies for the four detectors of the Prototype array and the simulation are given. The efficiencies of the detectors have been measured for two bias voltages 900 V and 1200 V, because during data taking detectors D1 and D2 were operated at 1200 V whereas D3 and D4 had a bias voltage of 900 V applied. A clear dependence on the bias voltage can be seen. The relative efficiency, which is the ratio of the event rates of each detector relative to D1 which has the highest event rate is shown as well. This value is used in analyses of decays to normalise the data spectra of the measurement periods in order to correct for the detection efficiency.

Detector	Rate (900V) / Hz	Rate (1200V) / Hz	Rel. Eff. / %	Abs. Eff. / %
simulation	8.40		–	$\equiv 1.00$
D1	5.29	4.52	$\equiv 1.00$	0.54
D2	4.54	3.79	0.84	0.45
D3	3.04	3.30	0.67	0.36
D4	3.58	3.71	0.79	0.43

Table 4.1: Measured photo peak activities at the two bias voltages 900 and 1200 V compared to the efficiencies calculated with POISON. A ^{137}Cs calibration source with a mono-energetic gamma line at 662 keVhas been used. Detectors D1 and D2 have been running with 1200 V bias, whereas detectors D3 and D4 had a bias voltage of 900 V during data taking runs. The efficiencies are calculated from the corresponding rate.

The dependence of the spectral shapes on the bias voltage applied to the cathode has been investigated as well. Figure 4.9 shows the comparison of a ^{137}Cs calibration spectra with a bias voltage of 900 V and 1200 V for each detector. The largest impact can be seen for detector D1, where not only the photo peak efficiency changes, but also the energy resolution.

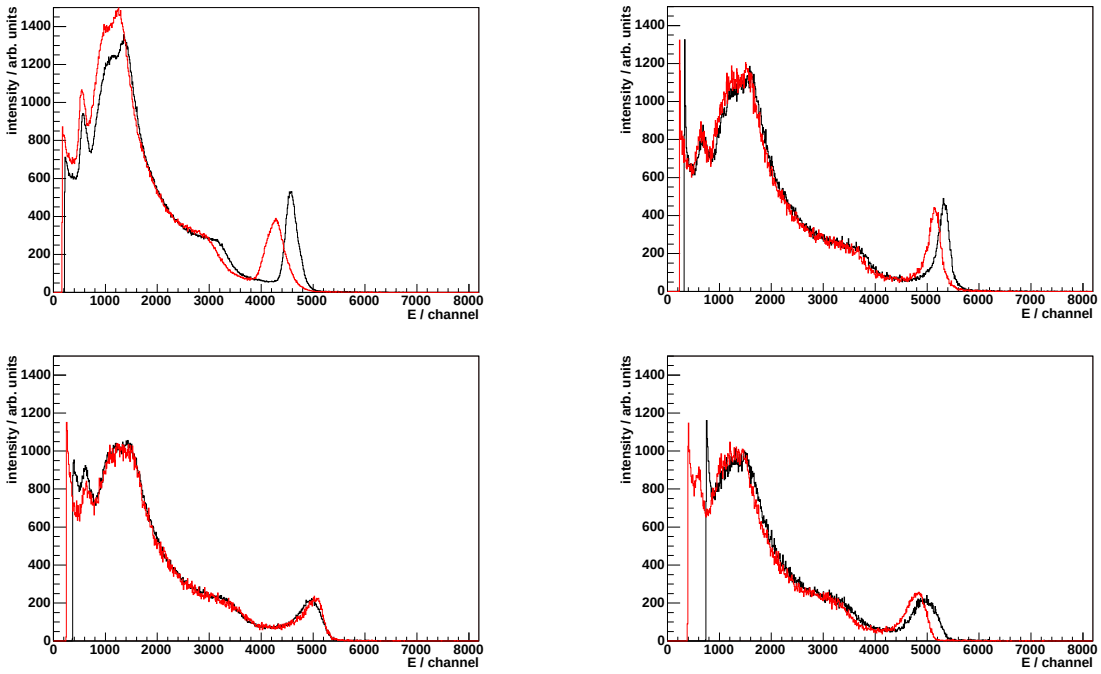

Figure 4.9: The dependence of the spectral shape of a mono-energetic gamma source (^{137}Cs) and the applied bias voltage is shown for detectors D1−D4 from top left to bottom right. The measured spectra are shown for 1200 V and 900 V indicated by black and red respectively. The spectra are normalised to 1 h.

Another effect of charge collection in the detector can be seen in figure 4.10. Here, a detector has been irradiated with the low energy gamma source ^{57}Co with the main photo peak at 122 keV. By placing the source to either the cathode or anode side of the detector the charge carriers in the detector are created just below the electrode. An asymmetry in the charge collection can be clearly seen. The recorded photo peak is broader and higher if the charge carriers are created near the cathode. However, this effect appears only for events in the uppermost 0.5 mm [eV-04].

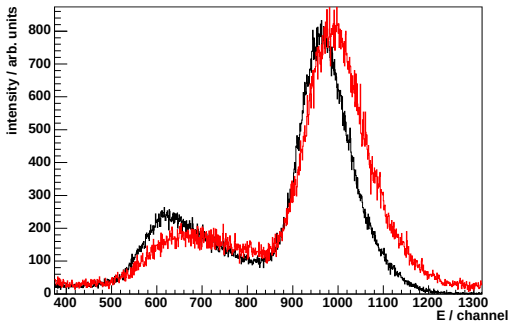

Figure 4.10: An asymmetry is shown for events generated near the cathode (red) and anode (black) in CdZnTe detectors with CPG readout. ^{57}Co has been used as a gamma source.

4.5 Simulation of Signal Events

For the calculation of the half lives in chapter 5 the efficiencies to detect the events searched for need to be known. The detection efficiencies for $0\nu\beta\beta$ decays to the ground state ($g.s.$) and excited states have been simulated using the momentum distributions calculated with KielGen according to the equations for $0^+ \rightarrow 0^+$ transitions from [Tre95]. The $0^+ \rightarrow 2^+$ transitions to excited states, however, are only roughly modelled by these distributions. In figure 4.11 the $0\nu\beta^-\beta^-$ spectrum of ^{116}Cd in a 1 cm^3 detector is shown as a simulation of an ideal detector indicated by the black histogram. The red histogram illustrates the broadening of the spectrum if an energy resolution of 5 % is folded on the same data.

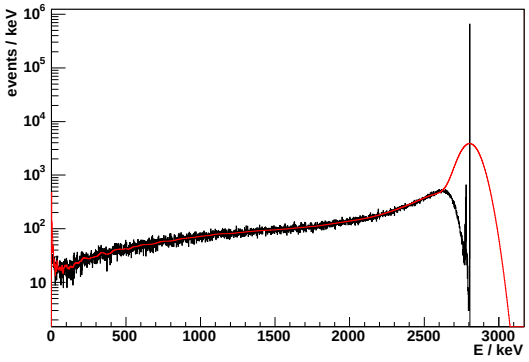

Figure 4.11: The spectrum of 10^6 simulated $0\nu\beta^-\beta^-$ ^{116}Cd events with a Q-value of 2.805 MeV is shown for a 1 cm^3 CdZnTe detector as a black histogram. The red histogram corresponds to the same data, however, folded with an energy resolution of 5 % which is the average energy resolution of the worst detector in the 2×2 Prototype. The difference of the full energy efficiency calculated from both spectra is a 4 % effect.

By fitting a Gaussian distribution to the energy resolution folded spectrum an efficiency of 67.79 % is obtained opposed to 65.08 % events in the 2.80 MeV bin of the unfolded data which is a 4 % effect on the efficiency. Nevertheless, the unfolded single bin efficiency has been taken for the following analyses. The efficiency ε to detect the full energy of the two electrons for the $\beta^-\beta^-$ isotopes in CdZnTe is shown in table 4.2.

For decays to excited states two signal searches are possible. The first is to detect only the electron energies, which is a distinct signature. However, it may be fortunate to extract the limit from the full absorption peak, i.e. the energy of the two electrons plus the photon energy which is indistinguishable from the decay to the ground state. Thus, only a combined half life limit can be given. Using the two searches, it is obvious that not only the full escape efficiency, but also the full absorption efficiency for gammas has to be calculated. The efficiency to detect gammas from decays to excited states will be boosted when considering a large array of crystals. Then the signal would be the reduced Q-value in one detector and the full gamma energy in any of the other detectors.

The efficiency for the full detection and full escape of a photon as a function of energy is depicted in figure 4.12.

Isotope	Level / keV, J^P	Energy / keV	ε / %
^{70}Zn	$g.s.$, 0^+	1001	92.02 ± 0.19
^{114}Cd	$g.s.$, 0^+	534	97.34 ± 0.20
^{116}Cd	$g.s.$, 0^+	2805	65.08 ± 0.16
	1294, 2^+	1511	84.75 ± 0.18
	1757, 0^+	1048	91.26 ± 0.19
	2027, 0^+	778	94.65 ± 0.19
^{128}Te	$g.s.$, 0^+	868	93.72 ± 0.19
	443, 2^+	425	98.31 ± 0.20
^{130}Te	$g.s.$, 0^+	2529	69.40 ± 0.17
	536, 2^+	1993	77.42 ± 0.18
	1121, 2^+	1408	86.40 ± 0.19
	1794, 0^+	735	95.31 ± 0.20

Table 4.2: The efficiencies ε to detect the full energy of the two electrons in $0\nu\beta^-\beta^-$ decay to the ground state ($g.s.$) and excited states (level, J^P).

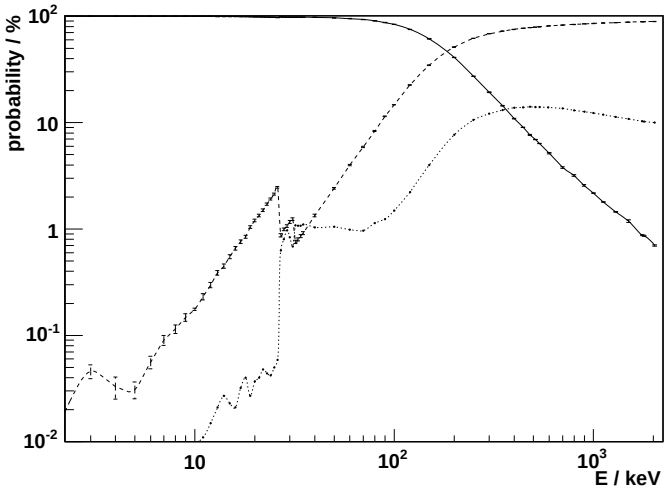

Figure 4.12: The efficiency to detect a gamma of a given energy in a $1 \times 1 \times 1$cm^3 CdZnTe detector with its full energy (solid line), partial energy (dotted line) and no energy (dashed line) as obtained via simulations with POISON.

Chapter 5

Analysis

During the past four years of the COBRA experiment there have been several data taking phases using different setups. The following list gives a short overview of the setups used in this thesis.

A *CPG2 detector in Dortmund, PC-MCA (with active veto)*
1117 h measurement with a 0.5 cm^3 CdZnTe detector from eV-PRODUCTS.
Together with 1645 h of data from a 1 cm^3 CdTe detector from EURORAD the measurements resulted in a publication with new and improved limits on double beta decay modes [Kie03].

B *CPG2 detector in the LNGS, PC-MCA (without veto)*
2015 h measurement with the above detector for studies of the reduced muon background in the LNGS compared to the Dortmund setup.

C *Prototype array in the LNGS, CAMAC DAQ*
4781 h measurement with the four 1 cm^3 CdZnTe detectors of the 2×2 Prototype array in the Pertinax holder.
386.6 h measurement with one of the remaining detectors of the 2×2 Prototype array after remounting to the Delrin holder.

D *Prototype array in the LNGS, VME DAQ*
181.9 h measurement with one of the remaining detectors of the 2×2 Prototype array after remounting to the Delrin holder.

In the following sections the data of the Prototype in the Pertinax holder taken with the CAMAC DAQ will be analysed and compared to the old already published data from the CPG2 detector measured in Dortmund. Also a first insight of new data with the remounted Prototype using the CAMAC and VME systems will be given providing a comparison of the background for the old Pertinax holder with the new Delrin holder.
After this, methods to reduce the background in the measured spectra will be discussed. Finally, the half life of the 4-fold forbidden unique β spectrum of ^{113}Cd and limits on the half lives of $2\nu\beta^-\beta^-$ and $0\nu\beta\beta$ decays of Cd, Zn and Te isotopes will be calculated. A compilation of half lives of double beta decays from the year 2002 can be found in [Tre02]. As an addition to the above analyses, lower limits on the charge non-conserving processes of the radiative electron decay and the decay of ^{113}Cd to neutral particles will be given.

5.1 Data Selection

Due to instabilities in the DAQ systems and problems with the detectors, the recorded data sets have to be "cleaned" before they can be analysed. Therefore, an individual inspection of the data sets from different detectors and DAQ systems has to be done.

5.1.1 CPG2

The selection of data taken with the CPG2 detector for the two measurement periods in Dortmund and the LNGS follows the same scheme. Both data sets have been recorded with the PC-MCA described in section 3.1, using 30 min runs in Dortmund and 2 h runs in the LNGS. Few runs lasted longer due to problems with the control script. From all runs, those with exceptional high count rates have been removed. The threshold of this cut has been determined by histogramming the count rate per run and fitting a Gaussian distribution to it. Runs with a higher count rate than the lower 90 % of the fitted Gaussian are rejected. Figure 5.1 shows the event rates of the remaining runs of data taken in the LNGS documenting stable operation of the detectors.

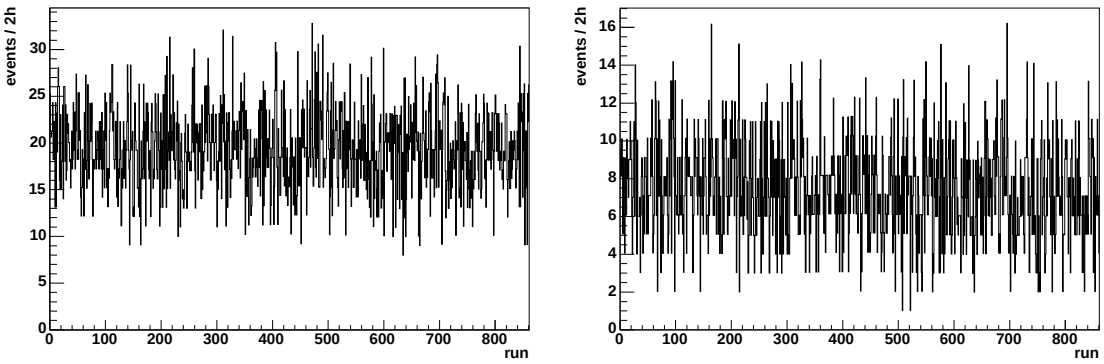

Figure 5.1: The counting rates of the CPG2 detector running in the LNGS for each run normalised to 2 h are shown for the energy intervals 100-300 keV in the left histogram and 300-1000 keV in the right histogram.

The calibration of the detector has been done using ^{22}Na, ^{60}Co, ^{133}Ba, ^{137}Cs, ^{228}Th and ^{241}Am as gamma sources. Figure 5.2 shows the measured positions of the photo peaks as a function of their energy in the left diagram.
The resulting functional dependence of the energy E on the channel number chn can be expressed via a linear equation:

$$E = (\text{chn} \times m + a) \times \text{keV} \tag{5.1.1}$$

with the slope $m = 0.9980$ and the offset $a = -5$ for this particular calibration.
With these measurements also the energy resolution as a function of energy has been determined as shown in the right diagram in figure 5.2. The resulting energy resolution as FWHM of the CPG2 detector during operation in the LNGS is determined as

$$\Delta E_{\text{CPG2}}(E) = 3.41\% \cdot E + 8.0\,\text{keV}. \tag{5.1.2}$$

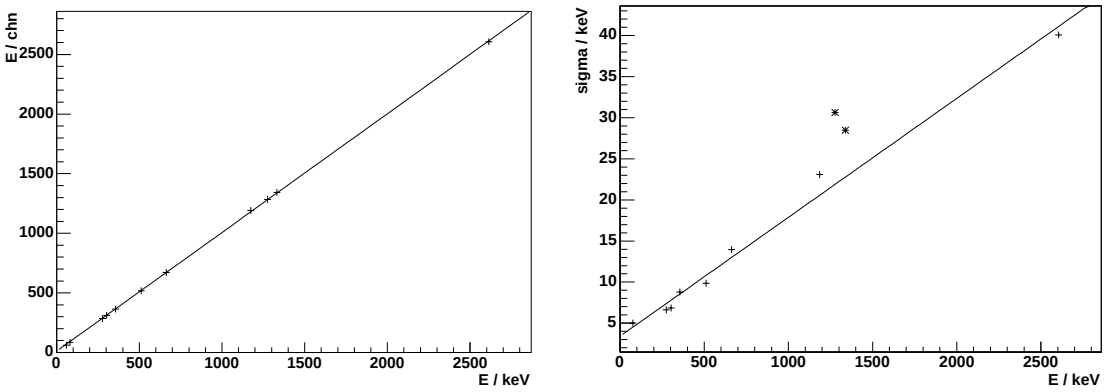

Figure 5.2: The calibration (left) and Gaussian width σ (right) of the CPG2 detector using the gamma lines of ^{22}Na, ^{60}Co, ^{133}Ba, ^{137}Cs, ^{228}Th and ^{241}Am are shown. The width of the fitted Gaussian distribution is given according to equation 2.1.3. The energy resolution of the detector in FWHM is a factor 2.35 larger than σ as shown in equation 2.1.4.

In figure 5.3 a comparison of the two data sets for the CPG2 detector taken in Dortmund and in the LNGS is shown. No significant improvement in background is visible at low energies. A slight reduction of background above 2 MeV is visible for the data taken in the LNGS. This is a hint on the improvement in the shielding of the setup from atmospheric muons. However, the smallness of the deviation is also a proof of the effectiveness of the active muon veto of the Dortmund setup. The low energy background can be attributed to the nearby electronics components which are located inside the encapsulation of the detector.

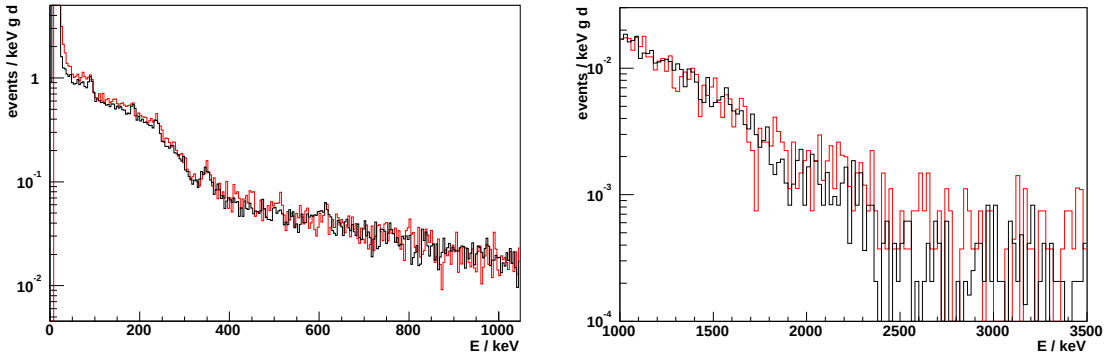

Figure 5.3: A comparison of the CPG2 data taken in Dortmund with an active veto (red histogram) and in the LNGS with an active veto (black histogram) is shown for the energy regions $0-1$ MeV and $1-3.5$ MeV. Only for the high energy region above 2 MeV a difference in the count rate is visible due to the reduced muon flux in the LNGS. The low energy background is dominated by radioactive contamination in the vicinity of the detector, i.e. the nearby electronics components. Clearly visible is the shoulder of the ^{113}Cd beta decay and gamma lines from the ^{238}U and ^{232}Th decay chain, such as the 238.6 keV and 351.9 keV gamma lines. The background level in the $0\nu\beta\beta$ region of ^{116}Cd and ^{130}Te at 2.805 MeV and 2.529 MeV respectively is enhanced from about $5 \cdot 10^{-4}$ to $2 \cdot 10^{-4}$ events per keV, gram and day.

5.1.2 Prototype

For the acquisition of the 2×2 Prototype data the CAMAC DAQ has been used providing data on an event-by-event basis which makes quality cuts more effective. However, due to the dysfunctions of the CAMAC ADCs described in section 3.2 the full spectrum has to be subdivided into two parts – one lower energetic part up to 600 keV and one higher energetic part above 600 keV – and cleaned accordingly.

Due to the different thresholds of the ADCs the higher energetic data set with increased statistics can only be used above 600 keV. The low energy data set has to be taken for lower energetic analyses as the threshold is below 100 keV for all its periods.

All periods taken with the Prototype setup are named according to their starting date. The complete data set comprises the periods described in table 5.1. For some periods, ADCs have been taken offline because of hardware problems.

		Integral Counts			
Period Name	Length / h	ADC 1	ADC 2	ADC 3	ADC 4
2003_09_09*	286.8	11124	6131	*-offline-*	4382
2003_09_23*	503.0	17143	10951	8718	7820
2004_01_30*	427.5	6885	31555	7030	4680
2004_02_18*	453.0	7462	31986	7523	10649
2004_04_07	501.1	4914	17018	11207	10586
2004_05_05	430.0	2453	6094	23163	7449
2004_05_27	465.7	20417	17850	6788708	8136
2004_06_16	619.9	*-offline-*	37738	*-offline-*	11174
2004_07_14	1094.1	1975889	428902	346335	61068

Table 5.1: Statistics of the periods taken with the 2×2 Prototype using the CAMAC DAQ. The ADC number corresponds to the detector number except for the periods marked with *, where detector D1 and D2 are swapped. The number of events per period corresponds to its length in most of the cases. Some periods show a significantly enhanced number of events. This is mainly due to either bursts produced by the detectors or by defective ADCs.

The overall stability of the data taking is shown exemplarily for detector D4 in period 2004_07_14 in figure 5.4. The left histogram shows the number of events per 1 hour run, in the right histogram the respective cumulation of all data files is shown. The distribution of the number of events per hour can be well fitted by a Gaussian distribution. The cut value is then defined as the count rate below which 90 % content of the fitted Gaussian distribution is located. The resulting cut for this period is 34.

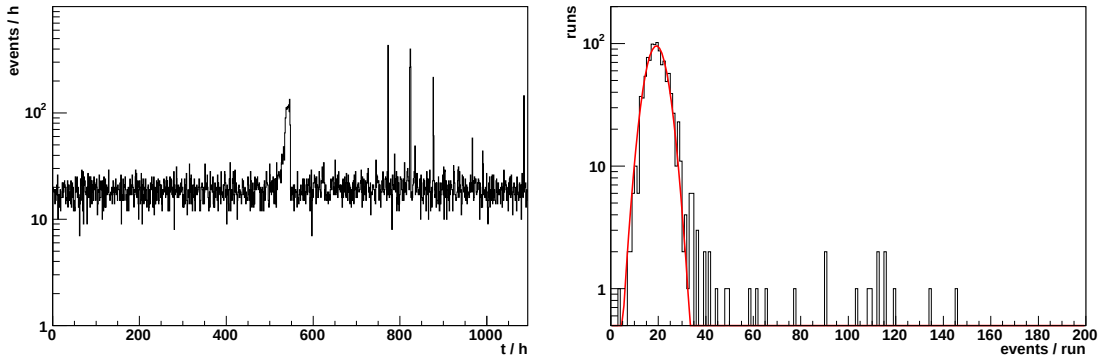

Figure 5.4: The distribution of events in detector D4 per run in period 2004_07_14 is shown in the left histogram. The right histogram shows the same data ordered by the number of events per run. The distribution follows a Gaussian shape. Runs with count rates higher than the single sided 90 % content of the fitted Gaussian distribution are rejected. The effective value for this period is 34.

The threshold of ADC number 1 is rather high with a value of about 500 keV. The threshold was chosen that high to discriminate true data events from sub threshold events generated by the ADC module itself as shown in figure 5.5. Therefore, its data cannot be included in the low energy data set used for the ^{113}Cd analysis reducing the total amount of data by 25%. Nevertheless, its data is used for the analyses in the higher energy region.

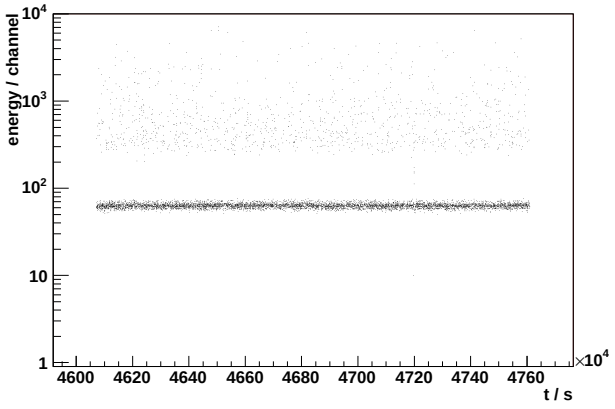

Figure 5.5: "Waterfall" plot of ADC 1 in period 2004_01_30 showing the time of arrival and energy of each event. The threshold of the ADC is approximately set to channel 250, where the physical spectrum ends. A band of sub threshold events can be seen around channel 60 which corresponds to about 84 % of all recorded events.

Usually, the detectors have been calibrated with ^{60}Co and ^{137}Cs sources prior to and after each period. Because of the low activity of the available ^{228}Th source only a few calibrations were performed with it. Additionally, being visible in most data spectra, the 351.92 keV gamma line of the decay of ^{214}Pb in the ^{238}U decay chain has been used as an intrinsic calibration line if possible. Figure 5.6 shows an example of such an auto-calibration.

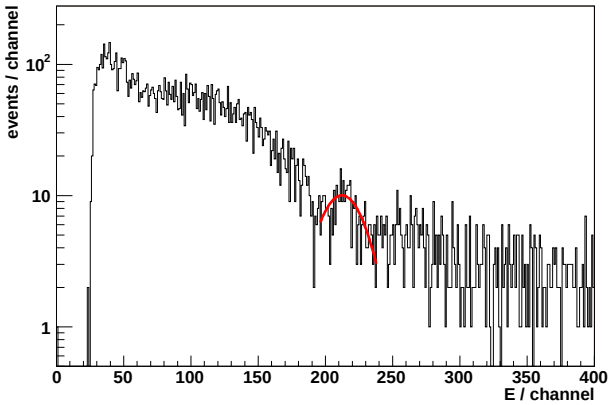

Figure 5.6: The spectrum of detector D4 in period 2004_04_07 is shown with a fit of a Gaussian distribution to the 351.92 keV gamma line of ^{214}Pb denoted by the red line. The centroid of this peak is taken as an additional calibration point.

Because of the rather high energetic calibration lines which are used in a standard calibration (661.66 keV for ^{137}Cs, 1173.2 keV and 1332.5 keV for ^{60}Co) for the low energy data set, the intrinsic 351.92 keV ^{214}Pb gamma line has been used as a selection criterion for the periods to be included. The calibrated spectra have been overlaid and all periods where the gamma line is shifted by more than 10 keV are rejected. This cut is loosened to 20 keV for the high energy data set. This way a precise calibration is assured for the low energy data set which is important for the ^{113}Cd analysis.

Furthermore, in order to analyse the ^{113}Cd beta spectrum for the low energy data set, a cut on the count rate of 1 h runs of data between 100 keV$-$320 keV is set to discriminate those runs where the exponential noise dominates the count rate. Again, the cut is done by fitting a Gaussian distribution to the number of events per run and keeping only the lower 90 % content of the Gaussian distribution. This cut reduces the amount of data by about 57 hours. For the high energy data set this cut is omitted as the noise level does not exceed 200 keV.

Another 6 days of measurement had to be discarded for detector D3, where the ADC suffered from a moving lower threshold probably due to warming up effects. Here, this movement can be documented by the comparison of the pre- and post-calibration which do not match. However, for the total period, reduced by the time of moving threshold, the post-calibration gives a good spectrum. In figure 5.7 the effect of the moving threshold is shown in a waterfall plot. For this period a cut was set to include only events after $t > 62.5 \cdot 10^6$ s.

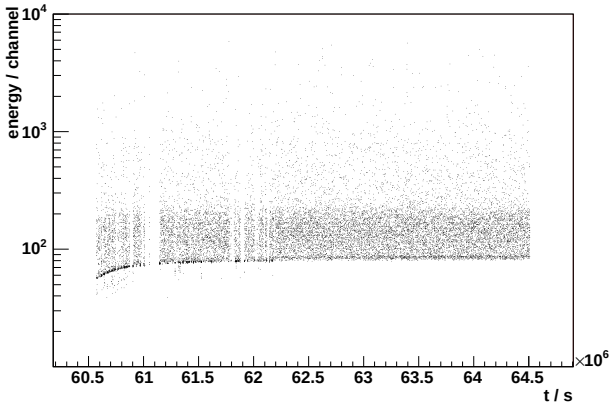

Figure 5.7: Waterfall plot showing the drifting of the lower threshold for detector D3 in period 2004_07_14. The period has been cleaned from noisy runs before plotting. A cut was set to include only events after $t > 62.5 \cdot 10^6$ s. After this point in time the behaviour of the ADC is stable.

The linear dependence of the energy resolution as a function of energy has been checked just before disassembling the Pertinax Prototype using ^{152}Eu, ^{133}Ba, ^{57}Co, ^{241}Am, ^{60}Co and ^{137}Cs sources. For the analyses the energy resolution of the detectors has been extracted from the calibrations between periods. An average of the energy resolution in FWHM of detectors D1−D4 is given in equations 5.1.3−5.1.6.

$$\Delta E_1(E) = 4.37\% \cdot E + 48.2\,\text{keV} \quad (5.1.3)$$
$$\Delta E_2(E) = 4.58\% \cdot E + 44.4\,\text{keV} \quad (5.1.4)$$
$$\Delta E_3(E) = 4.75\% \cdot E + 27.0\,\text{keV} \quad (5.1.5)$$
$$\Delta E_4(E) = 5.59\% \cdot E + 57.1\,\text{keV} \quad (5.1.6)$$

To extract the efficiency of the four detectors, a relative calibration of the detectors has been performed as described in section 4.4. For the analyses of the spectra these relative efficiencies have to be considered. The uncertainty of the absolute efficiency of the detectors is estimated to be about 20 %. A top-bottom asymmetry of events generated in different interaction depth in the detector leading to different spectral shapes as described in the same section is neglected completely. Instead a systematic error is calculated to be of 2 % in the peak position.

The remaining amount of good data after applying the cuts mentioned above is shown in table 5.2. The sum of 863.23 g · d for the low energy and 2594.64 g · d for the high energy cuts have to be compared to 134.5 g · d of data taken with the CPG2 detector in Dortmund and 242.6 g · d taken in the LNGS. This improvement is mainly due to the 8 times larger mass of the Prototype detector compared with the CPG2 detector.

Detector	Low Energy / g · d	High Energy / g · d
D1	213.62	981.44
D2	—	730.21
D3	343.45	343.45
D4	407.02	875.18
sum	964.09	2930.29

Table 5.2: Remaining statistics of the low and high energy data sets after cleaning. For the low energy data set D2 is missing because of a too high threshold of the ADC and calibration problems.

Nevertheless, only half of the 4781 h measurement which would correspond to a total of 5179.4 g · d could be used. As a consequence of all these cuts which are necessary due to the shortcomings of the aged CAMAC electronics, the installation of the new VME DAQ is motivated.
The final spectrum of the Prototype using the high energy cuts is shown in figure 5.8. This data set is used for most of the following analyses except for ^{113}Cd and other low energy analyses for which the low energy data set is used.

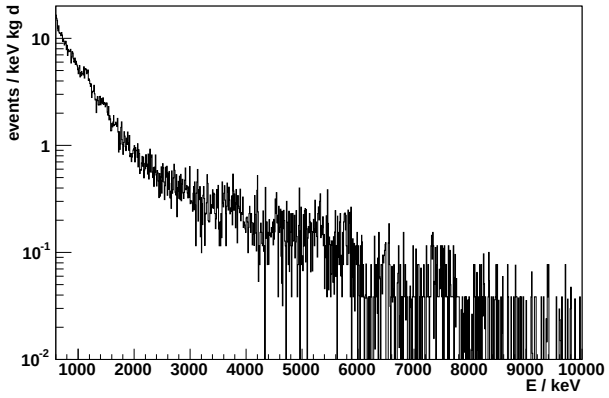

Figure 5.8: Total spectrum of the data taken with the Prototype in the LNGS of 2.595 kg·d statistics with a binning of 10 keV is shown. The background level in the $0\nu\beta\beta$ region of ^{116}Cd at 2.805 MeV is about 0.4 events per keV, kg and day. The background in form of alphas coming from the the natural decay chains of ^{238}U and ^{232}Th can be clearly seen by the clustered number of events at 5.8 MeV and 7.7 MeV. This contamination is located in the passivation paint covering the detectors.

5.2 Statistical Considerations

Before extracting the half lives of different decays from the before mentioned data sets, the underlying mathematical mechanisms have to be discussed. A good introduction to the analysis of spectra can be found in [Gil95, Leo92].
The radioactive decay law is given as

$$R = \frac{dN}{dt} = -\lambda N \tag{5.2.7}$$

with the decay rate R, also known as activity. It is proportional to the number of decay candidates N. This is a differential equation which can be solved with an exponential ansatz

$$N(t) = N_0 \cdot e^{-t\lambda} \tag{5.2.8}$$

with the initial number of decay candidates N_0. The decay constant λ is the reciprocal of the slope of the exponential function which is in turn connected to the half life of the decay. The half life is the time interval in which the number of remaining decay candidates is reduced to half of the initial amount. This is the commonly used value for radioactive decays.

$$N(t) = N_0 \cdot (1/2)^{-t/T_{1/2}}. \tag{5.2.9}$$

By measuring a decay rate only a number of events per time interval can be obtained, as radioactive decay is a statistical process. The measured value is

$$R = \frac{C}{\epsilon\ \Delta t} \tag{5.2.10}$$

with the number of detected counts C in a time span Δt. The detection efficiency ϵ has to be considered as well.
If the half life is much longer than the measuring time, the number of decay candidates is constant per time interval. In this case the decay rate equals the measured rate R. Otherwise, the number of detected events is

$$C(t_0, t) = N_0 \cdot (1/2)^{-t_0/T_{1/2}} - (1/2)^{-t/T_{1/2}} \quad \text{with } \Delta\mathrm{t} = \mathrm{t} - \mathrm{t}_0. \tag{5.2.11}$$

5.2.1 χ^2-Method to Extract an Upper Limit of Signal Events

In order to calculate half lives of decay processes the number of events attributed to this decay has to be determined from the measured data. To accomplish this, the background and signal model must be fitted simultaneously to the data. In some cases the background may be so high that only an upper limit of events which may be hidden in the background can be given leading to a lower limit on the half life of the searched process. The algorithm used to extract the upper limits of events is based on the calculation of χ^2 for a background and signal+background model [Kie03].
The background around the position of the peak under investigation is fitted with an exponential function or a constant depending on the energy. For searches below 2 MeV the background can be described by an exponential function. For searches above 2 MeV a constant background is assumed because of the low statistics in this region. Based on this background, a Gaussian shaped peak is then grown in addition to the background. The width of the Gaussian is given by

the energy resolution of the detector at the corresponding energy. With this signal+background model, the $\chi^2(n)$ can be calculated as a function of the number of events in the peak n. This function is used to check the null-hypothesis. The one sided 90% confidence level (C.L.) limit can then be extracted by taking the number of events where $\chi^2(n)$ is increased by 1.64 according to table 5.3 with respect to the null-hypothesis $\chi^2(n=0)$.

Probability Interval α	One Sided Confidence / %	Two Sided Confidence / %	k_α	$\Delta\chi^2$
0.1587	84.13	68.27	1.0	1.00
0.1	90.00	80.00	1.282	1.64
0.05	95.00	90.00	1.645	2.71
0.025	97.50	95.00	1.96	3.84
0.02275	97.73	95.45	2.00	4.00
0.01	99.00	98.00	2.326	5.41
0.00621	99.38	98.75	2.5	6.25
0.005	99.50	99.00	2.576	6.64
0.00135	99.87	99.73	3.0	9.00

Table 5.3: Probability intervals and associated degrees of confidence. The one and two sided confidence levels are shown for the probability intervals α. The k_α factor is the number of standard deviations from the centre of the Gaussian distribution. The variance of n is defined as $var(n) = \sigma^2(n)$, thus $\Delta\chi^2 = {k_\alpha}^2$ [Gil95].

With a measured number of events or an upper limit, the half life of an isotope can be calculated with the following equation:

$$T_{1/2} = \frac{N_0 \cdot \ln 2 \cdot t \cdot \epsilon}{n} \tag{5.2.12}$$

where n is the number of observed events, t is the measuring time, ϵ is the efficiency to detect such an event and N_0 is the number of atoms in the sample. For a given mass m of the sample and an isotopic abundance a_{iso} of the decaying isotope, the number of atoms can be calculated as follows:

$$N_0 = \frac{N_{\mathrm{A}} \cdot \mathrm{m} \cdot \eta_{\mathrm{el}} \cdot a_{\mathrm{iso}}}{\langle \mathrm{m}_{\mathrm{CZT}} \rangle}. \tag{5.2.13}$$

Here, $N_A = 6.022 \cdot 10^{23}\,\mathrm{mol}^{-1}$ is Avogadro's number and $\langle \mathrm{m}_{\mathrm{CZT}} \rangle$ is the weighted molar mass of CdZnTe (CZT):

$$\langle \mathrm{m}_{\mathrm{CZT}} \rangle = \sum_{\mathrm{el=Cd,Zn,Te}} \eta_{\mathrm{el}} \langle \mathrm{m}_{\mathrm{el}} \rangle = 234.5\,\mathrm{g\,mol}^{-1}. \tag{5.2.14}$$

The factor η_{el} represents the composition of elements in $\mathrm{Cd_{0.9}Zn_{0.1}Te}$:

$$\eta_{\mathrm{Te}} = 1,\ \eta_{\mathrm{Cd}} = 0.9,\ \eta_{\mathrm{Zn}} = 0.1 \tag{5.2.15}$$

with their molar masses $\mathrm{m_{el}}$

$$\mathrm{m_{Cd}} = 112.41\,\mathrm{g\,mol}^{-1},\ \mathrm{m_{Zn}} = 65.39\,\mathrm{g\,mol}^{-1},\ \mathrm{m_{Te}} = 127.6\,\mathrm{g\,mol}^{-1}. \tag{5.2.16}$$

The χ^2 function obtained above can also be expressed as a function of the inverse half life $\chi^2\left((T_{1/2})^{-1}\right)$. A joint limit of multiple spectra can then be extracted by adding the $\chi^2\left((T_{1/2})^{-1}\right)$ functions

$$\chi^2_{\text{sum}}\left((T_{1/2})^{-1}\right) = \sum_i \chi^2_i\left((T_{1/2})^{-1}\right) \tag{5.2.17}$$

and taking the half life which has an increased χ^2 by 1.64 with respect to its minimum to get a 90 % C.L. limit.
The measured limit on the half life of a certain decay increases linearly with the measurement time for a background free experiment. However, if background is present, then the relation is

$$T_{1/2} \propto a\epsilon\sqrt{\frac{M \cdot t}{\Delta E \cdot B}} \tag{5.2.18}$$

with the abundance a of the isotope under study, the efficiency ϵ to detect the event, the mass M of the detector, the measuring time t, the background level B and the energy resolution ΔE. This square root dependence on the measuring time comes from the fluctuations of the background which is also growing linearly with time so that a peak has to be larger than the statistical fluctuation of the background.

5.3 Background Reduction

Several techniques can be used to reduce background. One way is to reduce the amount of potentially contaminated material or to replace it with cleaner alternatives. Another solution is to increase the efficiency of the shielding system as described in section 2.4.
Yet another method is to find a way to distinguish between signal and background events. This can be done, e.g. by measuring the pulse shape of the recorded signals and discriminating signal from background according to the pulse shapes. However, this requires special hardware, so-called flash ADCs which were not available to the COBRA experiment so far. Another more simple but less effective method can be used. Some sorts of background are produced in cascades. By analysing the timing and energies of subsequent events, events can be identified as background and then be rejected from the data set.
The last resort is to subtract the contribution of known background from the measured spectra. This can be done by locating radioactive isotopes in materials surrounding the detector and subtracting a spectrum as predicted by simulations.

5.3.1 Shielding Efficiency

The overall performance of the COBRA shielding is illustrated in figure 5.9. Here, background spectra for the CPG2 detector and the Prototype are shown taken with different shieldings and in different locations: on the earth surface and underground in the LNGS.
The green histogram shows the spectrum taken with the CPG2 detector in Dortmund outside its shield and veto system, the blue histogram shows the data of the Prototype in the LNGS outside the shielding, the red histogram represents the data taken with the CPG2 detector in

Dortmund inside the full shielding and veto system. Finally, the black histogram shows the data of the Pertinax Prototype in the LNGS inside the lead and paraffin shield.
Comparing the green and blue histograms, the contribution of the cosmic rays above 3 MeV becomes apparent as it is only visible for the measurement on the earth's surface outside a passive shielding and muon veto. A massive amount of background activity up to 2.6 MeV remains, coming from the natural decay chains, whose isotopes are omnipresent, e.g. in the surrounding rock and concrete. This component can be effectively shielded with a passive lead and copper shield as shown by the red and black spectra. The black spectrum shows another improvement in the background as the background from the natural decay chains could be further improved by separating the preamplifier electronics from the detectors and placing them in a clean copper casing. The remaining contribution is mainly due to alpha and beta contamination from the passivation paint [Wil05].

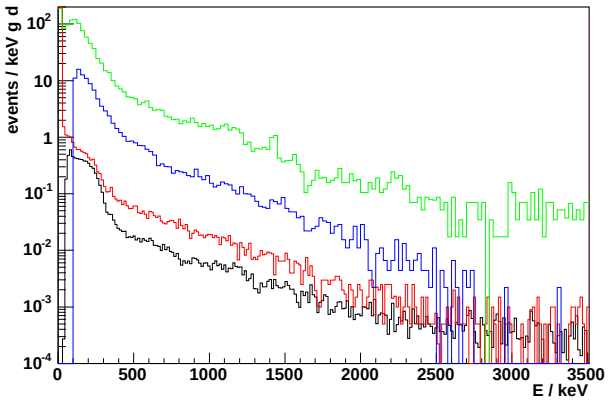

Figure 5.9: Comparison of background levels with different shieldings. The histograms show the Prototype in the complete shield in the LNGS (black, 863.2 g · d), the CPG2 detector in a lead shield in the LNGS (red, 134.5 g · d), the Prototype outside the shielding in the LNGS (blue, 4.25 g · d) and the CPG2 detector outside the shielding and active veto system on the earth surface in Dortmund (green, 2.3 g · d).

By comparing the spectra from the shielded CPG2 detector in Dortmund with the Prototype in the shielding in the LNGS, a good agreement on the data can be seen for the ^{113}Cd beta spectrum below 300 keV considering the increased background in the CPG2 detector between 500 and 2000 keV. The improvement on the background is mainly due to the electronics components being removed from the vicinity of the detectors and a better choice of clean materials for the casing and mounting of the detectors.

5.3.2 Clean Materials

In figure 5.10 the improvement of background with the new Delrin holder compared to the old Pertinax holder is shown. The new data only comprises a short measurement period compared to the data taken with the Pertinax holder. However, a significant improvement can be seen above the endpoint of ^{113}Cd and 2 MeV. The $2\nu\beta\beta$ region of ^{116}Cd at 2.8 MeV is not yet resolved sufficiently to make a decision whether an improvement can be expected or not. It is, however, evident that the remaining background comes from the passivation paint as already shown in figure 5.9.

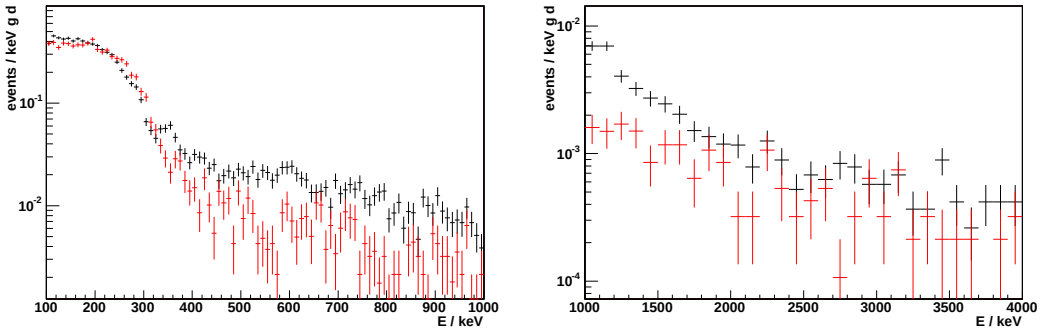

Figure 5.10: The data of a first 386.6 h measurement with the new Delrin holder shown in red is compared to the data using the Pertinax holder shown in black. The ^{113}Cd spectrum fits well to the old and new data. Above the endpoint, an improvement in background reduction of a factor 3 can be seen which vanishes above 2.6 MeV where the alphas and betas from the passivation paint dominate the spectrum.

5.3.3 Cascades

The natural decay chains of ^{238}U, ^{232}Th and ^{235}U as depicted in figure A.1 show several consecutive decays, where the half life of the second decay is well below 1 s. As the mean event rate for a single detector is in the order of one decay per few minutes, the probability that another unrelated event lies between these two decays is low.

In the ^{238}U decay chain the beta decay of ^{214}Bi is followed by an alpha decay of the daughter nucleus ^{214}Po with a half life of $164\ \mu$s and an energy of 7.687 MeV. If the decay is located near the detector, e.g. in the passivation paint or in the detector itself, the alpha can be identified by its whole energy. By analysing the time of arrival and energy of the event before the triggering event which must lie in an energy window around the alpha energy, the preceding decay can be identified.

Other candidates are the ^{220}Rn decay with a 6.288 MeV alpha followed by the 6.778 MeV alpha of the decay of ^{216}Po with a half life of 145 ms, or the beta decay of ^{211}Bi with a Q-value of 579 keV followed by an alpha decay of the daughter isotope ^{211}Po with an energy of 7.594 MeV and a half life of 0.52 s.

For the ^{220}Rn alpha decay candidate events are shown in table 5.4. The whole data set taken with the CAMAC DAQ has been scanned for events with an energy of (6288 ± 200) keV. If the next event in the same detector follows within 10 s, which corresponds to about 70 half lives of the daughter nucleus ^{216}Po, this double event has been selected as a candidate. Two candidate events show the correct second energy of approximately 6.8 MeV. Two more double events show a too low energetic second event which might be due to absorption effects. The other three events can clearly not be attributed to this cascade because their energy being recorded in the overflow bin of the ADC is much too high. Another note has to be taken that those cascades are not seen for detectors D3 and D4 because their ADC is not buffered.

Period	Detector	Energy 1 / keV	Δt	Energy 2 / keV
2003_09_23	D2	6221.74	0.1674	4136.27
"	D2	6289.66	0.2371	6845.38
2004_05_05	D2	6487.66	0.0311	6816.31
2004_05_27	D1	6485.7	0.0427	4832.45
2004_07_14	D1	6261.31	0.0028	15668.7
"	D1	6154.82	0.0027	15668.7
"	D1	6196.66	0.0028	15668.7

Table 5.4: All events with an energy of (6288 ± 200) keV are shown which have a subsequent event within 10 s. The first event is assumed to be from the decay of ^{220}Rn with a 6.228 MeV alpha. With a half life of 145 ms the daughter nucleus ^{216}Po should again emit an alpha with an energy of 6.778 MeV. Two events are candidates for this cascade with an energy of approximately 6.8 MeV. Two more are too low energetic which might be due to absorption effects. The other three events are clearly not attributed to this cascade with an energy recorded in the overflow bin of the ADC. No such cascades are seen for detectors D3 and D4.

The detected candidate events of the ^{214}Bi-^{214}Po cascade for ADC 2 are shown in the left diagram in figure 5.11. The signature is an event with an energy of (7.687 ± 0.2) MeV and a preceding event less than 1 s before that event. All six events are recorded with $\Delta t \simeq 2$ ms, i.e. the minimal time between two readouts of the CAMAC ADC, which is to be expected because of the low half life of this cascade of 164 μs. Therefore, also no cascades were seen for the unbuffered ADCs 3 and 4. For ADC 1 the threshold of about 600 keV was too high to see beta events. Other events may have been rejected by the de-tailing procedure as described in section 3.2.

The right diagram in figure 5.11 shows the 16 candidate events of the ^{211}Bi-^{211}Po cascade which has a half life of 0.52 s. For this cascade candidate events have been seen in all detectors. However, some ambiguity remains as with the current energy resolution the alpha energy has an overlap with the above 7.687 MeV alpha from the ^{214}Bi-^{214}Po cascade.

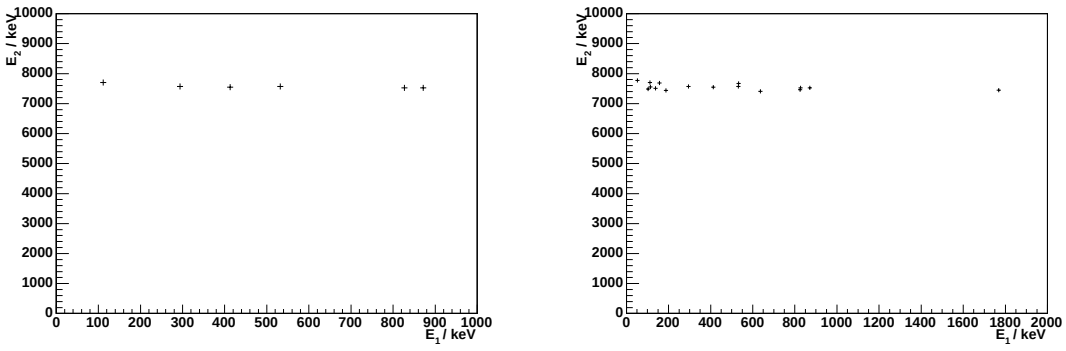

Figure 5.11: The left diagram shows the recorded candidate events of the ^{214}Bi-^{214}Po cascade with E_1 the energy of the beta decay and E_2 the energy of the alpha (7.687$\pm$0.2) MeV. The recorded candidate events of the ^{211}Bi-^{211}Po cascade are shown in the right diagram with E_1 the energy of the beta decay and E_2 the energy of the alpha (7.594$\pm$0.2) MeV.

5.3.4 Alpha decays

If a data set shows a signal of alpha contamination, then the background source must be located close to the detector. Candidates for the Prototype setup are the detector material itself and the passivation paint covering the detectors. As the activity of the passivation paint has been measured with a germanium counter this background component can be simulated and compared to the data. With this measurement the contribution of the associated gammas in the same decay chain as the alpha decays can be estimated as well by simulating the corresponding gamma activity.

A list of energies of all alpha particles with an emission probability >0.1 % from the ^{232}Th and ^{238}U decay chains is shown in table 5.5.

^{232}Th-Chain			^{238}U-Chain		
E_α / MeV	Prob. / %	Mother Isotope	E_α / MeV	Prob. / %	Mother Isotope
4.012	77.9	^{232}Th	4.197	77	^{238}U
3.954	22.1	^{232}Th	4.147	23	^{238}U
5.423	71.1	^{228}Th	4.775	72.5	^{234}U
5.340	28.2	^{228}Th	4.723	27.5	^{234}U
5.221	0.44	^{228}Th	4.688	76.3	^{230}Th
5.685	94.9	^{224}Ra	4.621	23.4	^{230}Th
5.449	5.1	^{224}Ra	4.784	94.5	^{226}Ra
6.288	99.9	^{220}Rn	4.601	5.55	^{226}Ra
5.747	0.11	^{220}Rn	5.490	99.9	^{222}Rn
6.778	100	^{216}Po	4.987	0.98	^{222}Rn
6.089	27.1	^{212}Bi	6.002	100	^{218}Po
6.050	69.6	^{212}Bi	7.687	100	^{214}Po
8.785	100	^{212}Po	5.305	99.9	^{210}Po

Table 5.5: Alpha energies and emission probabilities for the two natural decay chains ^{232}Th and ^{238}U (taken from [Wah96]).

Using the geometry of the Prototype as described in section 4.3.2 the measured material activities given in appendix C [Lau04] have been simulated and compared to the high energy cut data. Figure 5.12 shows the simulation folded with the detector's energy resolution and the measured data of detector D4. The left diagram shows only the contamination of the passivation paint broken down in the single components ^{40}K, ^{60}Co, ^{137}Cs and the betas and alphas from the decay chains ^{238}U and ^{232}Th. The summed simulated spectrum matches the data well above 4 MeV which is a proof of the paint being the limiting factor. The right diagram shows the additional background from the Pertinax holder which mostly contributes up to 2 MeV.

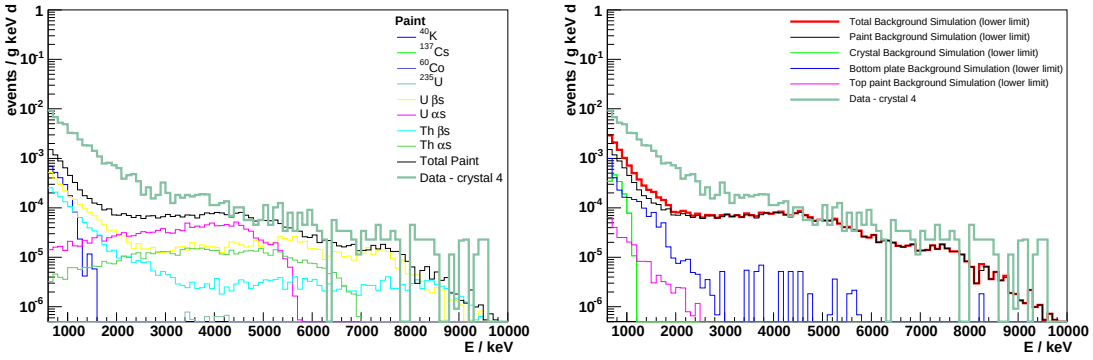

Figure 5.12: The background contribution as simulated by [Wil05] is shown for the components of the paint in the left diagram and for the complete Prototype simulation in the right diagram. The data is shown exemplarily for detector D4 using the high energy data set. The simulated events have been folded with the energy resolution of the detector. Above 4 MeV the contribution of the paint is sufficient to account for the observed count rate in this detector.

For the activity of the detector material only upper limits could be measured by [Lau04]. However, this activity can be measured with the detectors themselves as well. As shown in figure 5.13 the spectral shape of an alpha source in the paint does not result in a Gaussian shaped peak, but a broad distribution. The spectral shape of alphas emitted in the detector is a peak like structure as the alpha cannot leave the crystal. Therefore, if peaks are found in the data spectrum, these events must originate from intrinsic contamination of the detector material.

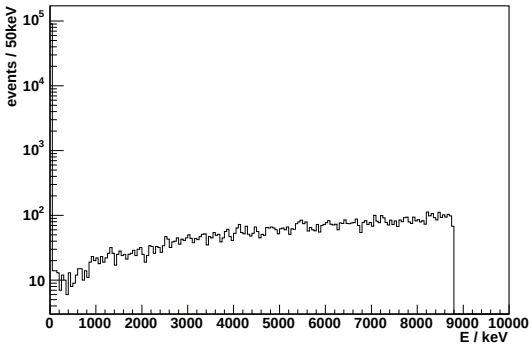

Figure 5.13: Simulation of 10^5 alpha particles with an energy of 8.8 MeV emitted isotropically and homogeneously in a 50 μm layer of passivation paint. No energy resolution has been folded in.

In figure 5.14 the agglomeration of events above 4 MeV is attributed to peak like structures. Taking the alpha energies from table 5.5 and applying the corresponding energy resolution on the peaks, the number of events in the peaks can be fitted to the data. This procedure has been done manually as the total number of events is low and a slight displacement can be seen for D2 and D4. This is a hint to an inaccurate extrapolation of the calibration. However, for the $0\nu\beta\beta$ analyses of 2.805 MeV the calibration is expected to be sufficient.

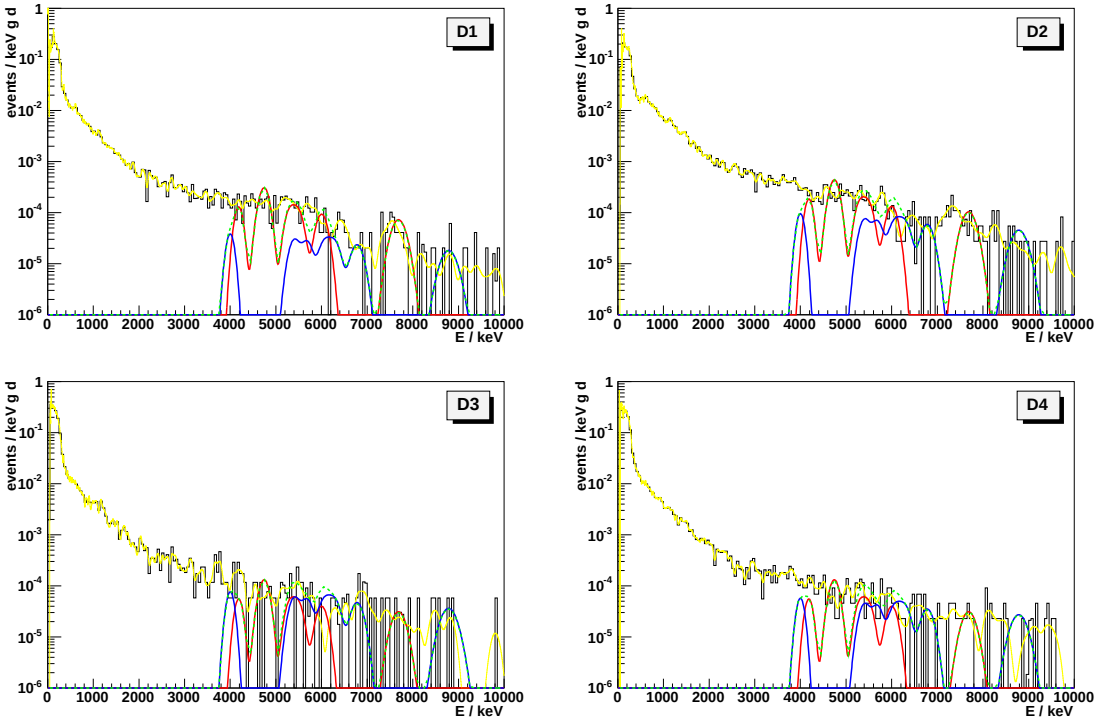

Figure 5.14: The data of detectors D1−D4 are shown as a black histogram. A spectrum of the alphas from the ^{238}U and ^{232}Th decay chains is superimposed in red and blue respectively. The emission probabilities are taken from table 5.5 and are adjusted by hand to a total height which matches the peak content in the data spectrum. The data spectrum has been smoothed for better visibility as indicated by the yellow histogram. The sum of ^{238}U and ^{232}Th is shown as a dashed green line. For D2 and D4 a displacement of the theoretical alpha peaks to the measured data is visible. This hints to an insufficient calibration for high energies above 5 MeV.

Using the number of event candidates from the manual fit and a 100 % detection efficiency for alphas inside the crystal, the specific activity of the crystal material can be calculated. The results are shown in table 5.6. These values are, of course, only a first approximation and need to be verified with larger statistics.

Sample	^{238}U / mBq kg^{-1}	^{232}Th / mBq kg^{-1}
D1	$\leq$0.810	$\leq$0.231
D2	$\leq$1.16	$\leq$0.579
D3	$\leq$0.347	$\leq$0.463
D4	$\leq$0.347	$\leq$0.347
Cd, Zn, Te	<19	<19
CdZnTe	<51	<60

Table 5.6: The intrinsic contamination of the detectors is shown for the four detectors of the Prototype D1−D4. For comparison the activity of the detector material CdZnTe and its components Cd, Zn and Te measured with a germanium detector by [Lau04] is given. The significance for the latter activities of the detector material and elemental material samples is limited by the measurement time.

5.3.5 Characteristic Gamma Lines

The contribution of characteristic gamma lines to the total background can be extracted from the data as well. As already mentioned, the 351.9 keV and 609.3 keV gamma lines are clearly visible in the spectrum. These lines can be used to estimate the activity of construction materials and cross check them with the measurements already described in section 2.6. However, as gammas are penetrating their origin is not easily accessible.
Using the χ^2 method described in section 5.2.1, the number of events from the 1460 keV gamma line of the decay of ^{40}K can be extracted from the high energy data set. The best fit of the gamma line is consistent with the null hypothesis. Using the number of excluded events at a 90 % C.L. and the assumption that all contamination is located in the CdZnTe crystals, a resulting activity of $\leq$0.5 Bq / kg can be derived. This result puts an almost comparable limit on the contamination of the detectors with ^{40}K than the measurement obtained with the germanium detector of ≤ 0.26 Bq/kg described in appendix C.
The same analysis for the 609.3 keV gamma line yields a ^{238}U activity of 106.9 mBq/kg for D1, 51.38 mBq/kg for D3 and 51.00 mBq/kg for D4. As these values contradict the activities measured from the alpha contamination by more than two orders of magnitude, this background must be located outside the crystals.

5.3.6 Final Spectrum

In the previous sections techniques to identify background events have been presented. However, as the efficiency to identify these events as background is only marginal for the current setup using the CAMAC DAQ, the spectrum shown in figure 5.8 is used as the final spectrum for the analyses. Nevertheless, these techniques will play a crucial role in the analysis of the data from the $4\times4\times4$ array.
For the search for the neutrino-less double beta decay, the two isotopes ^{116}Cd and ^{120}Te are the most promising candidates due to their high Q-value and nuclear matrix as shown in table 1.1. The background level of the four detectors of the Prototype for interesting regions, i.e. the endpoint of the double beta decays of ^{116}Cd, ^{130}Te and ^{70}Zn is shown in table 5.7.

	Background Level in 10^{-4} events / keV g d				
Range	Detector 1	Detector 2	Detector 3	Detector 4	Sum Spectrum
2.5-3.0 MeV	5.28 ± 0.35	5.03 ± 0.42	1.90 ± 0.49	2.83 ± 0.25	5.04 ± 0.20
2.4-2.6 MeV	6.48 ± 0.61	5.50 ± 0.70	2.21 ± 0.83	3.40 ± 0.44	5.89 ± 0.34
2.7-2.9 MeV	5.59 ± 0.56	4.33 ± 0.62	2.17 ± 0.82	2.22 ± 0.35	4.79 ± 0.30
0.9-1.1 MeV	61.06 ± 1.86	51.27 ± 2.13	25.43 ± 2.81	52.13 ± 1.72	63.50 ± 1.10

Table 5.7: The background rates corrected for the relative detection efficiency as described in section 4.4 are shown in 10^{-4} events per keV, gram and day. The selected regions correspond to the $0\nu\beta\beta$ regions of ^{116}Cd (2.805 MeV), ^{130}Te (2.529 MeV) and ^{70}Zn (1.001 MeV).

As shown in figure 5.12, the limiting factor dominating the background up to about 8 MeV comes from the passivation paint. Recent measurements with the new Delrin holder indicate that this is indeed the current limit of the setup. Unfortunately, the 64 detector array described in section 2.7 will be using detectors with the passivation paint as no alternative is yet known, thus the half life limits obtained with this setup will only increase with the square root of the statistics as shown in equation 5.2.18.

5.4 The 4-fold forbidden non-unique β spectrum of ^{113}Cd

Beta decays are usually classified according to their spin and parity changes. The larger the spin change of the transition the longer is its half life. In order to compare different decays, the rate of the decay can be better expressed by an ft value, which includes the half life t as well as a phase space correction

$$f = \int_{m_e}^{Q} pE(Q-E)^2 F(Z,E) S(E) dE \tag{5.4.19}$$

with the spectral shape $S(E)$, the Fermi function $F(Z,E)$ [Pov95]

$$F(Z,E) \simeq \frac{2\pi\eta}{1-e^{-2\pi\eta}} \quad \text{with } \eta = \frac{Z\alpha}{\beta} \tag{5.4.20}$$

and the beta factor $\beta(E) = p(E)/(E+m_e)$.
The ft value strongly depends on the degree of forbiddenness. An overview of the classification of beta decays is shown in table 5.8.

Transition	ΔI	$\Delta\pi$	log ft
superallowed	$0, \pm 1$	0	3.5 ± 0.2
allowed	$0, \pm 1$	0	5.7 ± 1.1
forbidden	$0, \pm 1$	± 1	7.5 ± 1.5
forbidden unique	± 2	± 1	8.5 ± 0.7
twice forbidden	± 2	0	12.1 ± 1.0
twice forbidden unique	± 3	0	11.7 ± 0.9
3-fold forbidden	± 3	± 1	18.2 ± 0.6
3-fold forbidden unique	± 4	± 1	20.7 (^{40}K)
4-fold forbidden	± 4	0	23.2 (^{113}Cd), 22.5 (^{115}In), 23.5 (^{50}V EC), 24.3 (^{50}V β^-)

Table 5.8: The scheme of the order of beta decays with their classification, the selection rules (ΔI, $\Delta\pi$) [Kon66] and log ft is shown [Sin98]. All three isotopes known to be instable to 4-fold forbidden non-unique beta decay are listed with their respective log ft values.

Only three isotopes are known to be instable to 4-fold forbidden beta decay, namely ^{50}V, ^{113}Cd and ^{115}In. Their half lives are about 10^{15} years. For ^{50}V, the β spectrum has never been measured, for ^{115}In there are two recent measurements [Pfe79, Bar04] and two measurements in the 1960's [Bea61, Wat62] and for ^{113}Cd five previous measurements exist [Wat62, Gre70, Mit88, Ale94, Dan96a].
^{113}Cd is of special interest for the COBRA experiment as it is naturally occurring with an abundance of 12.22 % [Wah96]. Its decay to ^{113}In is a $1/2^+ \rightarrow 9/2^+$ transition with a log ft value of 23.2 [Sin98]. After an unsuccessful attempt to measure the half life of ^{113}Cd in 1962 [Wat62], the first half life determination of its decay was achieved in 1970, comparing the count rates of an enriched sample of ^{113}Cd with a natural "blank". This experiment resulted in a half life of $(9.3 \pm 1.9) \cdot 10^{15}$ a [Gre70]. An early approach in the late 1980s using CdTe

semiconductor detectors extracted a half life of $(4-12)\cdot 10^{15}$ a [Mit88]. Other attempts have been done in the 1990s using $CdWO_4$. The first experiment used the material as a scintillator and measured a half life of $T_{1/2} = (7.7 \pm 0.3)\cdot 10^{15}$ a [Dan96a]. Using $CdWO_4$ as a cryogenic bolometer resulted in $T_{1/2} = (9.0 \pm 0.5(\mathrm{stat.}) \pm 1(\mathrm{syst.}))\cdot 10^{15}$ a [Ale94]. The experiments mentioned above are listed in table 5.9.

Year	Reference	Detector	Half Life / 10^{15} a
1961	[Wat62]	CdO powder on Geiger counters	$> 1.3 \pm 1.9$
1970	[Gre70]	counter, enriched vs. natural Cd	9.3 ± 1.9
1988	[Mit88]	CdTe semiconductor	$4-12$
1994	[Ale94]	$CdWO_4$ cryogenic bolometers	$9.0 \pm 0.5(\mathrm{stat.}) \pm 1(\mathrm{syst.})$
1996	[Dan96a]	$CdWO_4$ scintillators	7.7 ± 0.3

Table 5.9: Past experiments measuring the 4-fold forbidden non unique beta decay of ^{113}Cd.

Using the given half lives the decay rate leads to about 350 events per day in a 1 cm^3 CdZnTe detector with a mass of 6.5 g. With a Q-value of (320±3) keV [Aud95] this decay forms the most important background for other searches in the low energy region. This rate has to be compared to a total activity of currently about 100 events per day for the total spectrum above the end point of ^{113}Cd.
The shape of a beta spectrum as a function of the electron energy is theoretically described as

$$N(E) = F(Z,E)\cdot p\cdot (E+\mathrm{m}_e)\cdot (Q-E)^2\cdot S(E). \tag{5.4.21}$$

The Fermi function $F(Z,E)$ is taken from equation 5.4.20. The spectral shape $S(E)$, however, cannot be predicted from theory for the 4-fold non unique beta decay of ^{113}Cd. The common approach is that S can be modelled by a polynomial of the order $(2\triangle I - 2)$ in p and q, the momenta of the electron and neutrino respectively. Thus, we use the approach from [Dan96a] modelling the spectral shape with a polynomial of 6^{th} order.

$$S(E) = p(E)^6 + 7\cdot c_1\cdot p(E)^4\cdot q(E)^2 + 7\cdot c_2\cdot p(E)^2\cdot q(E)^4 + c_3\cdot q(E)^6 \tag{5.4.22}$$

The electron momentum $p(E)$ is given by

$$p(E) = \left((E+m_e)^2 - m_e^2\right)^{1/2} \tag{5.4.23}$$

and the neutrino momentum $q(E)$ by

$$q(E) = (Q-E) \tag{5.4.24}$$

In order to describe the measured data, the energy resolution of the apparatus $R(E,E')$ has to be folded into the spectrum

$$N'(E) = \int R(E,E')N(E)dE' \tag{5.4.25}$$

The energy resolution is a Gaussian distribution with a width according to the energy values stated in equations 5.1.3−5.1.6 for each detector.

The coefficients of the spectral shape are taken from [Dan96a]

$$\begin{aligned} c_1 &= 1.01 \pm 0.01 \\ c_2 &= 1.48 \pm 0.05 \\ c_3 &= 0.68 \pm 0.21. \end{aligned} \tag{5.4.26}$$

Another set of coefficients has been measured by [Ale94]

$$\begin{aligned} c_1 &= 0.765 \pm 0.095 \\ c_2 &= 0.589 \pm 0.177 \\ c_3 &= 2.04 \pm 0.74. \end{aligned} \tag{5.4.27}$$

However, the coefficients have only little impact on the shape of the spectrum above 200 keV. The largest difference is seen well below 100 keV. For comparison the two spectral shapes are shown in figure 5.15. Additionally, the beta spectrum as suggested by [Chu99] is shown as well as the spectral shape measured for the 4-fold forbidden decay of ^{115}In [Bar04]. The latter spectrum was adjusted to an endpoint of 320 keV and is shown because the beta decay of ^{115}In has the same selection rules as ^{113}Cd.

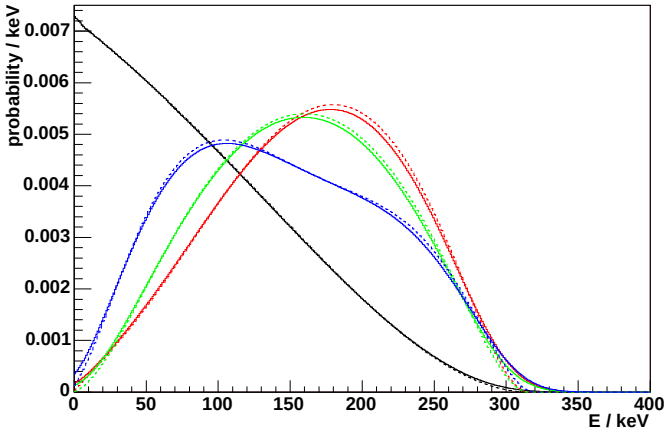

Figure 5.15: Theoretical spectra of the beta decay of ^{113}Cd. The spectra shown are from [Ale94] (red), [Dan96a] (green), Q-value-adjusted ^{115}In [Pan05] (blue) and Table of Isotopes (black) [Chu99, Aud95]. The dashed line shows the theoretical spectrum and the solid line the same spectrum folded with the energy resolution of the detectors.

For the analysis of the ^{113}Cd spectrum, the low energy data set as defined in section 5.1.2 is used. Before fitting the spectral shape according to the coefficients given in equation 5.4.26, background is subtracted from the data according to

$$B(E) = B_1 \exp(-E/B_2) \tag{5.4.28}$$

where the exponential function is intended to model the background from radioactive sources. The exponential function is fitted to the data from 400 keV to 1 MeV for each of the three detectors as shown in figure 5.16. The estimated background is then subtracted from the data. The contribution of the number of fitted background events to the full data is about 12.6 % for the energy range 120−310 keV.

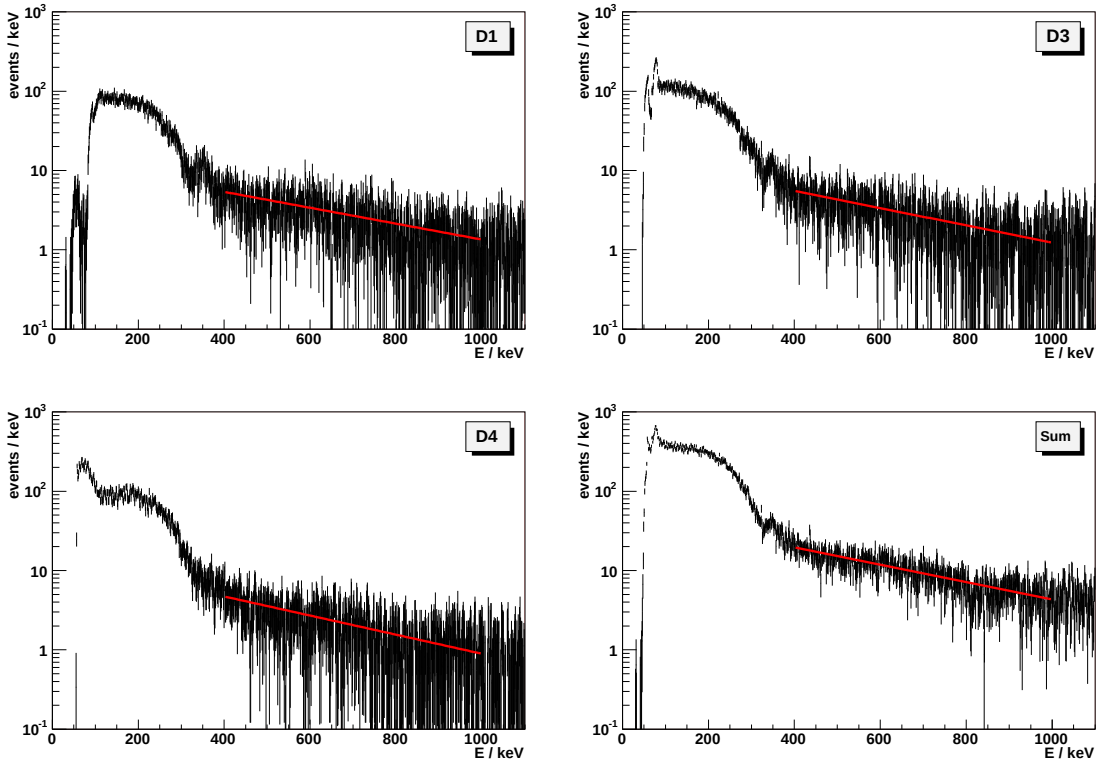

Figure 5.16: The background fit of detectors D1, D3, D4 and their summed spectrum is shown in red for the exponential background from 400−1000 keV. The background coefficients are $B_1 = 13.55$, $B_2 = 432.8$ for D1, $B_1 = 15.07$, $B_2 = 399.2$ for D3, $B_1 = 14.29$, $B_2 = 360.5$ for D4 and $B_1 = 53.50$, $B_2 = 396.9$ for the summed spectrum.

After the subtraction of the exponential background component, the contribution of the 351.9 keV gamma line from the ^{238}U decay chain is estimated by counting the number of events from 320−380 keV for each detector. The photo peak and Compton continuum of this peak is then removed by subtracting the corresponding number of events with the spectral shape as obtained with a simulation of the 351.9 keV gamma line folded with the detector's energy resolution.

After background reduction, the beta spectrum from [Dan96a] folded with the energy resolution of the detectors has been fitted to the individual detector spectra from 120−310 keV considering the relative efficiency of each detector as described in section 4.4. The fitted spectra for detectors D1, D3 and D4 are shown in figure 5.17 as yellow, red and green lines over the corresponding data histograms. The fit to the summed data is shown as a blue line. The spectral shape from [Dan96a] has been chosen, because the energy resolution of the $CdWO_4$ scintillators is about 10 %, which is comparable to the energy resolution of the detectors used for this analysis.

In table 5.10 the fitted event rates per hour and the resulting half lives are shown. The errors on the fitted values are statistical errors with a confidence interval of 90 %. The event rate has been calculated for the summed spectrum of all three detectors as well.

Detector	Events / h	$T_{1/2}$ / 10^{15} a	χ^2 / ndf
D1	16.3±0.4	8.1 ± 0.2	117.2/169=0.693
D3	17.6±0.5	7.5 ± 0.3	160.4/169=0.949
D4	13.9±0.5	9.3 ± 0.4	318.1/169=1.882
$\sum$(D1,D3,D4)	16.0±0.4	8.2 ± 0.2	234.0/169=1.385

Table 5.10: The fitted event rates and half lives of the ^{113}Cd beta decay are shown for the three detectors of the low energy data set and their sum spectrum. The goodness of the fit is indicated by the reduced χ^2 values of about unity.

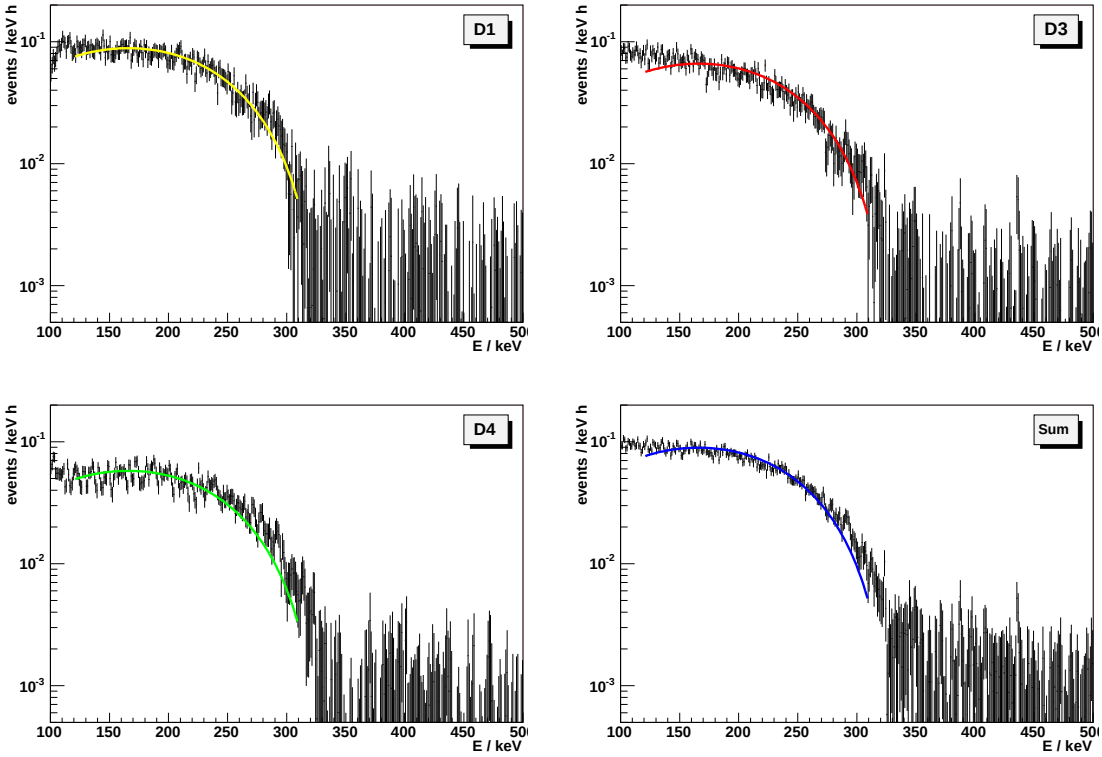

Figure 5.17: The fit of the ^{113}Cd beta spectrum according to [Dan96a] is shown for detectors D1 (yellow), D3 (red) and D4 (green) as well as for the summed data spectrum (blue).

The systematic error of the half life has been investigated by varying the range of the background and signal fits as well as the folded energy resolution. All these variations lead to a change of the half life of less than 1 %. The uncertainty of the amount of cadmium in the crystals because of the variation of the zinc content from 7−11 % leads to an error of 1.8 % in the amount of ^{113}Cd and therefore the measured half life. The largest unknown systematic error stems from the yet unknown active volume of the detectors. The contribution of this uncertainty may well contribute as much as 10 % to the systematic error but current investigations [Ful05] suggest that this contribution is indeed smaller. To be conservative the 10 % error is used, however, only as a single sided error as this uncertainty may only lower the half life.
Another problem is the low mobility of the holes which still has an impact on the detector signal. Though almost eliminated by the CPG readout, the measured pulse height of an energy

deposition in the detectors depends on the position of the event in the crystal. This top-bottom asymmetry is also discussed in section 4.4.
The value of the half life of the 4-fold forbidden beta decay of ^{113}Cd can be calculated as

$$T_{1/2} = \left(8.2 \pm 0.2(\mathrm{stat.})^{+0.2}_{-1.0}(\mathrm{syst.})\right) \cdot 10^{15}\,\mathrm{a}. \tag{5.4.29}$$

This has to be compared to the measured values of $T_{1/2} = (7.7 \pm 0.3) \cdot 10^{15}$ a [Dan96a] and $T_{1/2} = (9.0 \pm 0.5(\mathrm{stat.}) \pm 1(\mathrm{syst.})) \cdot 10^{15}$ a [Ale94]. The obtained half life is in good agreement with both measurements.
Though this analysis does not decide on the spectral shape as given by [Dan96a] and [Ale94], with this data the shape of the ^{113}Cd beta spectrum as given by the Table of Isotopes [Chu99] can be excluded.
In figure 5.18 the summed spectrum of the low energy data set is compared to the spectral shape suggested by [Chu99, Aud95] for the beta decay of ^{113}Cd. The predicted spectrum has been folded with the mean energy resolution of the detectors and scaled to the same number of events in the energy interval 100−300 keV. As already visible by the unguided eye the predicted spectrum does not fit the data. This is underlined by a reduced χ^2 of 24.6 which is far-off the optimal value of 1.

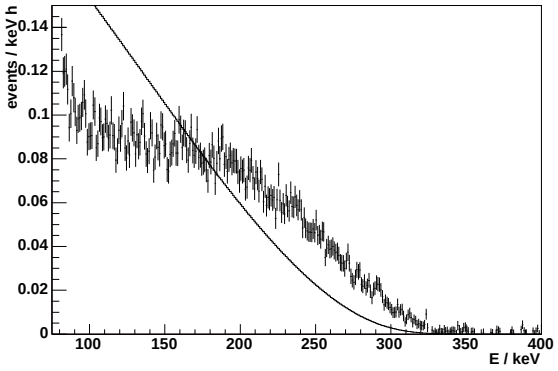

Figure 5.18: Comparison of COBRA data with the "Table of Isotopes" (ToI) spectrum of the beta decay of ^{113}Cd [Chu99, Aud95]. The ToI spectrum is folded with the mean energy resolution and normalised to the same number of events in the interval 100−300 keV as the summed data spectrum. The inadequacy of this model is indicated by a $\chi^2/\mathrm{ndf} = 4885.7/199 = 24.6$.

With the increased number of detectors in the 64 array, a statistically more significant result for the half life will be available derived from 64 independent measurements. The study of the new detectors and their active volume will also contribute to a decreased systematic error. Finally, the shape of the spectrum can be measured more accurately, extracting the coefficients of the spectral shape polynomial $S(E)$ if the noise and ADC thresholds can be lowered further.

5.5 The $2\nu\beta^-\beta^-$ Spectra

As introduced in section 1 the sum energy spectrum of the electrons in $2\nu\beta\beta$ decay is of continuous form because the neutrinos carry away energy. This spread of the events over a broad energy range makes it difficult to identify these events as signal events. There have been many previous measurements of the half life of this decay, some of them can be found in [Geo95, Nor87, Dan00, Dan03].
The distribution of the sum of electron energies according to equation 1.2.18 is compared to the high and low energy data sets described in section 5.1.2 for different decays depending on their Q-value. The energy resolution and detector acceptance have not been folded on the theoretical spectra since this is only a minor effect on the overall spectrum as already seen for the ^{113}Cd spectrum in figure 5.15.
Using the previously measured half life of ^{116}Cd of $T_{1/2} = 2.9^{+0.4}_{-0.3} \cdot 10^{19}$ a from [Dan03] the number of events to be seen in the COBRA detector can be derived. In figure 5.19 the data spectrum of the Prototype is shown as a histogram with the underlying double beta spectrum indicated by a thick line. The thinner lines mark the contribution of the double beta spectrum if its half life was $2.9 \cdot 10^{18}$ a and $2.9 \cdot 10^{17}$ a. The dashed line illustrates the current sensitivity limit from the COBRA data of $T_{1/2} > 1 \cdot 10^{17}$ a extracted by lowering the half life, thus increasing the number of events in the spectrum, until the theoretical spectrum and data reach the same level of activity over a larger range. Note that the present limit is dominated by the background. Using simulations of the setup and inserting the activities of the used materials, a combined fit of the simulated background and the $2\nu\beta^-\beta^-$ spectral shape may lead to an increased sensitivity.

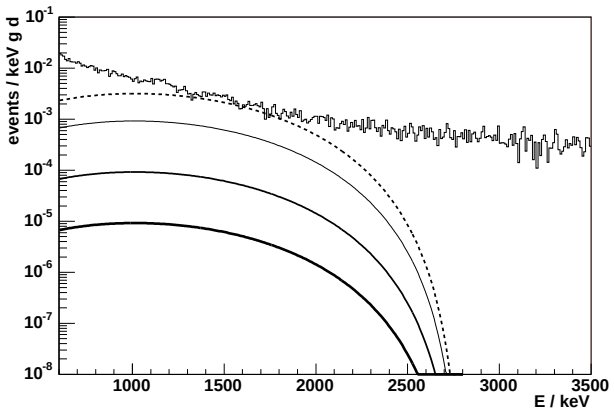

Figure 5.19: The theoretical spectrum of the $2\nu\beta^-\beta^-$ decay of ^{116}Cd [Tre95] is plotted against the high energy data set of 2.6 kg d statistics. The lowest line corresponds to $T_{1/2} = 2.9 \cdot 10^{19}$ a [Dan03]. The lines above show how the spectrum would grow if the half life was decreased by a factor 10 and 100. The dashed line indicates the current sensitivity of the COBRA measurement of $T_{1/2} > 1 \cdot 10^{17}$ a.

The same procedure can be repeated for the other $2\nu\beta^-\beta^-$ emitters in CdZnTe as well. The left diagram in figure 5.20 shows the analogue plot to figure 5.19 for ^{130}Te. This decay, however, has not yet been measured by real time detectors. The used half life value of $T_{1/2} = 10^{21}$ a has been obtained from geochemical experiments. For ^{70}Zn, ^{128}Te and ^{114}Cd the low energy data

set was used because of their lower Q-value. For the sake of clarity, only the extracted limits of the half life sensitivities are shown.

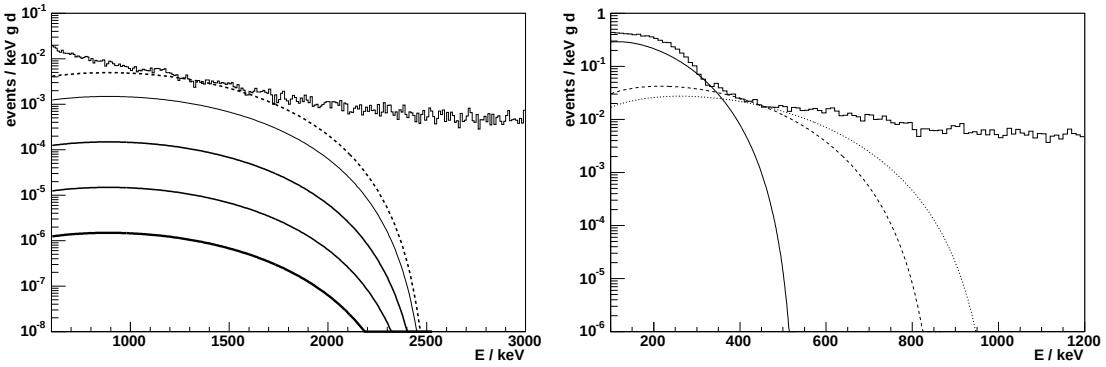

Figure 5.20: The theoretical spectrum of the $2\nu\beta^-\beta^-$ decay of ^{130}Te [Tre95] is plotted against the high energy data set of 2.6 kg d statistics in the left diagram. The lowest line corresponds to $T_{1/2} = 10^{21}$ a [Tre02] which has been deduced from geochemical experiments and has not yet been observed directly. The lines above indicate how the spectrum would grow if the half life was decreased by a factor 10, 100 and 1000. The dashed line shows the current detection limit with the COBRA measurement of $T_{1/2} > 3 \cdot 10^{17}$ a. For the $2\nu\beta^-\beta^-$ half lives of ^{70}Zn, ^{128}Te and ^{114}Cd the low energy data set of 0.86 kg d statistics is used. The limits of their half lives as extracted from the COBRA data are shown in the right diagram. The values are $T_{1/2} > 2.5 \cdot 10^{14}$ a for ^{70}Zn (dotted line), $T_{1/2} > 1.0 \cdot 10^{17}$ a for ^{128}Te (dashed line) and $T_{1/2} > 2.0 \cdot 10^{16}$ a for ^{114}Cd (solid line).

The half life sensitivities extracted above are compared to previously measured values in table 5.11. For most isotopes many measurements are known with slightly varying results. A complete list can be found in [Tre02]. With the current data the extracted limit of the half life of ^{116}Cd is only two orders of magnitude lower than the previously measured spectrum.

Isotope	COBRA Half Life Limit	Measured Value	Reference
^{70}Zn	$> 2.5 \cdot 10^{14}$ a	$> 1.3 \cdot 10^{16}$ a	[Dan04]
^{130}Te	$> 3.0 \cdot 10^{17}$ a	$(2.6 \pm 0.3) \cdot 10^{21}$ a	[Tre02]
^{128}Te	$> 1.0 \cdot 10^{17}$ a	$(7.2 \pm 0.3) \cdot 10^{24}$ a	[Tre02]
^{116}Cd	$> 1.0 \cdot 10^{17}$ a	$2.9^{+0.4}_{-0.3} \cdot 10^{19}$ a	[Dan03]
^{114}Cd	$> 2.0 \cdot 10^{16}$ a	$> 6.0 \cdot 10^{17}$ a	[Dan03]

Table 5.11: The 90 % C.L. half life limits of $2\nu\beta^-\beta^-$ instable isotopes in CdZnTe measured with the COBRA detector are compared with existing values. The referenced half lives for the Te isotopes were extracted from geochemical experiments.

As can be seen from figure 5.20, the half life of the $2\nu\beta^-\beta^-$ decay of ^{114}Cd is dominated by the background from the 4-fold forbidden non-unique beta decay of ^{113}Cd. Figure 5.21 shows the two energy distributions normalised to 1 event. The spectra differ below 100 keV which is not resolvable in the current measurement and above the end point of the ^{113}Cd spectrum, where the 351.9 keV gamma line of the ^{238}U decay chain is a limiting factor. If the background

in this region can be further reduced, a more stringent limit on the $2\nu\beta^-\beta^-$ decay of ^{114}Cd can be set. Another method to improve the sensitivity is to perform a combined fit of both spectra.

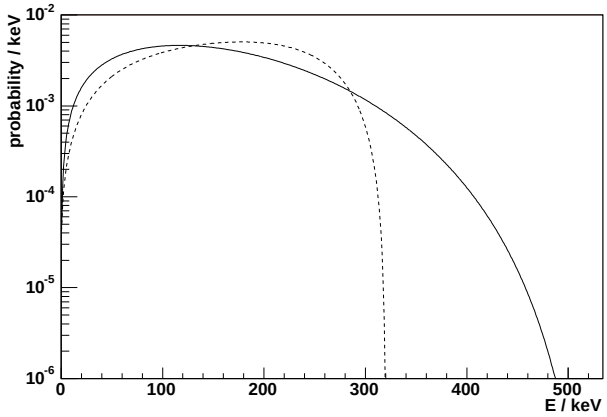

Figure 5.21: Comparison of the spectral shapes of the 4-fold forbidden non-unique beta decay of ^{113}Cd indicated by a dashed line using the parametric form of [Dan96a] and the $2\nu\beta\beta$ decay of ^{114}Cd [Tre95] drawn with a solid line. The energy resolution of the detectors has been omitted from the two distributions. A significant deviation in the form of the two spectra can be seen below 100 keV and, of course, above 320 keV, the end point of the ^{113}Cd spectrum.

5.6 The $0\nu\beta^-\beta^-$ Half Lives

Defining limits on the neutrino-less double beta decay $0\nu\beta\beta$, is easier to accomplish than $2\nu\beta\beta$, because no energy is carried away by neutrinos. Thus, the signature is a mono-energetic line instead of a broad distribution when measuring the sum electron energy. According to equations 5.2.12 and 5.2.13, the half life can be calculated from the number of detected events n as

$$T_{1/2} = \frac{m \cdot t}{[\mathrm{g} \cdot \mathrm{d}]} \cdot \frac{\epsilon\, a\, \eta}{n} \cdot 4.877 \cdot 10^{18}\,\mathrm{a} \tag{5.6.30}$$

The χ^2 method has been used to extract the upper limits of the number of events hidden in the data spectra. However, as the result of the peak search is assumed to be negative due to the known half life limits, the peak region itself has not been excluded from the background fit. A possible contribution of a peak to the background fit has been ruled out by a visual inspection of the fitted curves. An exponential shape has been used as a background model for all peak searches except for the decay of ^{130}Te and ^{116}Cd to the ground state, where a constant background is assumed due to the low event rate above 2 MeV. Then the number of excluded events has been converted to half lives for the $0\nu\beta^-\beta^-$ decays to the ground state and excited states for each detector. A joint limit of these single detector values has been extracted according to equation 5.2.17. The resulting values are listed in table 5.12.

Isotope / Level		E / keV	Half Life Limit / 10^{19} a D 1	D 2	D 3	D 4	Joint Limit
^{70}Zn	$g.s.$	1001	0.0171	0.0106	0.00200	0.0111	0.0283
^{128}Te	$g.s.$	868	3.07	2.38	1.24	3.73	4.58
$\hookrightarrow$	443 keV, 2^+	425	1.68	–	1.09	1.83	3.33
^{130}Te	$g.s.$	2529	7.70	2.53	3.85	5.56	8.13
$\hookrightarrow$	536 keV, 2^+	1993	13.0	4.45	2.27	2.25	11.3
$\hookrightarrow$	1121 keV, 2^+	1408	4.10	3.16	1.37	1.71	3.91
$\hookrightarrow$	1794 keV, 0^+	735	2.87	3.08	1.22	3.06	5.25
^{114}Cd	$g.s.$	534	1.46	–	0.811	4.62	4.77
^{116}Cd	$g.s.$	2805	0.774	0.521	0.405	1.08	1.04
$\hookrightarrow$	1294 keV, 2^+	1511	0.476	0.348	0.293	0.324	0.504
$\hookrightarrow$	1757 keV, 0^+	1048	1.41	1.44	0.177	1.91	3.61
$\hookrightarrow$	2027 keV, 0^+	778	0.998	0.561	0.346	0.704	1.68

Table 5.12: A list of obtained 90 % C.L. half lives of $0\nu\beta^-\beta^-$ decay to the ground state ($g.s.$) and excited states with the transition energy E. For the decay of ^{114}Cd to the $g.s.$ and ^{128}Te to the 443 keV 2^+ level the low energy data set has been used which does not include detector D2. For the other decays the high energy data set has been used.

The exclusion plot with the constant background plus signal fit is shown exemplarily for the decay of ^{116}Cd to the ground state in figure 5.22. In table 5.13 the results of the peak search are compared to the previously measured values with the COBRA test setup in Dortmund [Kie03] as described in section 2.5 and the current world best limits. A review of $2\nu\beta\beta$ and $0\nu\beta\beta$ decays of the year 2002 can be found in [Tre02].

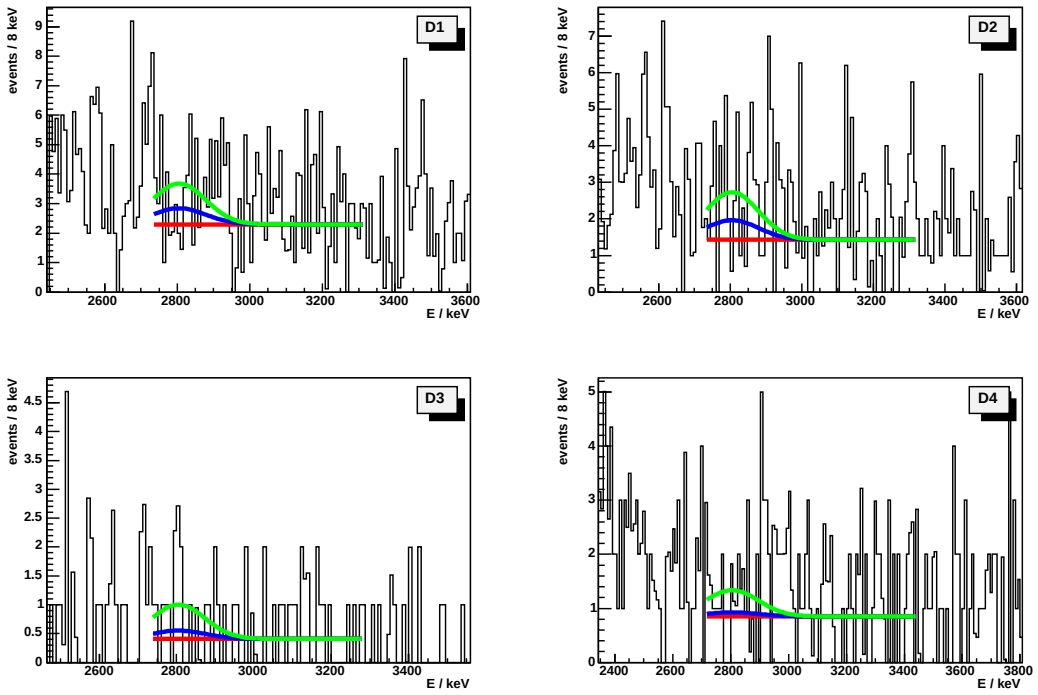

Figure 5.22: The exclusion plot for the $0\nu\beta^-\beta^-$ decay of ^{116}Cd to the ground state is shown for each detector. The red line denotes the fitted constant background. The blue line represents the background plus a Gaussian distribution with the width of the detector's energy resolution minimising the χ^2. The green line shows the 90 % excluded half life as specified in table 5.13. The background fit is asymmetric around the searched peak in order to exclude the 2.614 MeV gamma line.

		Half Life $T_{1/2}\,/\,a$			
Isotope / Level		This Work	[Kie03]	World Best	
^{70}Zn	$g.s.$	$> 2.83 \cdot 10^{17}$	$> 1.3 \cdot 10^{16}$	$> 0.7 \cdot 10^{18}$	[Dan04]
^{128}Te	$g.s.$	$> 4.58 \cdot 10^{19}$	$> 8.8 \cdot 10^{18}$	$> 1.1 \cdot 10^{23}$	[Arn03]
$\hookrightarrow$	443 keV, 2^+	$> 3.33 \cdot 10^{19}$	$> 1.3 \cdot 10^{18}$	$> 4.7 \cdot 10^{21}$	[Bel87]
^{130}Te	$g.s.$	$> 8.13 \cdot 10^{19}$	$> 3.3 \cdot 10^{19}$	$> 1.8 \cdot 10^{24}$	[Arn05]
$\hookrightarrow$	536 keV, 2^+	$> 1.13 \cdot 10^{20}$	$> 1.8 \cdot 10^{19}$	$> 9.7 \cdot 10^{22}$	[Ale00]
$\hookrightarrow$	1121 keV, 2^+	$> 3.91 \cdot 10^{19}$	$> 1.4 \cdot 10^{19}$	$> 2.7 \cdot 10^{21}$	[Bar01]
$\hookrightarrow$	1794 keV, 0^+	$> 5.25 \cdot 10^{19}$	$> 3.1 \cdot 10^{18}$	$> 2.3 \cdot 10^{21}$	[Bar01]
^{114}Cd	$g.s.$	$> 4.77 \cdot 10^{19}$	$> 6.4 \cdot 10^{18}$	$> 2.5 \cdot 10^{20}$	[Dan03]
^{116}Cd	$g.s.$	$> 1.04 \cdot 10^{19}$	$> 8.0 \cdot 10^{18}$	$> 1.7 \cdot 10^{23}$	[Dan03]
$\hookrightarrow$	1294 keV, 2^+	$> 5.04 \cdot 10^{18}$	$> 1.6 \cdot 10^{18}$	$> 1.3 \cdot 10^{22}$	[Dan00]
$\hookrightarrow$	1757 keV, 0^+	$> 3.61 \cdot 10^{19}$	$> 2.7 \cdot 10^{18}$	$> 7.0 \cdot 10^{21}$	[Dan00]
$\hookrightarrow$	2027 keV, 0^+	$> 1.68 \cdot 10^{19}$	$> 7.0 \cdot 10^{17}$	$> 2.1 \cdot 10^{21}$	[Pie94]

Table 5.13: A comparison of the 90 % C.L. half lives of $0\nu\beta^-\beta^-$ decay to the ground state ($g.s.$) and excited states obtained with the current work, the previously published values of the COBRA experiment [Kie03] and the world best limits.

For isotope the highest Q-value, ^{116}Cd, a joint limit on the $0\nu\beta^-\beta^-$ half life of

$$T_{1/2} > 1.04 \cdot 10^{19}\,\mathrm{a}\ (90\,\%\,\mathrm{C.L.}) \tag{5.6.31}$$

has been reached with the current setup running in the LNGS. This is only a modest improvement compared to the previously published value of the COBRA experiment of $0.8 \cdot 10^{19}$ a [Kie03]. For the second most important isotope ^{130}Te a half life of

$$T_{1/2} > 8.13 \cdot 10^{19}\,\mathrm{a}\ (90\,\%\,\mathrm{C.L.}) \tag{5.6.32}$$

has been achieved. Again, this half life is only a factor 2.5 enhanced compared the the previous value. The limiting factor of the current setup seems to be the background caused by the passivation paint on the crystals.
From the measured half life limits a limit on the neutrino mass can be given according to calculations for decays to the ground state from [Sta90]. In table 5.14 the resulting neutrino mass limits are listed. The best value of 77.6 eV for ^{130}Te has to be compared to 0.35 eV from ^{76}Ge [KK01b].

Isotope	$T^{0\nu}_{1/2}$ / 10^{19} a	$T^{0\nu}_{1/2} \cdot \langle m_\nu\rangle^2$ / a eV^2	$\langle m_\nu\rangle$ / eV
^{70}Zn	> 0.0283	$9.83 \cdot 10^{25}$	>18600
^{114}Cd	> 4.77	$5.07 \cdot 10^{25}$	> 1030
^{128}Te	> 4.58	$7.77 \cdot 10^{24}$	> 412
^{116}Cd	> 1.04	$4.87 \cdot 10^{23}$	> 216
^{130}Te	> 8.13	$4.89 \cdot 10^{23}$	> 77.6

Table 5.14: List of obtained neutrino mass limits deduced from half life limits of $0\nu\beta^-\beta^-$ decay to the ground state using the nuclear matrix elements from [Sta90].

Although an intensive shielding of the detector setup and a selection of clean construction materials can reduce the overall background of the data, especially for $0\nu\beta\beta$ decay an irreducible background component remains: due to the finite energy resolution of the detectors, the $2\nu\beta\beta$ spectrum contributes to the number of events at the endpoint. Figure 5.23 shows the endpoint region for ^{116}Cd. The theoretical $2\nu\beta\beta$ spectrum is drawn as a dotted line normalised to 1 event over the whole spectrum. The solid line represents the $2\nu\beta\beta$ spectrum with an energy resolution of 40 keV FWHM which corresponds to a projected energy resolution of 1.4 % for future detectors. This spectrum has to be compared to the Gaussian distribution of events in the $0\nu\beta\beta$ peak with a half life chosen to be six orders of magnitude above the half life of the 2ν mode, i.e. a peak content of 10^{-6}.
A clear distinction between the two modes is visible despite the fact that the two distributions do overlap. The only problem discriminating the two spectra would be if the number of detected counts is low, but this can be cured by a longer measuring time.
As CdZnTe detectors have many isotopes instable to double beta decay, also those isotopes with a lower Q-value than others suffer from background of the other isotopes with a higher Q-value. At the current state of the COBRA experiment, however, the dominating background is still coming from radioactive nuclides near the detector, mostly from the passivation paint covering 5 sides of the detectors.

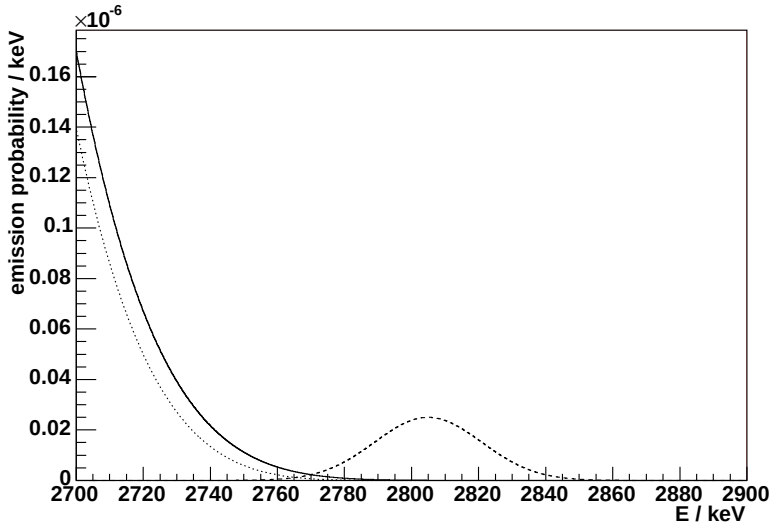

Figure 5.23: The spectrum of the $2\nu\beta\beta$ decay of ^{116}Cd [Tre95] is drawn against the 2805 keV $0\nu\beta\beta$ peak. The half life of the 0ν mode is chosen to be six orders of magnitude larger than for the 2ν mode. The theoretical 2ν spectrum as indicated by a dotted line has been folded with an energy resolution of 40 keV FWHM which is denoted by a solid line. The 0ν peak shown as a dashed line is folded with the same energy resolution. Though both spectra do overlap a clear distinction can be seen.

5.7 The $0\nu\beta^+\beta^+$ Half Lives

The search for the β^+ modes of $0\nu\beta\beta$ decay is a more complex task. This is in part due to the distinctive submodes, i.e. the combination of β^+ and EC, but also due to the lower Q-values per β^+ as described in equation 1.2.17. The only isotope under study which may decay via $0\nu\beta^+\beta^+$ is ^{106}Cd with a Q-value of 2771 keV. The sum energy of the two positrons is 727 keV.

For any $\beta^+\beta^+$ or β^+EC decay the emitted positrons annihilate at rest after having deposited their kinetic energy. This produces two 511 keV gammas pointing in opposite directions. The efficiency to detect the full energy of each of these gammas in one detector is only about 7%. However, the efficiency to leave the detector without depositing energy is 79%. Thus it is advantageous to search for a peak at the reduced energy of the transition.

For the EC modes, the K-shell energy E_K is emitted in photons from the daughter nucleus. This energy is 49 keV, 30 keV and 17 keV for Cd, Te and Zn respectively. The efficiency for a full absorption of the 49 keV photon in the detector crystal is 96.5 % so that for a $0\nu\beta^+$EC decay the total energy to be searched is $Q - 2 \cdot 511\,\text{keV} + E_K$. A complete list of the experimental signals of the distinct β^+ modes is shown in table 5.15.

Decay Mode	Signature	Energy
$0\nu\beta^+\beta^+$	$2e^+$	$Q - 4m_e$
$0\nu\beta^+\beta^+\gamma_\ell$	$2e^+$, γ_ℓ	$Q - 4m_e - E_{\gamma_\ell}$
$0\nu\beta^+$EC	e^+, γ_K	$Q - 2m_e + E_K$
$0\nu\beta^+$ECγ	e^+, γ_K, γ_ℓ	$Q - 2m_e + E_K - E_{\gamma_\ell}$
2νECEC	$2\gamma_K$	$2E_K$
2νECECγ_ℓ	$2\gamma_K$, γ_ℓ	$2E_K + E_{\gamma_\ell}$
0νECEC	γ_{rad}, $2\gamma_K$	Q
0νECECγ_ℓ	γ_{rad}, $2\gamma_K$, γ_ℓ	$2E_K + E_{\gamma_\ell}$

Table 5.15: The experimental signature of the different β^+-modes of double beta decay are shown with their full energy E. The decay to excited states is indicated by an additional gamma γ_ℓ.

Using the shown energy signatures and the corresponding detection efficiencies, limits on the half lives of the $0\nu\beta^+\beta^+$and $0\nu\beta^+$EC decays to the ground state and excited states of the daughter nucleus can be calculated. In table 5.16 the results of the search are summarised and compared to the previous measurement of the COBRA experiment [Kie03] and the world best limits.

No limits on 2νEC EC decays could be calculated because of a too high threshold. The highest signature would be for cadmium with an energy of 98 keV. For the two isotopes ^{106}Cd and ^{108}Cd only a joint limit could be given for 2νEC EC decay anyway, because the K-shell energy is the same. Nevertheless, for the 0νEC EC decay of ^{106}Cd to the first and second excited level of the daughter nucleus at 512 keV and 1171 keV and the first excited level of the daughter nucleus of ^{120}Te at 1134 keV limits on the half life could be set.

Isotope / Level	Mode	E / keV	Half Life $T_{1/2}$ / a This Work	[Kie03]	World Best	
^{106}Cd $g.s.$	$0\nu\beta^+\beta^+$	727	$> 7.0 \cdot 10^{17}$	$> 1.5 \cdot 10^{17}$	$> 2.2 \cdot 10^{19}$	[Dan96b]
512 keV, 2^+	$0\nu\beta^+\beta^+$	215	$> 7.5 \cdot 10^{16}$	$> 7.4 \cdot 10^{16}$	$> 1.6 \cdot 10^{20 a}$	[Bel99]
$g.s.$	$0\nu\beta^+$EC	1798	$> 1.6 \cdot 10^{18}$	$> 3.8 \cdot 10^{17}$	$> 3.7 \cdot 10^{20}$	[Bel99]
512 keV, 2^+	$0\nu\beta^+$EC	1286	$> 9.4 \cdot 10^{17}$	$> 2.2 \cdot 10^{17}$	$> 2.6 \cdot 10^{20}$	[Bel99]
1134 keV, 0^+	$0\nu\beta^+$EC	664	$> 4.4 \cdot 10^{17}$	$> 7.5 \cdot 10^{16}$	$> 1.1 \cdot 10^{20}$	[Bel99]
512 keV, 2^+	0νEC EC	610	$> 5.0 \cdot 10^{16}$	$> 8.3 \cdot 10^{17}$	$> 3.5 \cdot 10^{18}$	[Bar96]
1134 keV, 0^+	0νEC EC	1232	$> 4.6 \cdot 10^{16}$	—	$> 6.2 \cdot 10^{18}$	[Bar96]
^{120}Te $g.s.$	$0\nu\beta^+$EC	730	$> 9.3 \cdot 10^{16}$	$> 2.2 \cdot 10^{16}$		[Kie03]
1171 keV, 2^+	0νEC EC	1231	$> 6.1 \cdot 10^{15}$	$> 8.4 \cdot 10^{15}$		[Kie03]
^{64}Zn $g.s.$	$0\nu\beta^+$EC	602	$> 2.6 \cdot 10^{17}$	$> 2.8 \cdot 10^{16}$	$> 2.3 \cdot 10^{18 *}$	[Nor85]

Table 5.16: A comparison of the half lives of $0\nu\beta^+\beta^+$ decay to the ground state ($g.s.$) and excited states obtained with the current work and the previously published values of the COBRA experiment and the world best limits. Values are quoted at a confidence level of 90 %, unless marked with a * in which case the confidence level is only 68 %. An ^{a} indicates a combined limit on the 0ν and 2ν modes.

For most of the decay modes improved half life limits could be set compared to the previous publication of the COBRA experiment [Kie03]. For the 0νEC EC decays to excited states, however, only lower limits could be set, because the energy threshold of the Prototype detectors is higher than for the CPG2 detector. Therefore, the two K-shell gammas plus the de-excitation gamma had to be detected, which has a lower efficiency than only the two K-shell gammas and no energy deposition of the de-excitation gamma which was the signal searched for in [Kie03]. Nevertheless, for the $0\nu\beta^+$EC decay of ^{120}Te a world best limit could be obtained.

5.8 Other Rare Decays

In addition to the studies of 2ν and 0ν double beta decays and the 4-fold forbidden non-unique beta decay of ^{113}Cd, other rare decays may be searched for in the present data. Two of these decays are the radiative electron decay and the decay of ^{113}Cd to neutrals as shown in the following two sections.

The Radiative Electron Decay

As already mentioned, a half life limit on the decay of the electron can be calculated. The process under study is the radiative electron decay

$$e^- \rightarrow \nu_e \gamma \tag{5.8.33}$$

which is a charge non-conserving process (CNC) [Pra03]. The current limit is set as $T_{1/2} > 6.6 \cdot 10^{26}$ a (90 % C.L.) [Bac02] which is also a lower limit of the total half life of the electron [Eid04]. As the neutrino and the gamma are emitted back-to-back, the signal would be a single gamma with $E = \frac{1}{2} m_e = 255.5\,\text{keV}$. However, as the electrons under study are bound in the CdZnTe sample, their binding energy must be subtracted [Bal93]. The binding energies for the K-shells are 26.7 keV, 9.7 keV and 31.8 keV for Cd, Zn and Te, respectively, however, only two electrons per atom are in the K-shell. To simplify the analysis these electrons may be rejected. The binding energy for the L- and M-shells is well below 5 keV which has to be compared to the energy resolution of the detectors of about 30 keV for the signal energy. Thus, the correction for the L- and M-shells may be neglected as a first approximation.
Hence, the mean number of electrons under study for $Cd_{0.9}Zn_{0.1}Te$ is 94.2 per compound. This number is about a factor 500 larger than the number of ^{130}Te nuclei which is the most common isotope in CdZnTe with a relative abundance of 16.9 %. This means an increased sensitivity of this process compared to double beta decays. Due to the Doppler shift a broadening of the photo peak has to be expected as well. However, again this effect may be neglected in comparison to the finite energy resolution of the detectors.
The main background of this decay comes from the shoulder of the ^{113}Cd beta decay which dominates the count rate. The excluded number of events obtained with the χ^2 method using an exponential background model corresponds to a half life limit of

$$T_{1/2} > 1.3 \cdot 10^{20}\,\text{a}\ (90\,\%\ \text{C.L.}) \tag{5.8.34}$$

which is still about six orders of magnitude smaller than the result of [Bac02]. Better limits may be obtained if the background from ^{113}Cd can be further reduced, e.g. by enriching the detector material in ^{116}Cd.

The Neutral Decay of ^{113}Cd

The charge non-conserving decay of a nucleus into its daughter nucleus and only neutrals is a possible scenario as well. The involved reaction can be described as

$$n \rightarrow p + \nu_e + \bar{\nu}_e. \tag{5.8.35}$$

One candidate isotope for this decay is ^{113}Cd:

$$^{113}\text{Cd} \rightarrow {}^{113m}\text{In} + \text{neutrals}. \tag{5.8.36}$$

In figure 5.24 the energy levels of the involved nuclei are given. In this process the signal is the decay of ^{113}Cd without emission of an electron but with a 391.7 keV gamma resulting from the internal transition (IT) of the excited ^{113m}In nucleus. This process is only energetically allowed if no electron is emitted in the final state.

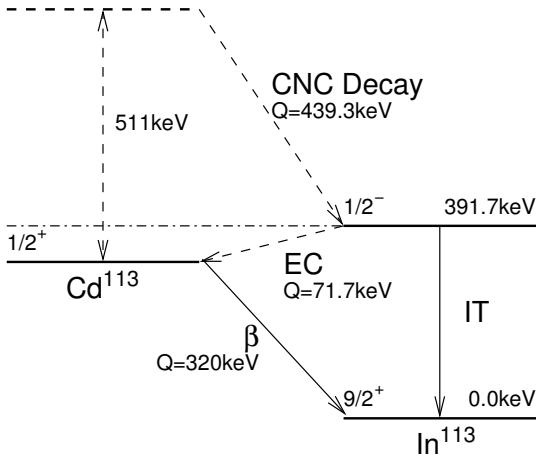

Figure 5.24: The scheme of the ^{113}Cd CNC decay is shown including the involved energy levels. The branching ratio of electron capture (EC) of ^{113m}In is $< 0.0036\,\%$.

The current limit of the COBRA experiment for this process is

$$T_{1/2} > 1.47 \cdot 10^{19}\,\mathrm{a}\;(90\,\%\;\mathrm{C.L.}) \tag{5.8.37}$$

which is an improvement of about a factor 10 compared to the previously measured half life limit of $T_{1/2} > 1.4 \cdot 10^{18}$ a (90 % C.L.) [Roy83]. However, for the decay of ^{113}Cd into neutrals only a rather modest half life limit has been measured so far. More stringent limits were obtained for other isotopes like ^{71}Ga with a measured half life limit of $T_{1/2} > 2.4 \cdot 10^{26}$ a (68 % C.L.) [Nor96].

Chapter 6

Summary

The COBRA experiment is approaching a new step in its evolution. In the beginning, the project started with investigations using commercial detectors. From the attained knowledge a 2×2 array of detectors was constructed which can be scaled up to at least 16 detectors. This detector array was installed at the Laboratori Nazionali del Gran Sasso, Italy, in a complex shielding which has been designed and built from scratch as well. The data taken with this setup has been presented and analysed in this work. Based on this knowledge the design of a $4 \times 4 \times 4$ detector array has been recently started which attracted more collaborators.
Currently the 64 detector array as described in section 2.7 is in the phase of construction using a detector holder based on the 2×2 array mentioned in chapter 2.6. Other groups are working on improving the shielding system or investigating the use of pixelated detectors for future upgrades.

6.1 Conclusions

A new VME data acquisition system including a custom built ADC has been developed during this thesis. It has been shown in this work that the new system is working well and will be scalable to 64 channels. The custom built VME ADC has undergone a vast number of debugging and stability tests and is currently proving its reliability in real data taking in the LNGS. It replaces the CAMAC system curing the problems of its aged electronic components and offering enough readout channels for the $4 \times 4 \times 4$ detector array.
Nevertheless, as already stated valuable data has been recorded using the CAMAC data acquisition system. With this data different analyses of rare decays have been performed.
With three of the four detectors of the 2×2 array the value of the half life of the 4-fold forbidden beta decay of ^{113}Cd has been measured, resulting in a mean of

$$T_{1/2}(^{113}\text{Cd},\, \beta^-) = \left(8.2 \pm 0.2(\text{stat.})^{+0.2}_{-1.0}(\text{syst.})\right) \cdot 10^{15}\,\text{a}\ (90\,\%\ \text{C.L.}) \tag{6.1.1}$$

using the spectral shape of the spectrum as measured by [Dan96a].
This outcome is consistent with the previously measured values of $T_{1/2} = (7.7 \pm 0.3) \cdot 10^{15}$ a [Dan96a] and $T_{1/2} = (9.0 \pm 0.5(\text{stat.}) \pm 1.0(\text{syst.})) \cdot 10^{15}$ a [Ale94]. However, this measurement does not solve the slight discrepancy of both half lives. Also the shape of the beta spectrum could not be analysed because of the low energy noise obliterating the spectral shape

below its maximum. Nevertheless, the shape of the spectrum as specified by the "Table of Isotopes" [Chu99, Aud95] can be excluded.
The main interest of the COBRA experiment lies in the measurement of double beta decays. For the $2\nu\beta^-\beta^-$ decay of ^{116}Cd the current sensitivity is at a level of

$$T_{1/2}(^{116}\text{Cd},\, 2\nu\beta^-\beta^-) \;>\; 1\cdot 10^{17}\,\text{a}\;(90\,\%\;\text{C.L.}) \tag{6.1.2}$$

which is less than three orders lower than the known value of $T_{1/2} = 2.9\cdot 10^{19}$ a [Dan03]. Therefore, for the detection of $2\nu\beta^-\beta^-$ decays the background has to be lowered. However, as most of the background can be attributed to the passivation paint on the detectors a significantly improved sensitivity is to be expected if the paint can be avoided.
Improved limits on the $0\nu\beta\beta$ decay half lives compared to a previous publication [Kie03] have been achieved as well. For the most important isotopes ^{116}Cd and ^{130}Te which have the highest Q-values a limit of 90 % C.L. of the $0\nu\beta^-\beta^-$ decay has been set of

$$T_{1/2}(^{116}\text{Cd},\, 0\nu\beta^-\beta^-) \;>\; 1.04\cdot 10^{19}\,\text{a}, \tag{6.1.3}$$

$$T_{1/2}(^{130}\text{Te},\, 0\nu\beta^-\beta^-) \;>\; 8.13\cdot 10^{19}\,\text{a}. \tag{6.1.4}$$

For the first time of the COBRA experiment a half life limit $> 10^{20}$ years has been measured:

$$T_{1/2}(^{130}\text{Te},\, 0\nu\beta^-\beta^- \rightarrow 536\,\text{keV}(0^+\rightarrow 2^+)) \;>\; 1.13\cdot 10^{20}\,\text{a}\;(90\,\%\;\text{C.L.}). \tag{6.1.5}$$

The half life limit of the decay of ^{130}Te to the ground state leads to an upper limit of the neutrino mass of

$$\langle m_\nu\rangle \;<\; 77.6\,\text{eV} \tag{6.1.6}$$

using the nuclear matrix elements from [Sta90] and assuming the parameters $\langle\lambda\rangle$ and $\langle\eta\rangle$ of the right handed weak current to be zero. This value has to be compared to the currently best limit of 0.35 eV from ^{76}Ge [KK01b].
Although the highest half life limits are not yet competitive with other experiments, for the $0\nu\beta^+$EC decay of ^{120}Te to the ground state a half life of

$$T_{1/2}(^{120}\text{Te},\, 0\nu\beta^+\text{EC}) \;>\; 9.3\cdot 10^{16}\,\text{a}\;(90\,\%\;\text{C.L.}) \tag{6.1.7}$$

was obtained which surpasses the most stringent limit ever measured for this decay mode of $T_{1/2} > 2.2\cdot 10^{16}$ a [Kie03].
In addition to the analysis of double beta decays a search for other processes, e.g. charge non-conserving processes (CNC) can be performed. For the radiative decay of the electron a lower limit of the half live was measured as

$$T_{1/2}(\text{e}^-\rightarrow\nu_\text{e}\gamma) \;>\; 1.3\cdot 10^{20}\,\text{a}\;(90\,\%\;\text{C.L.}) \tag{6.1.8}$$

which is about six orders of magnitude lower than the current best limit of $T_{1/2} > 6.6\cdot 10^{26}$ a [Bac02]. Another CNC process is the decay of ^{113}Cd to ^{113m}In and only neutral particles. For this decay even a world best limit of

$$T_{1/2}(^{113}\text{Cd}\rightarrow {}^{113m}\text{In} + \text{neutrals}) \;>\; 1.47\cdot 10^{19}\,\text{a}\;(90\,\%\;\text{C.L.}) \tag{6.1.9}$$

was achieved, which is an improvement of one order of magnitude to the previous measurement of $T_{1/2} > 1.4 \cdot 10^{18}$ a (90 % C.L.) [Roy83].
In addition to the constructional activities on the Prototype and its readout system extensive simulations have been performed using the Monte Carlo program "POISON" presented in chapter 4. This program has been developed as part of the activities carried out for this thesis and is now used in the collaboration as the default simulation tool. Therefore, it helped in designing the $4 \times 4 \times 4$ array as well as in understanding the sources of radioactive background in the current Prototype detector. The background observed in the measured spectra could be identified as originating from the passivation paint. Background from other sources has been identified and reduced by exchanging the critical materials. The new detector holder based on the clean material Delrin is currently in use and shows a reduced background contribution.

6.2 Outlook

It can be expected that with the 64 array new physics results can be achieved, such as a precision measurement of the ^{113}Cd 4-fold forbidden beta decay. This measurement will not only involve the half life of the decay but also the spectral shape of the energy distribution.
The prospect of the detector array is to show the power of coincidences in order to reject background. However, only modest improvements are expected if not considering coincidences as the passivation paint is the dominant background source. Still, the augmented detector mass and the clean Delrin holder will contribute to improve the limits of double beta decays.
The next step of the COBRA experiment is therefore to remove the passivation paint. Other topics are an increase of the detector mass to several kilograms or the use of pixelated detectors to further improve background rejection.
Data measured with the CAMAC data acquisition suffered not only from hardware malfunction, but had a rather high threshold of at least 80 keV. Measurements with the CPG2 detector using the PC-MCA based data acquisition system showed that the threshold of the detectors can be lowered further. First data taken with the new VME based DAQ confirms a lower threshold of about 20 keV for the Prototype detector as well. However, not enough statistics has been gathered yet to carry out an analysis of rare decays. This improved threshold opens a window to the detection of double electron capture processes and the single electron capture of ^{123}Te. The latter decay was investigated with the commercial detector mentioned above, however, only achieving an upper limit of $T_{1/2} > 3.2 \cdot 10^{16}$ a [Mue03] due to the noise of the detector.
The Q-value of the second forbidden unique electron capture of ^{123}Te is (53.3 ± 0.2) keV [Aud95]. There are two positive evidences for this decay mode, but they show a discrepancy by six orders of magnitude in half life. The two values are $(1.24 \pm 0.10) \cdot 10^{13}$ years [Wat62] and $(2.4 \pm 0.9) \cdot 10^{19}$ years [Ale96]. The higher evidence has been recently withdrawn by repeating the experiment [Ale03]. There was indeed a signal at the expected energy, however, this signal is now attributed to neutron activation of ^{120}Te producing ^{121}Te and ^{121m}Te. As the thermal neutron flux in the location of this experiment is significantly reduced, this activation is thought to have taken place before the measurement when the detectors have been stored on earth surface. The new measurement revealed a lower limit of the half life of electron capture from the K-shell of $T^K_{1/2} > 5 \cdot 10^{19}$ a which corresponds to $T_{1/2} > 9.2 \cdot 10^{16}$ a using the predicted K EC branching ratio.
This same background may well account for the signal measured by [Wat62]. Another problem

is associated with the fact that the observations relied on the outside detection of K X-rays following the de-excitation of ^{123}Sb. This line is at 26.1 keV, very close to the Te K X-ray line at 27.3 keV which might be excited by other processes like cosmic rays and radioactive background.
The advantage of the COBRA experiment for the detection of this decay is that it also features the source=detector principle and has a sophisticated neutron shield. It will also be possible to discriminate the background K X-rays from the signal thanks to the good energy resolution of the detectors. Yet, with the first measurement from [Mue03] already the usually quoted half life limit of $T_{1/2} > 10^{13}$ a [Chu99] can be improved by three orders of magnitude.
Another prospect of the COBRA experiment may be the real time detection of solar neutrinos [Zub03]. To accomplish this, the mass of the detector surely has to be extended to several tons. The investigated neutrinos originate from the decay of ^{7}Be in the sun as a mono-energetic 862 keV neutrino line as shown in figure 6.1. As a detection process a coincidence of the inverse beta decay process with a following beta decay

$$\nu_e + (A, Z) \quad \rightarrow \quad (A, Z+1)_{g.s.} + e^- \tag{6.2.10}$$

$$(A, Z+1) \quad \rightarrow \quad (A, Z+2) + e^- + \bar{\nu}_e \tag{6.2.11}$$

is searched for. Thus the signature is a mono-energetic electron of the neutrino capture with an energy of $E_e = E_\nu - (E_f - E_i)$ and a following high energetic beta in the same detector crystal. This process is possible for two of the five $\beta^-\beta^-$ emitters in CdZnTe: ^{70}Zn ($E_e = 207$ keV) and ^{116}Cd ($E_e = 368$ keV). For ^{130}Te this process is not possible because of the angular momentum 5^+ of the daughter nucleus ^{130}I. Here, the transition to the first 1^+ excited state of ^{130}Te at 43.25 keV is possible. The signal to be expected is

$$\nu_e + (A, Z) \quad \rightarrow \quad (A, Z+1)^* + e^- \tag{6.2.12}$$

$$(A, Z+1)^* \quad \rightarrow \quad (A, Z+1)_{g.s.} + \gamma. \tag{6.2.13}$$

This process has a threshold of the neutrino energy of 494 keV.

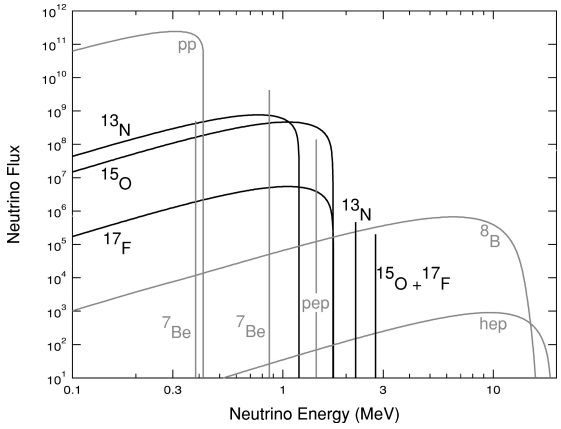

Figure 6.1: Neutrino flux from the sun at the distance of the earth, including electron capture in the CNO cycle [For04]. The pp chain is shown in grey and the CNO cycle is shown in black. Line fluxes are in cm^{-2}s^{-1} and continuum fluxes are in cm^{-2}s^{-1}MeV^{-1}.

Appendix A

Natural Decay Chains

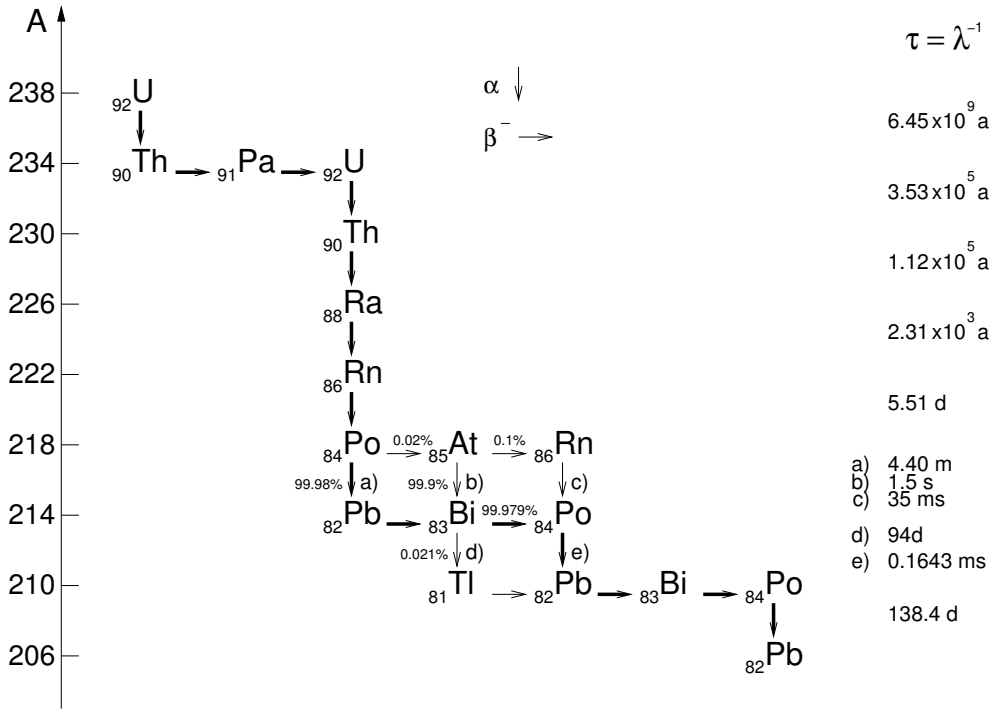

Figure A.1: Natural decay chain of ^{238}U [Wah96]. Alpha decays are denoted by down going arrows, beta decays by arrows pointing to the right side. The main decay channel is marked with thick arrows. The half lives to the right indicate only the values for the alpha decays as they dominate the decay chain.

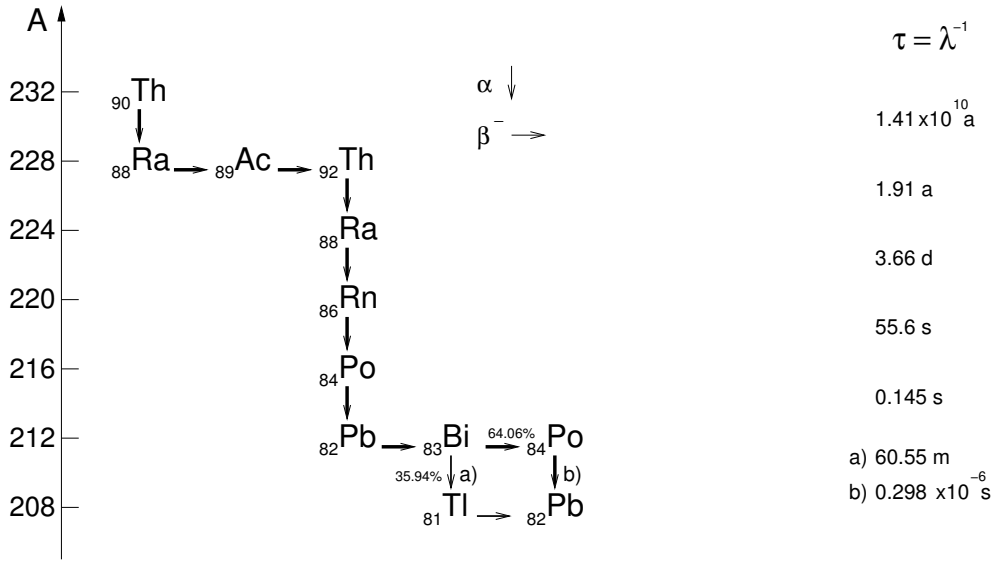

Figure A.2: Natural decay chain of ^{232}Th [Wah96].

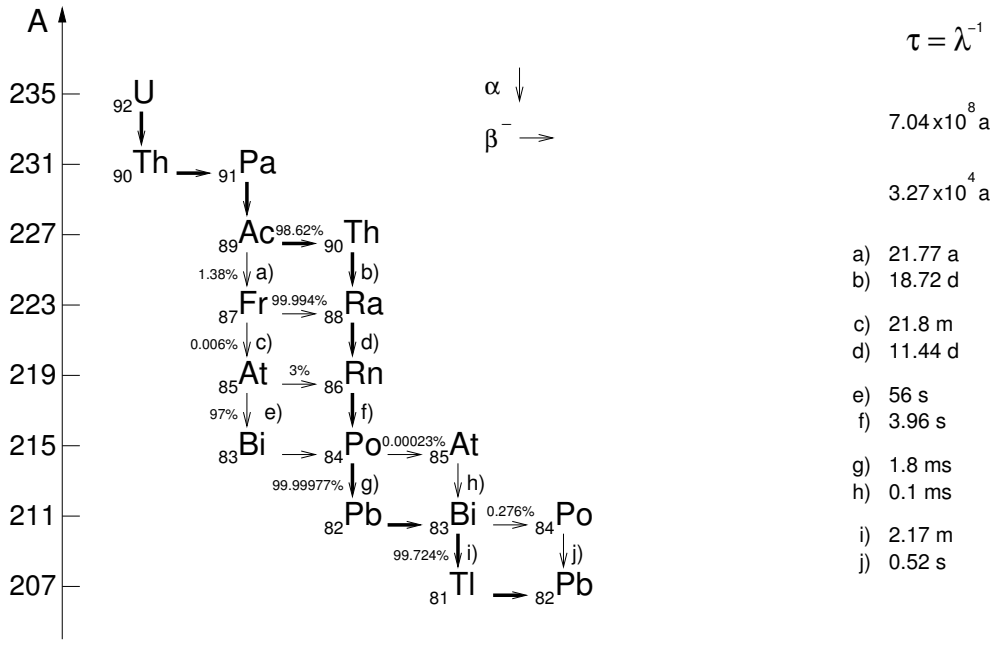

Figure A.3: Natural decay chain of ^{235}U [Wah96].

Appendix B

Technical Drawings

B.1 Delrin Holder

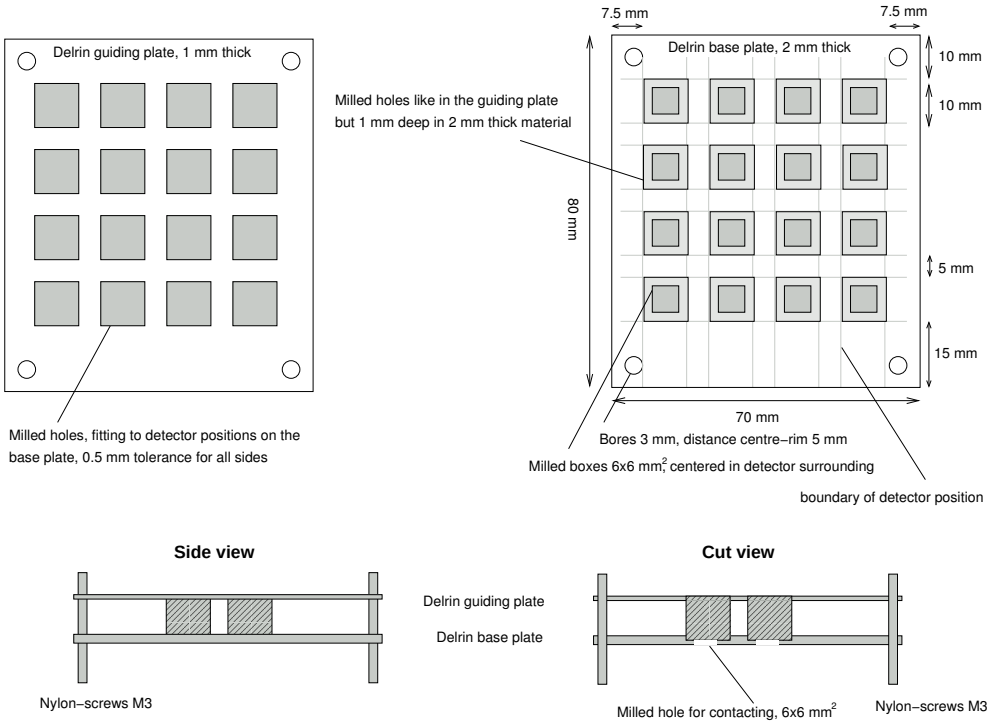

Figure B.1: Technical drawing of the Delrin holder with the dimensioning of the components. The holder is designed to host 16 detectors. Using the same holders, a 3-dimensional array of detectors can be built by stacking the layers.

Appendix C

Material Contaminations

C.1 Detector Material

Contaminant	CdZnTe	Passivation Paint	Zn	Cd	Te
		Activity / mBq kg^{-1}			
^{232}Th chain					
^{228}Ra	< 47	1100 ± 100	< 8	< 4	< 7
^{228}Th	< 60	730 ± 70	< 8	< 4	< 7
^{238}U chain					
^{226}Ra	< 51	2100 ± 100	< 8	< 4	< 7
^{234}Th	< 210	1100 ± 300	< 150	< 200	< 240
^{235}U chain	< 4	170 ± 30	< 5	< 4	< 5
^{40}K	< 260	6900 ± 800	< 55	< 24	< 51
^{137}Cs	40 ± 8	< 15	< 2	< 1	< 2
^{60}Co	< 19	< 60	< 3	< 2	< 4

Table C.1: The activities of the detector components are listed as measured by [Lau04]. The CdZnTe measurement is from non-functional detector material without passivation paint, the elemental analysis from metallic pieces of the raw materials Cd, Te and Zn provided by the manufacturer. The ^{137}Cs activity of the CdZnTe crystal which is well above the limits of the raw components is supposed to originate from improper handling of the crystal prior to measuring. The passivation paint has been kindly provided by the manufacturer as well.

C.2 Construction Material

Contaminant	Copper	Pertinax (brown/white)		Delrin
	Activity / mBq kg^{-1}			
^{232}Th chain				
^{228}Ra	< 2.1	29 ± 7	18 ± 3	< 5
^{228}Th	< 2.3	32 ± 7	15 ± 3	< 5
^{238}U chain				
^{226}Ra	< 2.5	170 ± 10	66 ± 4	< 5
^{234}Th	< 100	250 ± 110	< 92	n/a
^{235}U chain	< 1.4	12 ± 3	2 ± 1	< 3
^{40}K	< 11	330 ± 40	340 ± 30	< 31
^{137}Cs	< 0.9	650 ± 40	19 ± 2	3 ± 1
^{60}Co	< 0.6	< 4	< 2	< 2

Table C.2: The activities of the construction materials in the vicinity of the detectors are listed as measured by [Lau04]. The measured copper is the same material as the brick in which the Prototype resides. The ground plate of the Pertinax holder is made from brown Pertinax, whereas the top plate is made from copper coated white Pertinax.

Appendix D

Data Acquisition

D.1 Command Sets

D.1.1 CAMAC Command Set

Command	Action	Answer
HELLO	check if server answers	"YESMASTER"
QUIT	exit server	"GOODBYE"
HISTO/	*Histogramming Functions*	
... LIST	return a list of available histograms	bit pattern of available histograms
... GET/#1	return content of histogram #1	8192 integers
... CLEAR/#1	clear content of histogram #1	ID of cleared histogram
CALIB/	*Calibration Functions*	
... START	start writing out events into one single file may be used for calibrations	
... STOP	stop writing out data to calibration file	
SLOW/	*Slow Control Functions*	
... READOUT	Issue a readout of the slow control system	nothing
... GET	report the number of events recorded since start of the DAQ	integer
... UPTIME	report the time in seconds since start of the DAQ	unsigned long int
... **RELAIS/**		
..... SET/#1	switch on socket #1	bit pattern of active sockets
..... RESET/#1	switch off socket #1	bit pattern of active sockets
..... GET/#1	get status of sockets without switching	bit pattern of active sockets
... HVGET/#1	get current value of high voltage channel #1	integer
... HVSET/#1/#2	set current value of high voltage channel #1	integer
... HVADJUST/#1/#2	fix internal value of high voltage control	
... GETPREAMP/#1	get potentiometer setting of preamplifier channel #1	value of the potentiometer
... SETPREAMP/#1/#2/#3/#4	set the four potentiometers in the preamplifier to values #1 - #4	
DAQ/	*Data Acquisition Control Functions*	
... RUNNO	get the number of the current DAQ output file	6 integers: year, month, day, hour, minute, second
... STOP/#1	deactivate ADC#1, stop writing of events to disk if #1<0	bit pattern of active ADCs
... CONT/#1	activate ADC#1, start writing of events to disk if #1<0	bit pattern of active ADCs
... LIST	show available channels	bit pattern of available ADCs
... ACTIVE	show active channels	bit pattern of active ADCs
TDS/	*Oscilloscope Control*	
... RUN	reset trigger	1 if successful
... READ	read out stored waveform	1 if successful
... WHEN/#1/#2	channel #1, threshold #2	
... PUT#1/<string>	send string to the oscilloscope	answer string

Table D.1: Commands to control the CAMAC DAQ server.

D.1.2 VME Command Set

Command	Action	Answer
HELLO	check if server answers	"YESMASTER"
QUIT	exit server	"GOODBYE"
HISTO/	*Histogramming Functions*	
...LIST	return a list of available histograms	bit pattern of available histograms
...GET/#1	return content of histogram #1	16384 integers
...CLEAR/#1	clear content of histogram #1	ID of cleared histogram
CALIB/	*Calibration Functions*	
...START	start writing out events into one single file may be used for calibrations	
...STOP	stop writing out data to calibration file	
SLOW/	*Slow Control Functions*	
...DEBUG[/#1]	Change/check debug level (verbosity) of DAQ	current debug level
...GETCLEARCAP	report length of peak clear signal	length in μs
...CLEARCAP[/#1]	perform a peak clear of peak holder if specified, the length of the peak clear signal is set to #1 μs (range $0-1023$)	length in μs
...AUTOCLEARCAP[/#1]	initiate automatic peak clear every #1 s, or disable if ≤ 0 if no parameter is specified the current time interval is returned	length in s
...CLEARTIMER	reset timer on all VME boards	0
...DEADTIME/#1	set rise time protection of all VME boards to #1 μs (range $0-1023$)	new value
...GETDEADTIME	report rise time protection of all VME boards	current value in μs
...THRESHOLD/#1/#2	set threshold of channel #1 to #2	
...GETTHRESHOLD/#1	report threshold of channel #1	
...AMPLIFICATION/#1/#2	set amplification of channel #1 to #2	
...GETAMPLIFICATION/#1	report amplification of channel #1	
...DB9WRITE/#1/#2/#3/...	write the 7-bit data words #2, #3, ... to COBRA-DB9 port #1	
...READADC/#1	read value of slow control ADC channel #1	value of the ADC
...**TTL/**		
.....SET/#1	activate the bits of bit pattern #1 of the TTL-DB9	
.....RESET/#1	deactivate the bits of bit pattern #1 of the TTL-DB9	
.....FLASH/#1	flash the bits of bit pattern #1 of the TTL-DB9	
...**SERIAL/**		
.....SEND/<string>	send <string> to serial port	answer string of the device
DAQ/	*Data Acquisition Control Functions*	
...RUNNO	get the number of the current DAQ output file	6 integers: year, month, day, hour, minute, second
...NMOD	report number of ADC modules registered to the DAQ	number of modules
...STOP/#1	deactivate ADC#1, stop writing of events to disk if #1<0	bit pattern of active ADCs
...CONT/#1	activate ADC#1, start writing of events to disk if #1<0	bit pattern of active ADCs
...ACTIVE	show active channels	bit pattern of active ADCs
...TRIG/#1	do a software conversion start of ADC number #1	module number #1

Table D.2: Commands to control the VME DAQ server. Optional arguments are given in square brackets "[ ]"

D.2 Flow Chart

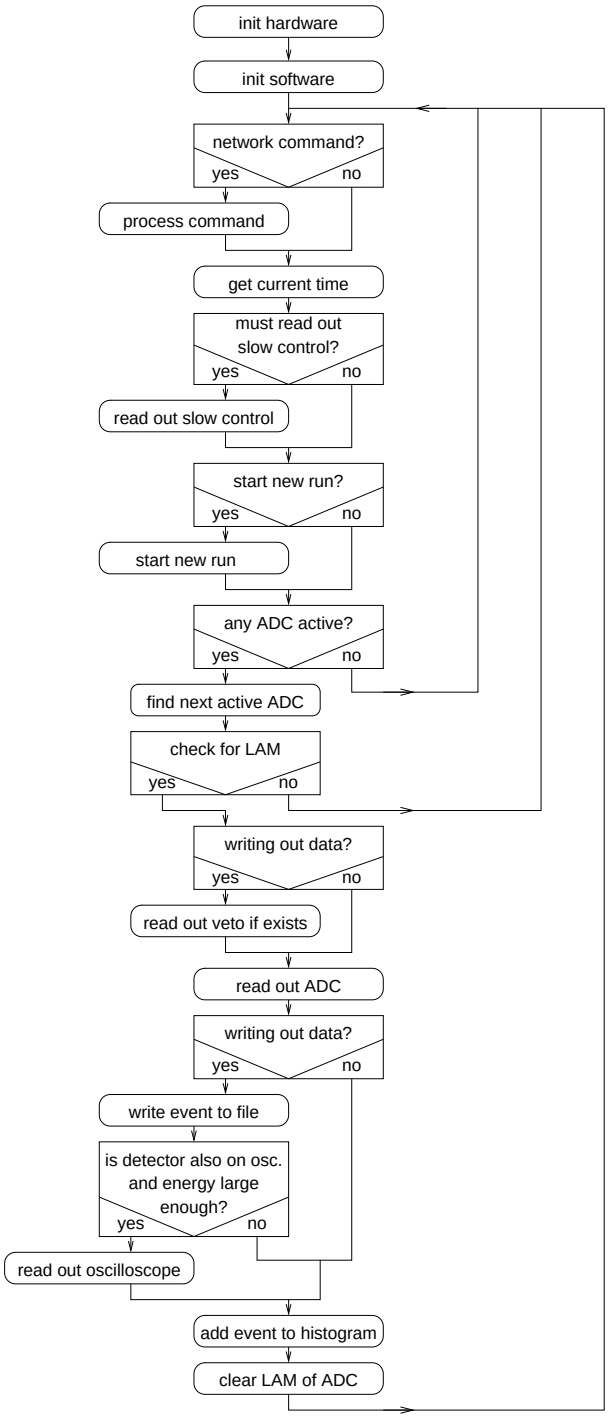

Figure D.1: Flow chart of the CAMAC DAQ server software. Rounded boxes indicate actions, squares represent conditional branches.

D.3 Data Files

D.3.1 CAMAC Data File

```
STARTdaq_2003_09_23_15_00_00.dat/34929200
3:34929204.111065:150:-1
3:34929248.530249:27:-1
1:34929252.615764:23:-1
4:34929258.393073:187:-1
[...]
2:34932718.756965:167:-1
END3600
```

Figure D.2: Extract of a sample CAMAC DAQ data file illustrating the data format. Each file contains a header stating the filename and starting time in Unix time-format and a footer stating the running time of the data file in seconds. Each other line represents one event with a colon (':') separated list of items: the number of the ADC, the system time at readout, the ADC value and a flag reporting the status of the veto. Its value '-1' denotes an inactive veto, '0' is no coincident veto and '1' stands for coincident veto.

D.3.2 VME Data File

```
STARTdaq_2005_03_22_09_00_00.dat/1111482000
1 4 1063343366 1111482053.931555 49 35 0 529 0 -22316 -26124 -27724
1 4 1075203827 1111482147.861565 59 38 0 321 0 -22220 -26108 -27644
1 4 1086191038 1111482234.881566 47 52 0 257 0 -22300 -26172 -27676
1 0 1108995473 1111482415.491554 282 42 0 30 0 -22252 -26140 -27628
1 1 1117419068 1111482482.201565 449 34 0 12 0 -22204 -26124 -27500
1 2 1120159048 1111482503.901554 23 426 0 26 0 -22236 -26092 -27660
1 4 1120389828 1111482505.731566 21 51 0 596 0 -22220 -26076 -27644
[...]
1 1 1470853400 1111485281.371565 393 47 0 20 0 -22220 -26060 -27580
1 1 1509671927 1111485588.801565 229 40 0 8 0 -22188 -26028 -27484
END3600
```

Figure D.3: Extract of a sample VME DAQ data file illustrating the data format. The header and footer are the same as for the CAMAC data file shown in figure D.2. Each event line contains a white space separated list of items: the module number of the ADC, the ADC channel with the highest value in this module, the internal timer value, the system time at the readout in Unix time, the four values of the ADC channels, the 14 bit TTL signal and three values of the slow control IP module ADC representing temperatures taken at the time of readout.

D.4 Transition Box

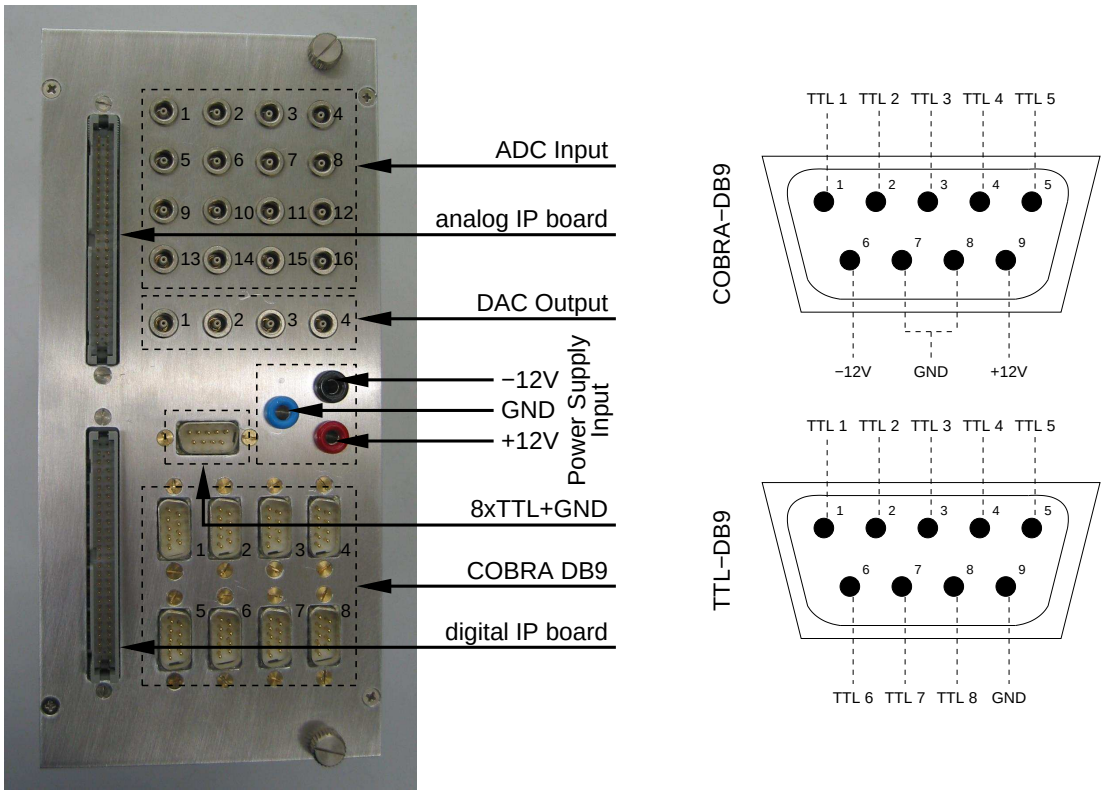

Figure D.4: The transition box for the slow control IP modules attached to the VME controller is shown on the left side. On the top right side the pin assignment of the COBRA-DB9 connector used for power supply and steering of the COBRA preamplifiers and shapers is schematically displayed. The bottom right schematic shows the pin assignment of the TTL-DB9 connector which is currently unused.

D.5 VME-ADC

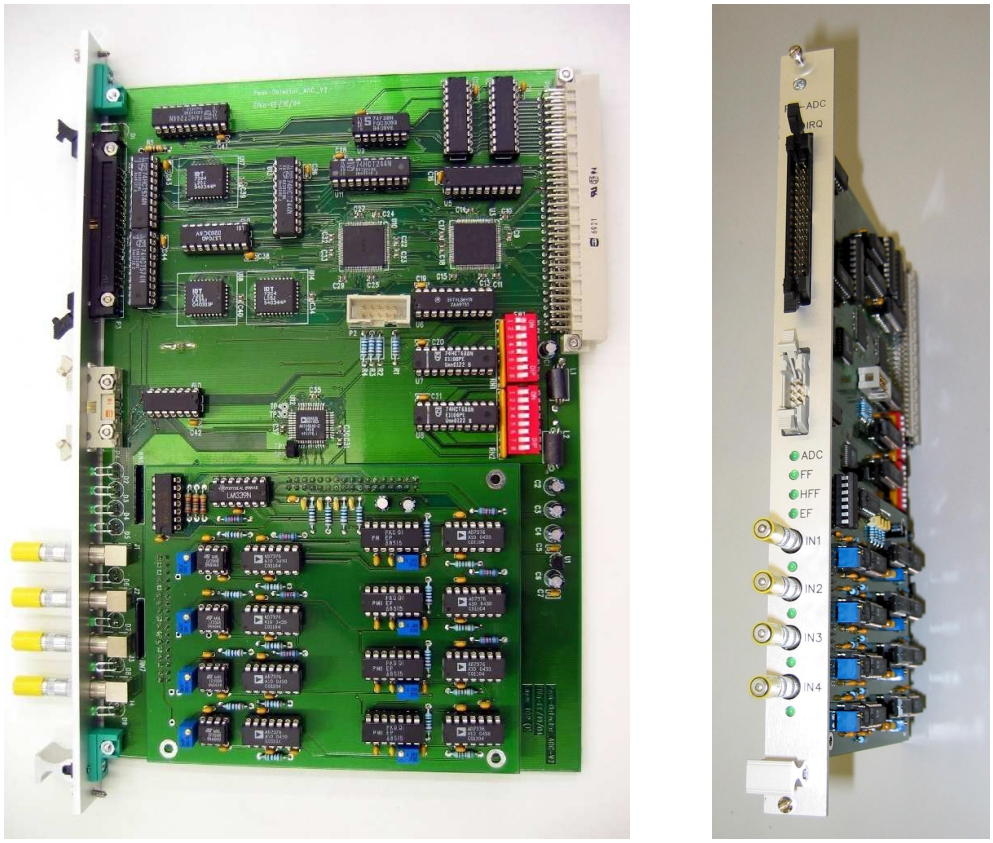

Figure D.5: Second version of the VME ADC. The analogue parts are separated from the digital part on a mezzanine board depicted in figure D.6. The digital parts include a TTL input register, internal timer, event buffer and VME bus control. The ADC chip is also located on this main board.

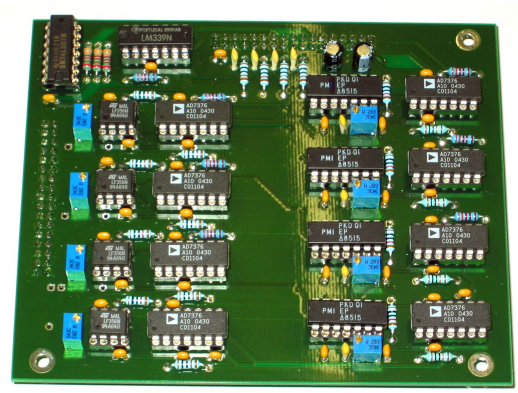

Figure D.6: VME ADC mezzanine board. The board contains the analogue parts – input amplifier, peak hold and threshold discriminator – of the four channels of the VME ADC.

Appendix E

Monte Carlo

E.1 POISON Input Files

```
# set up viewer
/vis/scene/create
/vis/open DAWNFILE
/vis/viewer/set/viewpointThetaPhi 25 60 deg
# set up track display
/tracking/storeTrajectory 1
/vis/scene/endOfEventAction accumulate
/vis/scene/add/trajectories
# set up generator
/setup/outfile sample2.dat
/setup/generator KielGen
/setup/location 5
/kielgen/mode 12
/run/beamOn 2000
```

Figure E.1: Sample sequence script for POISON generating 2000 ^{113}Cd beta events in the central detector of a $3\times3\times3$ array of $1\,\mathrm{cm}^3$ CdZnTe detectors.

E.2 POISON Output Files

```
*************************************************
*                                               *
*         POISON Version 0.9.2 (2005-01-14)     *
*                                               *
*************************************************
*   COBRA Monte Carlo Suite                     *
*************************************************
Parsing geometry file...

*************************************************************
 Geant4 version $Name: geant4-06-02-patch-01 $   (27-July-2004)
                      Copyright : Geant4 Collaboration
                      Reference : NIM A 506 (2003), 250-303
                            WWW : http://cern.ch/geant4
*************************************************************

Constructor()...
Materials...

phot:  Total cross sections from Sandia parametrisation.
Construct...
Detector Parameters:
          cdte_dimx = 10mm, cdte_dimy =  10mm, cdte_dimz = 10mm.
          gap_len = 2.5mm, gap_top = 3mm, tray_width = 5mm.
       paint_th = 0mm.
Creating Exp.Hall with 23cm x 17cm x 18.4cm
Creating a shielding:
  Lead shielding with walls,  x=1cm, y=1cm, z=1cm.
  Copper shielding with walls,  x=1cm, y=1cm, z=1cm.
Building 3x3x3 Array of CdZnTe with 1cm x 1cm x 1cm
Building stack of 3 excavations with dimensions x: 7.5cm, y: 4.5cm, z: 1.4cm.
Adding 0mm of paint to crystals
Visualization Manager instantiating...
Visualization Manager initialising...
Registering graphics systems...

You have successfully chosen to use the following graphics systems.
Current available graphics systems are:
  ASCIITree (ATree)
  DAWNFILE (DAWNFILE)
  GAGTree (GAGTree)
  G4HepRepFile (HepRepFile)
  G4HepRep (HepRepXML)
  RayTracer (RayTracer)
  VRML1FILE (VRML1FILE)
  VRML2FILE (VRML2FILE)
  OpenGLImmediateX (OGLIX)
  OpenGLStoredX (OGLSX)
  OpenGLImmediateXm (OGLIXm)
  OpenGLStoredXm (OGLSXm)
```

```
Idle> # set up viewer
Idle> Idle> 1 DAWNFILE scene handlers extanct.
WARNING: objects with visibility flag set to "false" will not be drawn!
  "/vis/viewer/set/culling global false" to Draw such objects.
  Also see other "/vis/viewer/set" commands.
Idle> Idle> Idle> G4Scene::AddWorldIfEmpty: The scene was empty,
   "world" has been added.

File  g4_00.prim  is generated.
dawn g4_00.prim
Idle> # set up track display
Idle> Idle> Idle> Idle> # set up generator
Idle>
Idle>
Idle> Location   5) in central Detector

Idle> Mode  12) Cd113 beta

Idle>
compt:  Total cross sections from a parametrisation. Good description from 10 KeV
to (100/Z) GeV.
       Scattered gamma energy according Klein-Nishina.
        PhysicsTables from 1 keV to 100 GeV in 80 bins.

conv:  Total cross sections from a parametrisation. Good description from 1.5 MeV
to 100 GeV for all Z.
        e+e- energies according Bethe-Heitler
        PhysicsTables from 1.022 MeV to 100 GeV in 100 bins.

msc:  Model variant of multiple scattering for e-
      Lambda tables from 100 eV  to 100 TeV in 120 bins.
      Boundary algorithm is active with facrange= 0.199

eIoni:   tables are built for  e-
      dE/dx and range tables from 100 eV  to 100 TeV in 120 bins.
      Lambda tables from threshold to 100 TeV in 120 bins.
      Step function: finalRange(mm)= 1, dRoverRange= 1, integral: 1
      Delta cross sections from Moller+Bhabha, good description from 1 KeV to 100 GeV.

eBrem:   tables are built for  e-
      dE/dx and range tables from 100 eV  to 100 TeV in 120 bins.
      Lambda tables from threshold to 100 TeV in 120 bins.
      Total cross sections from a parametrisation based on the EEDL data library.
      Good description from 1 KeV to 100 GeV, log scale extrapolation above 100 GeV.

eIoni:   tables are built for  e+
      dE/dx and range tables from 100 eV  to 100 TeV in 120 bins.
      Lambda tables from threshold to 100 TeV in 120 bins.
      Step function: finalRange(mm)= 1, dRoverRange= 1, integral: 1
      Delta cross sections from Moller+Bhabha, good description from 1 KeV to 100 GeV.

eBrem:   tables are built for  e+
      dE/dx and range tables from 100 eV  to 100 TeV in 120 bins.
      Lambda tables from threshold to 100 TeV in 120 bins.
      Total cross sections from a parametrisation based on the EEDL data library.
      Good description from 1 KeV to 100 GeV, log scale extrapolation above 100 GeV.
```

```
annihil:  Total cross section from Heilter formula(annihilation into 2 photons).
        gamma energies sampled according Heitler
        PhysicsTables from 10 keV to 10 TeV in 100 bins.
### All dEdx and Range tables are built #####

hIoni:   tables are built for  proton
      dE/dx and range tables from 100 eV  to 100 TeV in 120 bins.
      Lambda tables from threshold to 100 TeV in 120 bins.
      Step function: finalRange(mm)= 1, dRoverRange= 0.2, integral: 1
      Bether-Bloch model for Escaled > 2 MeV, parametrisation of Bragg peak below,
Integral mode 1

msc:  Model variant of multiple scattering for proton
      Lambda tables from 100 eV  to 100 TeV in 120 bins.
      Boundary algorithm is active with facrange= 0.199

File  g4_01.prim  is generated.
dawn g4_01.prim
Idle> Idle> Graphics systems deleted.
Visualization Manager deleting...
Exiting POISON cleanly.
```

Figure E.2: Sample output from POISON using the script from figure E.1 for a $3\times3\times3$ array of $1\,\mathrm{cm}^3$ CdZnTe detectors.

```
0 0 0 0 0 0 0 0 0 0 0 0 0 0 138.735 0 0 0 0 0 0 0 0 0 0 0 0 0 0 138.735 (keV) 138.735
1 0 0 0 0 0 0 0 0 0 0 0 0 0 223.604 0 0 0 0 0 0 0 0 0 0 0 0 0 0 223.604 (keV) 223.604
2 0 0 0 0 0 0 0 0 0 0 0 0 0 110.457 0 0 0 0 0 0 0 0 0 0 0 0 0 0 110.457 (keV) 110.457
...
1997 0 0 0 0 0 0 0 0 0 0 0 0 0 0 209.815 0 0 0 0 0 0 0 0 0 0 0 0 0 0 209.815 (keV) 209.815
1998 0 0 0 0 0 0 0 0 0 0 0 0 0 0 67.7068 0 0 0 0 0 0 0 0 0 0 0 0 0 0 67.7068 (keV) 67.7068
1999 0 0 0 0 0 0 0 0 0 0 0 0 0 0 187.499 0 0 0 0 0 0 0 0 0 0 0 0 0 0 187.499 (keV) 187.499
```

Figure E.3: Sample data file from POISON using the script from figure E.1 for a $3\times3\times3$ array of $1\,\mathrm{cm}^3$ CdZnTe detectors.

List of Tables

List of Figures

References

[Aal02] C. E. AALSETH ET AL. *Comment on 'Evidence for neutrinoless double beta decay'*. Modern Physics Letters A **17**, 1475 (2002).

[Ach04] P. ACHARD ET AL. *Measurement of the atmospheric muon spectrum from 20 to 3000 GeV*. Physics Letters B **598**, 15 (2004).

[Agl95] M. AGLIETTA ET AL. (LVD). *Neutrino induced and atmospheric single muon fluxes measured over five decades of intensity by LVD at Gran Sasso Laboratory*. Astroparticle Physics **3**, 311 (1995).

[Agl03] M. AGLIETTA ET AL. *Study of single muons with the Large Volume Detector at Gran Sasso laboratory*. Physics of Atomic Nuclei **66**, 123 (2003).

[Ago03] S. AGOSTINELLI. *GEANT4: A Simulation Toolkit*. Nuclear Instruments and Methods in Physics Research, Section A **506**, 250 (2003).

[Ahm02] Q. R. AHMAD ET AL. (SNO). *Direct evidence for neutrino flavor transformation from neutral-current interactions in the Sudbury Neutrino Observatory*. Physical Review Letters **89**, 011301 (2002).

[Ale94] A. ALESSANDRELLO ET AL. *Bolometric measurement of the beta spectrum of* ^{113}Cd. Nuclear Physics B Proceedings Supplements **35**, 394 (1994).

[Ale96] A. ALESSANDRELLO ET AL. *Evidence for Naturally Occurring Electron Capture of* ^{123}T. Physical Review Letters **77**, 3319 (1996).

[Ale00] A. ALESSANDRELLO ET AL. *New experimental results on double beta decay of* ^{130}Te. Physics Letters B **486**, 13 (2000).

[Ale03] A. ALESSANDRELLO ET AL. *New limits on naturally occurring electron capture of* ^{123}Te. Physical Review C **67**, 014323 (2003).

[Alt98] J. ALTEGOER ET AL. *The NOMAD Experiment at the CERN SPS*. Nuclear Instruments and Methods in Physics Research, Section A **404**, 96 (1998).

[Ama04] K. AMAKO, P. L. ET AL. *GEANT4 and its validation* (2004). Proceedings of the 9th Topical Seminar on Innovative Particle and Radiation Detectors Siena, 23-26 May 2004, to be published in Nuclear Physics B Proceedings Supplements.

[Amm99] M. AMMAN and P. LUKE. *Characterization of a large-volume, multi-element CdZnTe detector*. IEEE Transactions on Nuclear Science **46** (3), 205 (1999).

[Arn03] C. ARNABOLDI ET AL. *A calorimetric search on double beta decay of* ^{130}Te. Physics Letters B **557**, 167 (2003).

[Arn05] C. ARNABOLDI ET AL. *A new limit on the neutrinoless beta beta decay of* ^{130}Te (2005). `hep-ex/0501034`.

[Aud95] G. AUDI and A. WAPSTRA. *The 1995 update to the atomic mass evaluation*. Nuclear Physics A **595**, 409 (1995).

[Bac02] H. O. BACK ET AL. *Search for electron decay mode* $e \rightarrow \gamma + \nu$ *with prototype of Borexino detector*. Physics Letters B **525**, 29 (2002).

[Bal93] A. BALYSH ET AL. *New experimental limits for electron decay and charge conservation.* Physics Letters B **298**, 278 (1993).

[Bar96] A. BARABASH ET AL. *Theoretical and experimental investigation of the double beta processes in* ^{106}Cd. Nuclear Physics A **604**, 115 (1996).

[Bar01] A. BARABASH ET AL. *New limits on the beta beta decay of* ^{130}Te *to excited states of* ^{130}Xe. The European Physical Journal A **11**, 143 (2001).

[Bar04] I. BARABANOV ET AL. *Results of the LENS R&D and prototype measurements at LNGS and MPIK* (2004). Poster at Neutrino 2004.

[Bea61] G. BEARD and W. KELLEY. *Beta Decay of Naturally Radioactive* ^{115}In. Physical Review **122**, 1576 (1961).

[Bel87] E. BELLOTTI ET AL. *A Search for Double Beta Decay of* ^{128}Te *and* ^{130}Te *Leading to the First Excited State of Daughter Nuclei*. Europhysics Letters **3** (8), 889 (1987).

[Bel89] P. BELLI ET AL. *Deep underground Neutron Flux Measurement with Large* BF_3 *Counters*. Il nuovo Cimento A **101**, 959 (1989).

[Bel99] P. BELLI ET AL. *New limits on* $2\beta^+$ *decay processes in* ^{106}Cd. Astroparticle Physics **10**, 115 (1999).

[Bel03] E. BELLOTTI. *The Gallium Neutrino Observatory (SNO)* (2003). TAUP 2003 Conference, Seattle.

[Boc96] J. BOCKHOLT ET AL. (Heidelberg - Moscow-Collaboration). *Bounds on new Majoron models from the Heidelberg - Moscow - Experiment*. Physical Review D **54**, 3641 (1996).

[Boe87] F. BOEHM and P. VOGEL. *Physics of Massive Neutrinos* (Camebridge University Press, 1987).

[Bri00] J. BRIESMEISTER. *MCNP - A General Monte Carlo N-Particle Transport Code, Version 4C*. Los Alamos National Laboratory (2000). LA-13709-M.

[Bru87] R. BRUN, F. BRUYANT, M. MAIRE ET AL. *GEANT3*. (1987). CERN-DD/EE/84-1.

[Bug98] E. BUGAEV ET AL. *Atmospheric Muon Flux at Sea Level, Underground and Underwater*. Physics Review D **58**, 05401 (1998).

[Chu99] S. CHU, L. EKSTRÖM and R. FIRESTONE. *WWW Table of Radioactive Isotopes* (database version 2/28/1999). URL `http://nucleardata.nuclear.lu.se/nucleardata/toi/`.

[Chu03] M. CHU, S. TERTERIAN and D. TING. *Role of Zinc in CdZnTe Radiation Detectors: Why Zinc? How Much?* (2003). Proceedings of the 2003 IEEE Nuclear Science Symposium, Workshop on Room-Temperature Semiconductor Detectors (RTSD), Portland, Oregon, 19-24 Oct 2003.

[Cos73] L. COSTRELL. *NIM Standard.* (Plenum Press, New York, 1973).

[Cow53] C. COWAN, F. REINES, F. HARRISON ET AL. *Large Liquid Scintillation Detectors*. Physical Review **90**, 493 (1953).

[Cuz87] M. CUZIN. *Some new developments in the field of high atomic number materials*. Nuclear Instruments and Methods in Physics Research, Section A **253**, 407 (1987).

[Dan96a] F. DANEVICH ET AL. *Beta Decay of* ^{113}Cd. Physics of Atomic Nuclei **59** (1), 5 (1996).

[Dan96b] F. DANEVICH ET AL. *Investigation of* $\beta^+\beta^+$ *and* β^+*/EC decay of* ^{106}Cd. Zeitschrift für Physik A **355**, 433 (1996).

[Dan00] F. DANEVICH ET AL. *New results of* ^{116}Cd *double beta decay study with* $^{116}CdWO_4$ *scintillators*. Physical Review C **62**, 045501 (2000).

[Dan03] F. DANEVICH ET AL. *Search for* 2β *decay of cadmium and tungsten isotopes: Final results of the Solotvina experiment*. Physical Review C **68**, 035501 (2003).

[Dan04] F. A. DANEVICH ET AL. $ZnWO_4$ *crystals as detectors for* 2β *decay and dark matter experiments* (2004). `nucl-ex/0409014`.

[Dav68] J. DAVIS, RAYMOND, D. S. HARMER and K. C. HOFFMAN. *Search for neutrinos from the sun.* Physical Review Letters **20**, 1205 (1968).

[Doi88] M. DOI, T. KOTANI and E. TAKASUGI. *The neutrinoless double beta decay with majoron emission.* Physical Review D **37**, 2575 (1988).

[Eid04] S. EIDELMAN ET AL. *Review of Particle Physics.* Physics Letters **B 592**, 1 (2004).

[Eji01] H. EJIRI ET AL. *Limits on the Majorana neutrino mass and right-handed weak currents by neutrinoless double beta decay of* ^{100}Mo. Physical Review C **63**, 065501 (2001).

[eV-04] EV-PRODUCTS (2004). http://www.evproducts.com/.

[Fer02] F. FERUGLIO, A. STRUMIA and F. VISSANI. *Neutrino oscillations and signals in* β *and* $0\nu2\beta$ *experiments.* Nuclear Physics A **637**, 345 (2002).

[Fla00] M. FLANZ, W. RODEJOHANN and K. ZUBER. *Trimuon production in νN-scattering as a probe of massive neutrinos*. The European Physical Journal C - Particles and Fields **16** (3), 453 (2000).

[For04] FORMAGGIO, J.A. AND MARTOFF, C.J. *Backgrounds to Sensitive Experiments Underground*. Annual Review of Nuclear and Particle Science **54**, 361 (2004).

[Fuk98] Y. FUKUDA ET AL. *Evidence for Oscillation of Atmospheric Neutrinos*. Physical Review Letters **81**, 1562 (1998).

[Ful05] B. FULTON. *Personal communications* (2005). University of Birmingham, United Kingdom.

[Gav03] V. N. GAVRIN. *Results from the Russian American Gallium Experiment (SAGE)* (2003). TAUP 2003 Conference, Seattle.

[Geo95] A. GEORGADZE ET AL. *Study of ^{116}Cd Double Beta Decay with $^{116}CdWO_4$ Scintillators*. Physics of Atomic Nuclei **58** (7), 1093 (1995).

[Gil95] G. GILMORE and J. HEMINGWAY. *Practical Gamma-Ray Spectrometry* (John Wiley & Sons, Inc., 1995).

[GM35] M. GOEPPERT-MAYER. *Double Beta-Disintegration*. Physical Review **48**, 512 (1935).

[Goz04] M. GOZDZ, W. A. KAMINSKI and A. WODECKI. *Minimal supersymmetric standard model with gauge mediated supersymmetry breaking and neutrinoless double beta decay*. Physical Review C **69**, 025501 (2004).

[Gre70] W. E. GRETH, S. GANGADHARAN and R. L. WOLKE. *Beta instability in cadmium-113*. Journal of Inorganic and Nuclear Chemistry **32**, 2113 (1970).

[Gößß05] C. GÖSSLING, M. JUNKER, H. KIEL ET AL. *Experimental study of ^{113}Cd beta decay using CdZnTe detectors* (2005).

[Ham99] W. HAMPEL ET AL. *GALLEX Solar Neutrino Observations: Results for GALLEX IV*. Physics Letters B **447**, 127 (1999).

[He98] Z. HE, G. KNOLL, D. WEHE ET AL. *Coplanar grid patterns and their effect on energy resolution of CdZnTe detectors*. Nuclear Instruments and Methods in Physics Research, Section A **411**, 107 (1998).

[He03] Z. HE and B. STURM. *Characteristics of Depth Sensing Coplanar-Grid CdZnTe Detectors* (2003). Proceedings of the 2003 IEEE Nuclear Science Symposium, Workshop on Room-Temperature Semiconductor Detectors (RTSD), Portland, Oregon, 19-24 Oct 2003.

[Hir94] M. HIRSCH, K. MUTO, T. ODA ET AL. *Nuclear structure calculations of $\beta^+\beta^+$, β^+/EC and EC/EC decay matrix elements*. Zeitschrift für Physik A **347**, 151 (1994).

[Jon75] L. JONES and P. WOODLAM. *Resolution Improvement in CdTe Gamma Detectors Using Pulse-Shape Discrimination*. Nuclear Instruments and Methods in Physics Research **124**, 591 (1975).

[Kaw97] M. KAWAGUTI and S. TANAKA. *DAWN for GEANT4 visualization* (1997). Talk given at Computing in High-energy Physics (CHEP 97), Berlin, Germany, 7-11 Apr 1997.

[Kie01] H. KIEL. *Analyse von Trimyon-Ereignissen im Frontkalorimeter des NOMAD-Detektors*. Diploma thesis, University of Dortmund, Germany (2001).

[Kie03] H. KIEL, D. MUENSTERMANN and K. ZUBER. *A Search for various Double Beta Decay Modes of Cd, Te and Zn Isotopes*. Nuclear Physics A **723**, 499 (2003).

[Kie04] H. KIEL. *POISON Version 0.9.3, COBRA GEANT4 Monte Carlo - User Manual* (2004). COBRA manual.

[Kie05] H. KIEL ET AL. *New and improved limits on various double beta decay rates of Cd, Zn and Te isotopes* (2005).

[KK01a] H. V. KLAPDOR-KLEINGROTHAUS, A. DIETZ, H. L. HARNEY ET AL. *Evidence for neutrinoless double beta decay*. Modern Physics Letters A **16**, 2409 (2001).

[KK01b] H. V. KLAPDOR-KLEINGROTHAUS ET AL. *Latest results from the Heidelberg-Moscow double-beta-decay experiment*. The European Physical Journal A **12**, 147 (2001).

[Kla99] J. KLAIBER-LODEWIGS. *Eigenschaften und Einsatz von CdTe/CdZnTe-Mikrostreifendetektoren*. Diploma thesis, University of Bonn, Germany (1999).

[Kno79] G. F. KNOLL. *Radiation Detection and Measurement.* (John Wiley & Sons, Inc., 1979).

[Kon66] E. J. KONOPINSKI. *The Theory of Beta Radioactivity.* (Oxford University Press, 1966).

[Kra04] O. KRASEL. *Charge Collection in Irradiated Silicon-Detectors*. PhD thesis, University of Dortmund, Germany (2004).

[Lau04] M. LAUBENSTEIN. *Personal communications*. LNGS (2004).

[LeC80] LECROY RESEARCH SYTEMS CORPORATION. *CAMAC Model 3512, High Performance Buffered Spectroscopy ADC* (1980). Technical Manual.

[Leo92] W. LEO. *Techniques for Nuclear and Particle Physics Experiments.* (Springer Verlag, 1992).

[Lob85] V. M. LOBASHEV ET AL. *A method for measuring the electron antineutrino rest mass*. Nuclear Instruments and Methods in Physics Research, Section A **240**, 305 (1985).

[Luk95] P. LUKE. *Unipolar Charge Sensing with Coplanar Electrodes – Application to Semiconductor Detectors*. IEEE Transactions on Nuclear Science **42**, 207 (1995).

[Mak62] Z. MAKI and S. NAKAGAWA, M. SAKATA. *Remarks on the unified model of elementary particles*. Progress of Theoretical Physics **28**, 870 (1962).

[McC93] J. MCCABE, A. SMITH and J. MEADOWS. *Evaluated Nuclear Data Files for the Naturally Occurring Isotopes of Cadmium*. Argonne National Laboratory (ANL/NDM-129) (1993).

[McK05] D. MCKECHAN. *A Monte Carlo simulation of the COBRA detector and its comparison with data*. Project thesis, University of Sussex, Brighton, United Kingdom (2005).

[Mit88] L. MITCHELL and P. FISCHER. *Rare decays of cadmium and tellurium*. Physical Review C **38**, 895 (1988).

[MK94] T. MAYER-KUCKUCK. *Kernphysik*. (Teubner Studienbücher, 1994).

[Mue01] D. MUENSTERMANN. *Untersuchung seltener Kernzerfälle mit Cadmium-Tellurid-Detektoren*. Diploma thesis, University of Dortmund, Germany (2001).

[Mue03] D. MUENSTERMANN and K. ZUBER. *An alternative search for the electron capture of* ^{123}Te. Journal of Physics G **29**, B1 (2003).

[Mue05] D. MUENSTERMANN. PhD thesis, University of Dortmund, Germany (2005). In preparation.

[Nor85] E. NORMAN. *Improved limits on the double beta decay half-lives of* ^{50}Cr, ^{64}Zn, ^{92}Mo *and* ^{96}Ru. Physical Review C **31**, 1937 (1985).

[Nor87] E. NORMAN and D. MEEKHOF. *New limits on the double beta decay half-lives of* ^{94}Zr, ^{96}Zr, ^{116}Cd *and* ^{124}Sn. Physics Letters B **195** (2), 126 (1987).

[Nor96] E. B. NORMAN, J. N. BAHCALL and M. GOLDHABER. *"Improved limit on charge conservation derived from* ^{71}Ga *solar neutrino experiments"*. Physical Review D **53**, 4086 (1996).

[Oeh04] S. OEHL. *A Shielding System Against Neutrons for the COBRA-Experiment and Characterisation of CdZnTe Detectors with the Transient Current Technique*. Diploma thesis, University of Dortmund, Germany (2004).

[Pan05] L. PANDOLA. *Personal communications* (2005). Laboratori Nazionali del Gran Sasso,, INFN, Italy.

[Pau30] W. PAULI. *Brief an die Radioaktiven* (1930).

[Pet93] W. D. PETERSON. *The VMEbus Handbook, expanded third edition* (VFEA International Trade Association, 1993).

[Pfe79] L. PFEIFFER ET AL. *Beta spectrum of* ^{115}In. Physical Review C **19**, 1035 (1979).

[Pic92] A. PICARD ET AL. *A solenoid retarding spectrometer with high resolution and transmission for keV electrons*. Nuclear Instruments and Methods in Physics Research, Section B **63**, 345 (1992).

[Pie94] A. PIEPKE ET AL. *Investigation of the $\beta\beta$ Decay of ^{116}Cd into excited States of ^{116}Sn*. Nuclear Physics A **577**, 510 (1994).

[Pon00] O. PONKRATENKO, V. TRETYAK and Y. ZDESENKO. *Event Generator DECAY4 for Simulating Double-Beta Processes and Decays of Radioactive Nuclei*. Physics of Atomic Nuclei **63**, 1282 (2000).

[Por96] E. PORRAS ET AL. *Production of radionuclides by 1.7-GeV proton-induced reactions on CdTe crystals*. Nuclear Instruments and Methods in Physics Research, Section B **111**, 315 (1996).

[Pov95] B. POVH, K. RITH, C. SCHOLZ ET AL. *Teilchen und Kerne*. (Springer Verlag, 1995).

[Pra03] T. PRADHAN. *Electron decay* (2003). `hep-th/0312325`.

[Ram39] S. RAMO. *Currents induced by electron motion*. Proceedings of the Institute of Radio Engineers **27**, 584 (1939).

[Rei53a] F. REINES and C. L. COWAN. *Detection of the Free Neutrino*. Physical Review **92**, 830 (1953).

[Rei53b] F. REINES and C. L. COWAN. *A Proposed Experiment Detect the Free Neutrino*. Physical Review **90**, 492 (1953).

[Rei59] F. REINES and C. L. COWAN. *Free Antineutrino Absorption Cross Section. I. Measurement of the Free Antineutrino Absorption Cross Section by Protons*. Physical Review **113**, 273 (1959).

[Rod01] W. RODEJOHANN and K. ZUBER. *Neutrinoless double beta decay at a neutrino factory*. Physical Review D **63**, 054031 (2001).

[Roy83] A. ROY ET AL. *Further experimental test of nucleon charge conservation through the reaction $^{113}Cd \rightarrow {}^{113m}In$ + neutrals*. Physical Review D **28**, 1770 (1983).

[Sch82] J. SCHECHTER and J. W. F. VALLE. *Neutrino decay and spontaneous violation of lepton number*. Physical Review D **25**, 774 (1982).

[SE98] W. SEELMANN-EGGEBERT, G. PFENNIG and H. KLEWE-NEBENIUS. *Karlsruher Nuklidkarte / Chart of the Nuclides* (Forschungszentrum Karlsruhe GmbH, 1998). 6. Auflage 1995, korrigierter Nachdruck 1998.

[Shi78] V. SHIRLEY and C. LEDERER. *Table of Isotopes* (Wiley-Interscience, 1978).

[Shi02] K. SHIBATA, K. T. ET AL. *Japanese Evaluated Nuclear Data Library, Version 3, Revision 3*. Journal of Nuclear Science and Technology **39** (11), 1125 (2002).

[Shu02] J. SHULTIS and R. FAW. *Fundamentals of Nuclear Science and Engineering* (Marcel Dekker, 2002).

[Sin98] B. SINGH ET AL. *Review of Logft Values In β Decay*. Nuclear Data Sheets **84**, 487 (1998).

[Sta90] A. STAUDT, K. MUTO and H. V. KLAPDOR-KLEINGROTHAUS. *Calculation of 2nu and 0nu double-beta decay rates*. Europhysics Letters **13**, 31 (1990).

[Suj03] Z. SUJKOWSKI. *Neutrino-less double beta decay: Experimentum crucis of neutrino physics*. Acta Physica Polonica **B34**, 2207 (2003).

[Sze98] C. SZELES and M. DRIVER. *Growth and properties of semi-insulating CdZnTe for radiation detector applications*. Proceedings of SPIE **3446**, 2 (1998).

[Ton96] J. TONEY ET AL. *Uniformity of $Cd_{1-x}Zn_xTe$ grown by high-pressure Bridgman*. Nuclear Instruments and Methods in Physics Research, Section A **380**, 132 (1996).

[Tre95] V. TRETYAK and Y. ZDESENKO. *Tables of double beta decay*. Atomic Data and Nuclear Data Tables **61**, 43 (1995).

[Tre02] V. TRETYAK and Y. ZDESENKO. *Tables of double beta decay - an update*. Atomic Data and Nuclear Data Tables **80**, 83 (2002).

[Wah96] W. WAHL. *$\alpha \cdot \beta \cdot \gamma$ Table of Commonly used Radionuclides*. (Institution für Spektrometrie und Strahlenschutz, 1996).

[Wat62] D. WATT and R. GLOVER. *A Search for Radioactivity among the Naturally Occurring Isobaric Pairs*. Philosophical Magazine **7**, 105 (1962).

[Wei35] C. WEIZSÄCKER. *Zur Theorie der Kernmassen*. Zeitschrift für Physik **96**, 431 (1935).

[Wei99] C. WEINHEIMER ET AL. *High precision measurement of the tritium beta spectrum near its endpoint and upper limit on the neutrino mass*. Physics Letters B **460**, 219 (1999).

[Wei03] C. WEINHEIMER ET AL. *Direct neutrino mass experiments: Present and future*. Nuclear Physics B Proceedings Supplements **118**, 279 (2003).

[Wil05] J. WILSON. *A Preliminary Simulation of Backgrounds due to Paint on the Crystals* (2005). COBRA internal Memo.

[Zde02] Y. G. ZDESENKO, F. A. DANEVICH and V. I. TRETYAK. *Has neutrinoless double beta decay of Ge-76 been really observed?*. Physics Letters B **546**, 206 (2002).

[Zub98] K. ZUBER. *On the Physics of Massive Neutrinos*. Physics Reports **305** (6) (1998).

[Zub01] K. ZUBER. *COBRA: Double beta decay searches using CdTe detectors*. Physics Letters B **519**, 1 (2001).

[Zub03] K. ZUBER. *Spectroscopy of low energy solar neutrinos using CdTe detectors*. Physics Letters B **571**, 148 (2003).

[Zub04] K. ZUBER. *Neutrino Physics* (Institute of Physics Publishing, 2004).

Publications

Articles

H. Kiel, D. Muenstermann and K. Zuber
A Search for various Double Beta Decay Modes of Cd, Te and Zn Isotopes
Nuclear Physics A 723, 499 (2003)

Articles in preparation

C. Gößling, M. Junker, H. Kiel, D. Muenstermann, S. Oehl and K. Zuber
Experimental study of ^{113}Cd beta decay using CdZnTe detectors

H. Kiel and others
New and improved limits on various double beta decay rates of Cd, Zn and Te isotopes

Conference Talks

H. Kiel, K. Zuber, Y. Ramachers and D. Muenstermann
COBRA - Search for Double Beta Decays using CdTe Detectors
Nuclear Physics Spring Meeting
March 11 – 15 2002, Münster (Germany)

Conference Posters

K. Zuber, C. Goessling, H. Kiel, D. Muenstermann and Y. Ramachers
COBRA - A New Approach to Double Beta Decay Using CdTe
Neutrino 2002
May 25 – 30 2002, Munich (Germany)

C. Goessling, **H. Kiel**, D. Muenstermann, S. Oehl, Y. Ramachers and K. Zuber
COBRA - A New Approach to Double Beta Decay Using CdTe
2nd Latin American School of High Energy Physics
June 1 – 14 2003, San Miguel Regla, Hidalgo (Mexico)

Acknowledgements / Danksagung

Last, but not least, I would like to thank all people who have contributed to the completion of this thesis. In this first part I'm going to mention all non-german native speakers. Thanks go to Jeanne Wilson for proof-reading and Oleg Chkvorets for reference simulations and a nice time at LNGS. I would also like to thank the COBRA collaboration for the fruitful cooperation.

An dieser Stelle möchte ich mich bei allen bedanken, die mir während meiner Studiums- und Promotionszeit zur Seite standen und zum Gelingen dieser Arbeit beigetragen haben.
Zum einen wären dort natürlich mein Doktorvater Dr. Kai Zuber, der es mir ermöglicht hat, mich in einem interessanten neuen Experiment entscheidend einzubringen und es zu prägen. Desweiteren gilt mein Dank auch meinem Zweitgutachter Prof. Dr. C. Gößling, der für mich ein guter Gastgeber an seinem Lehrstuhl war und ist.
Ich möchte mich auch bei den Mitgliedern der COBRA Kollaboration und dem Lehrstuhl für Experimentelle Physik 4 für die nette und erfolgreiche Zusammenarbeit bedanken. Speziell geht mein Dank an Sandra Oehl, Jeanne Wilson und Daniel Münstermann für das Korrekturlesen. Desweiteren geht auch ein Dank an Norbert Koch von der Elektronik-Entwicklung des Fachbereichs. Ohne ihn wäre die Entwicklung des VME ADCs nicht möglich gewesen. Danke auch an Oleg Chkvorets für die gesellige Zeit im LNGS und für einige Vergleichssimulationen.
An dieser Stelle sei auch dem Dortmunder Universitätsorchester gedankt, in dem ich mich immer wohl gefühlt habe und mich bei angenehmer Musik ein wenig von der Physik erholen konnte.
In die Reihe der Korrekturleser gesellen sich auch Herr Dipl.-Ing. (FH) Holger Klönne, sowie Dr. Matthias Althaus, mit dem ich eine angenehme Studien- und Diplomarbeitszeit in Dortmund verbracht habe.
Ich möchte auch ganz herzlich meinen Eltern Elsbeth und Hans-Joachim Kiel und meinem Bruder Holger für ihre Unterstützung danken. Ein ganz spezieller Dank geht an meine Freundin Stefanie Schleich für ihre Liebe und Geduld.